Zachos, J.C., Kroon, D., Blum, P., et al., 2004
Proceedings of the Ocean Drilling Program, Initial Reports Volume 208

6. SITE 1265[1]

Shipboard Scientific Party[2]

INTRODUCTION

Site 1265 (proposed Site WALV-9B; seismic line GeoB 01-048, common depth point [CDP] 3854) is located in a broad channel at the base of a slope extending westward down from the crest of Walvis Ridge (Figs. **F1,** p. 52, and **F2,** p. 53, both in the "Leg 208 Summary" chapter; Fig. **F1**). The site is at an upper bathyal water depth of 3083 m, ~48 m deeper than Deep Sea Drilling Project (DSDP) Site 529 located 15 km to the southeast where a 417-m-thick sequence of Maastrichtian to Pleistocene sediment was recovered (Moore, Rabinowitz, et al., 1984). The Site 529 sequence was poorly recovered, particularly the Paleocene interval, because of rotary drilling. Slumps were encountered at this site in the upper Paleocene, in the Oligocene–Miocene, and in the lower Pleistocene intervals. The upper lower Oligocene through Pleistocene interval (0–160 meters below seafloor [mbsf]) of the Site 529 sedimentary record consists of homogeneous foraminifer-nannofossil and nannofossil ooze. The upper Paleocene to upper lower Oligocene unit (160–284 mbsf) consists of nannofossil and foraminifer-nannofossil oozes and chalks. This unit lies on top of the lowermost interval, which extends to the bottom of the hole at 417 mbsf. The oldest sediments are Maastrichtian in age.

F1. Seismic line GeoB 01-048, p. 34.

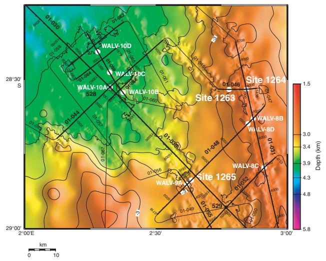

Our main objective for this site was the recovery of undisturbed sediments recording critical intervals in the early Cenozoic, specifically the Paleocene/Eocene Thermal Maximum and the period of global cooling and growth of polar ice caps across the Eocene/Oligocene (E/O) boundary into the earliest Oligocene (early Oligocene Glacial Maximum). We planned to recover 100% of the sedimentary section in multiple holes to make it possible to establish a cyclostratigraphy and develop an astronomically tuned timescale. We aimed to fully document events across the critical intervals as well as short climate fluctuations during the early Eocene Climatic Optimum. Site 1265 is located in water ~350

---

[1] **Examples of how to reference the whole or part of this volume.**
[2] **Shipboard Scientific Party addresses.**

Ms 208IR-106

m deeper than that at Site 1263, the shallow anchor of the Leg 208 depth transect, and thus will provide constraints on intermediate water chemistry.

Site 1265 is located in an area where a continuous and expanded sequence of upper Paleocene and Eocene calcareous nannofossil ooze could be cored using the advanced piston corer (APC), and we aimed to avoid slumps. It is situated near a small bathymetric high that is underlain by thick sequences of Neogene and Paleogene sediment (Fig. F2). The sequences are separated by a prominent reflector, $R_{O/M}$, which is just below the Oligocene/Miocene (O/M) boundary (Fig. F3). Two distinct reflectors in the lower sequence, $R_{P/E}$ and $R_{K/P}$, represent the Paleocene/Eocene (P/E) and Cretaceous/Paleogene (K/P) boundaries, respectively. The upper sequence thins considerably in a northeast direction from the high toward the channel, although the thickness of the lower sequence as judged by the distance between $R_{P/E}$ and $R_{K/P}$ remains about the same. As a result, the depth of the P/E boundary, estimated to be at 270 mbsf (velocity = 1.8 m/ms; 300 ms two-way traveltime [TWT] below seafloor) was just within the effective working range of the APC.

F2. Site 1265 and proposed Site WALV-9A, p. 35.

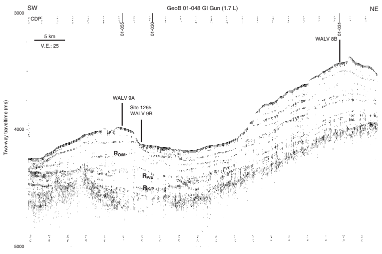

F3. Line GeoB 01-046 and Site 1265 with ages, p. 36.

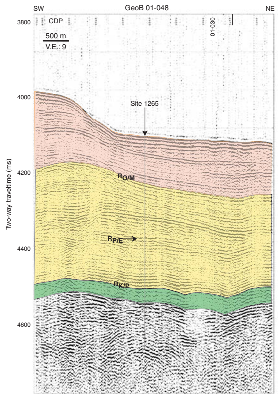

Coring in four holes at Site 1265 yielded a 313-m-thick sequence of upper Paleocene through Holocene calcareous sediments with condensed clay-rich intervals in the middle to upper Eocene and upper Miocene (see the **"Leg 208 Summary"** chapter). The APC system was used to the depth of the P/E boundary (~274 mbsf) in at least two holes (1265A and 1265D). The extended core barrel (XCB) system was deployed when the APC system reached refusal depth, which varied from hole to hole. The upper Paleocene to lower Eocene and upper Eocene to lower Oligocene are expanded and stratigraphically complete. Despite significant reworking, lithologic cycles in the cores spanning the E/O boundary can be correlated with cycles in other cores of the depth transect. The P/E boundary clay layer was recovered fully intact in one hole.

OPERATIONS

Transit to Site 1265

The 21-nmi transit to Site 1265 (proposed Site WALV-9B) was accomplished in 2.3 hr at an average speed of 9.1 kt. The vessel was positioned over the site at 1415 hr on 8 April 2003. The corrected precision depth recorder seafloor depth estimate was 3079.4 meters below rig floor (mbrf). The polycrystalline diamond compact drill bit used at the previous sites was retired from service because it had sustained considerable damage to the cutting structure due to drilling through numerous chert layers. The bit was replaced with a new Rock Bit International C-3 11$^{7}/_{16}$-in rotary bit.

Coring intervals, times, nominal recovery rates, core barrels that required drillover to be released from the sediment, and the deployments of the Advanced Piston Corer Temperature (APCT) tool, Tensor core orientation tool, and nonmagnetic core barrel are listed in Table T1.

T1. Coring summary, p. 87.

Hole 1265A

Hole 1265A was initiated at 0000 hr on 9 April with the bit at 3071.0 mbrf. The seafloor depth estimated by the recovery of a full core barrel was provisionally established at 3071.0 mbrf. APC coring advanced to 285.6 mbsf, where the formation became too indurated, as APC strokes were incomplete on three consecutive cores (208-1265A-30H, 31H, and 32H), and the bit was advanced by recovery. The hole was deepened with the XCB system to the target depth of 321.0 mbsf. The active heave compensator was used while coring three of the four XCB cores (208-1265A-34X through 36X).

After flushing the hole with a 40-bbl sepiolite mud sweep, the hole was displaced with 142 bbl of 8.6-lb/gal sepiolite mud. The drill string was pulled back, and the bit was positioned at 83.8 mbsf. The triple combination (triple combo) tool string was lowered to 321.0 mbsf (bottom of hole), and the hole was logged up to the seafloor. In a separate run, the Lamont-Doherty Earth Observatory (LDEO) Multi-Sensor Gamma Ray Tool (MGT) logged the hole in acquisition mode from total depth to the drill pipe. The second tool string (Formation MicroScanner [FMS]-sonic) also reached the bottom of the hole. The third logging effort was a single-axis checkshot vertical seismic profile using the Well Seismic Tool (WST-3) with seven measurement stations. The tool could not be anchored at the top station at 139 mbsf because of the large diameter of the hole. The bit was pulled clear of the seafloor at 1045 hr on 11 April, and the vessel was offset 20 m west.

Hole 1265B

After obtaining a bottom water temperature with the APCT at 3066 mbrf, Hole 1265B was initiated at 1255 hr with the bit placed 5 m shallower than it was placed in Hole 1265A in order to obtain a stratigraphic overlap. The calculated seafloor depth from the recovery of the first core was 3070.8 mbrf. Piston coring advanced to 251.7 mbsf, where the core barrel jammed inside the bottom-hole assembly (BHA). After the core winch operator tried for nearly 3 hr to recover the core barrel and to part the shear pin in the overshot at the bottom of the sinker bar assembly, the coring line was cut above the sinker bars using the Kinley wireline cutter and the drill string and BHA were recovered. Once the BHA was on the surface, the coring line was found tangled around and jammed into the sinker bar swivel. This configuration also impeded the core winch operator’s ability to jar down and part the overshot shear pin to release the coring line from the core barrel. The problem was apparently caused by slack in the coring line during or shortly after the firing of the piston corer, which snarled in the sinker bar swivel and made recovery of the core barrel impossible. The coring line was freed and reterminated, and the full core barrel was subsequently recovered. The Kinley cutter and hammers were recovered, and all BHA components were inspected. No visible hardware damage was observed.

Hole 1265C

Hole 1265C was initiated at 1130 hr on 13 April and was drilled ahead without coring with a center bit to 185.0 mbsf. The center bit was retrieved, and the first piston core was obtained from 185.0 to 194.5 mbsf. The aft coring line was utilized, running the barrel in, but the forward coring line was used to recover Core 208-1265C-1H because the aft coring line was kinked as the possible result of recoil when the corer was fired. The second piston core was obtained from 194.5 to 204.0 mbsf and also achieved a full stroke of the corer. When 70,000 lb of force could not release the core barrel, it was drilled over. When the core winch operator attempted to recover the core barrel, it appeared to move a few meters and then became firmly stuck. After working the winch for 2 hr in a vain attempt to recover the core barrel and part the shear pin, the Kinley wireline cutter was deployed again to sever the coring line just above the sinker bars at a depth of ~3260 mbrf. After the drill string was recovered once more, the coring line was found tangled around and jammed into the sinker bar swivel in the same fashion as during the previous incident on 12 April. The coring line was freed and reterminated, and the full core barrel was recovered. The Kinley cutter and hammer were recovered, and the landing seat was inspected and replaced because of a small crack in the shoulder area that was not related to this incident. The lockable float valve and bit were inspected and kept in service. It was speculated that a combination of heave (~3 m) and lithology-induced recoil (possibly augmented by chert stringers) was responsible for this incident.

Hole 1265D

Hole 1265D was initiated at 1540 hr on 14 April for a final attempt at obtaining another sample of the P/E boundary. After drilling ahead with a center bit to 248.0 mbsf, XCB coring advanced the hole from 248.0 to 270.0 mbsf. The APC was then used to obtain a partial sample of the P/E boundary from 270.0 to 274.9 mbsf.

The total cored interval for the site was 619 m, and the recovered interval was 587 m (average nominal recovery = 95%). The total interval drilled without coring was 433 m.

Four downhole temperature measurements (Hole 1265A; 38–124 mbsf) and one bottom water temperature measurement (Hole 1265B) with the APCT yielded an initial temperature gradient estimate of 4.5°C/100 m.

The drill string was recovered, the hydrophones and thrusters were secured, the beacon was recalled and recovered, and the vessel left for the next site at 1130 hr on 15 April.

COMPOSITE DEPTH

Magnetic susceptibility (MS) and sediment lightness (L*) data (600 nm/450 nm ratio) collected from Holes 1265A, 1265B, 1265C, and 1265D at 2.5-cm intervals were used to correlate cores and to construct the composite section for Site 1265. Multisensor track (MST) data were collected at 5-cm intervals from 0 to 105 mbsf in Holes 1265A and 1265B. In the carbonate-rich sediments from ~10 to 30 mcd, only the 600 nm/450 nm ratio (orange/blue ratio) provided a signal-to-noise ratio suitable for correlation between holes (Figs. F4, F5). The depth offsets that define the composite section for Site 1265 are given in Table T2.

The composite depths of Cores 208-1265A-30H through 36X were calculated using a 14% meters composite depth (mcd) growth rate obtained from Holes 1265A and 1265B (Fig. F6). This growth rate is based on the correlation of Cores 208-1265A-1H through 27H and 208-1265B-1H through 27H in the depth interval of 0–295 mcd. The composite data show that the cores from Site 1265 provide an almost continuous stratigraphic sequence from the seafloor to 316 mcd, the upper Paleocene (Core 208-1265A-29H). Following construction of the composite depth section for Site 1265, a single spliced record was assembled from the aligned core records from the four parallel holes (Table T3). The lack of overlap between the base of Core 208-1265A-27H and the top of

F4. MS data, p. 37.

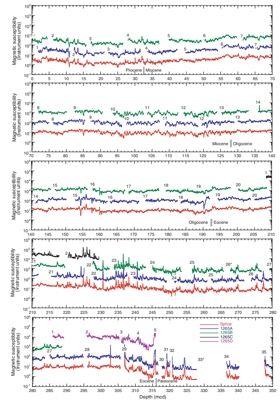

F5. Color reflectance data, p. 38.

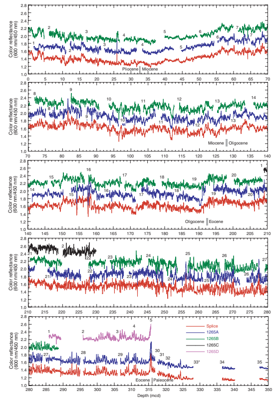

T2. Composite depth scale, p. 89.

F6. Mcd growth rates, p. 39.

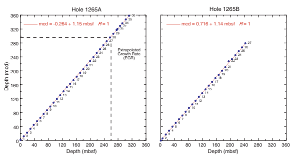

T3. Splice tie points, p. 90.

Core 208-1265B-28H and between Cores 208-1265D-2X and 208-1265A-29H resulted in two gaps in the spliced record. Most of the cores were not significantly stretched, squeezed, or disturbed by the coring process. As a result, the color and MS cycles were reasonably well aligned between holes (e.g., Figs. **F4, F5**), although the mcd values of the same stratigraphic horizon in alternate holes may not be exactly the same.

The P/E boundary interval in the composite was taken from Core 208-1265A-29H. The Site 1265 splice (Table **T3**) can be used as a guide to sample a single sedimentary sequence between the seafloor and 316 mcd and was used to plot other data sets from this site.

LITHOSTRATIGRAPHY

Four holes were drilled at Site 1265. Holes 1265A and 1265B were continuously cored to 359.5 mcd (312.4 mbsf) and 288.8 mcd (251.9 mbsf), respectively. Hole 1265C was washed to 208.4 mcd (185.0 mbsf) and cored to 229.9 mcd (204.3 mbsf). Holes 1265B and 1265C were terminated prematurely because of mechanical problems (see **"Operations,"** p. 2). Hole 1265D was washed to 285.9 mcd (248.0 mbsf) and cored to 315.9 mcd (274.9 mbsf) to obtain a second copy of the P/E boundary. Major lithologies include nannofossil ooze, foraminifer-bearing nannofossil ooze, foraminifer-nannofossil ooze, nannofossil-foraminifer ooze, clay-bearing nannofossil ooze, and foraminifer- and clay-bearing nannofossil ooze. Minor and accessory lithologies include ash-bearing nannofossil ooze, ashy nannofossil ooze, clay-bearing volcanic glass, zeolite- and nannofossil-bearing clay, clay, calcareous dinoflagellate cyst–bearing nannofossil ooze, and hematite-bearing nannofossil ooze. Evidence for moderate to extensive bioturbation is prevalent within sediment intervals of higher color contrast but is largely absent within sediment intervals of lower color contrast. Drilling disturbance was minimal in most cores; some intervals were affected by APC soft-sediment deformation or XCB biscuiting.

By combining measurements of MS, sediment L*, and smear slide–based estimates of foraminifer abundance, we have divided this sequence into two lithostratigraphic units, with the lower unit subdivided into three subunits (Table **T4;** Fig. **F7**). Stratigraphic variation for whole-core MST parameters is presented in Figure **F8.** Stratigraphic variation in sediment L*, chromaticity (a* and b*), and carbonate content is presented in Figure **F9.** Stratigraphic smear slide variation in major and minor lithologies is presented in Figure **F10** and highlights the predominance of nannofossils throughout Site 1265 with relatively higher foraminifer abundances within Unit I. As also reflected in the carbonate content, Site 1265 clay abundance is commensurately low throughout and is too subtle for use in defining lithostratigraphic units.

Half-core physical property data show linear downcore trends punctuated by three horizons of change (Fig. **F11**). The first horizon (~52 mcd) is marked by a downcore decrease in compressional wave (*P*-wave) velocity values measured with the *P*-wave velocity sensor 3 (PWS3), a broad relative maximum in grain density, and less variation within bulk density and porosity. The second horizon (~185 mcd) is marked by a step decrease in grain density and porosity. The third horizon (~239 mcd) is marked by a step increase in grain density and *P*-wave velocity. The strong correlation and general downcore increase in both gamma ray attenuation (GRA)-based and moisture and density (MAD)-based es-

T4. Lithostratigraphic subdivisions, p. 91.

F7. Parameters used to define lithostratigraphic units, p. 40.

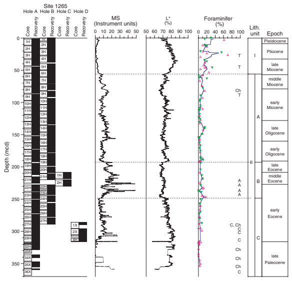

F8. MS, NGR, and GRA bulk density, p. 41.

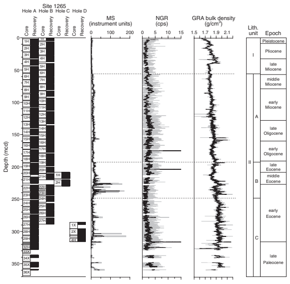

F9. Lightness, carbonate content, and chromaticity, p. 42.

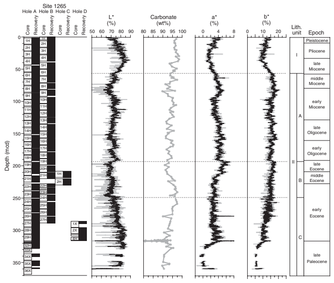

F10. Smear slide components, p. 43.

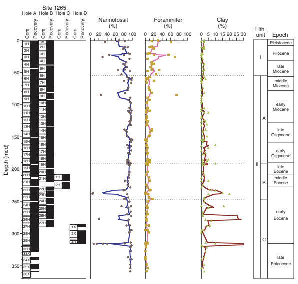

timates of bulk density coupled with the strong negative correlation between bulk density and porosity (Fig. F12) suggest increasing downhole sediment compaction. This interpretation is also supported by the weak correlation between bulk density and PWS3 (Fig. F12) measurements.

Description of Lithostratigraphic Units

Unit I

Interval: 208-1265A-1H-1, 0 cm, through 6H-1, 50 cm; 208-1265B-1H-1, 0 cm, through 6H-4, 108 cm
Depth: Hole 1265A: 0.0–48.0 mbsf (1.6–55.9 mcd); Hole 1265B: 0.0–48.3 mbsf (0.0–55.9 mcd)
Age: Pleistocene to late Miocene
Lithology: foraminifer-bearing nannofossil ooze and nannofossil ooze

Unit I consists primarily of light gray to very pale brown foraminifer-bearing nannofossil ooze with smear slide–based foraminifer percentages averaging 22% (Fig. F7). Nannofossil oozes are less common, and the base of the unit is a clay-bearing nannofossil ooze. MS is consistently low except for a marked increase at the base of Unit I, whereas L* values show a broad and unit-centered relative maximum at ~35 mcd (Fig. F7). Carbonate content averages 96 ± 1 wt% (Fig. F9).

Irregularly shaped, centimeter-scale, pinkish to whitish blebs with gray halos of disseminated fine Mn oxides (Fig. F13) are common in the upper 30 m of Unit I but are absent in the lower part. These blebs show minimal vertical compression with relatively few noncircular cross sections and a large range in diameter (<2 cm to >17 mm). Two ~1-cm-diameter blebs carved from the working half did not extend through the core half. Smear slide comparisons show that the composition of the blebs differ from those of the surrounding sediments only in their Mn oxide content. In intervals without blebs, faint centimeter-scale dark bands are common and rarely bioturbated. Based on these limited observations, blebs may represent localized diagenetic effects related to oxidation-reduction reactions, although a burrow trace origin cannot be ruled out. Discrete centimeter- to decimeter-scale intervals of fining-upward nannofossil foraminifer oozes and nannofossil-bearing foraminifer oozes are present at ~27.4 mcd (interval 208-1265A-3H-4, 62–66 cm; 24.13–24.16 mbsf) and ~41.5 mcd (interval 208-1265A-4H-6, 70–72 cm; 36.55–36.57 mbsf) and are interpreted as turbidites or gravity flows (Fig. F14).

In the middle to upper parts of Unit I, decimeter-scale oscillations in sediment color, marked by an alternation between light gray brown and pale brown lithologies, are well expressed in both L* and MS values (Fig. F15). These color alternations may reflect oscillations in carbonate production and preservation during the glacial–interglacial cycles of the Pliocene–Pleistocene.

Unit II

Interval: 208-1265A-6H-1, 50 cm, through 36X-CC; 208-1265B-6H-4, 108 cm, through 27H-CC, 10 cm; 208-1265C-1H-1, 0 cm, through 2H-CC, 32 cm; 208-1265D-1X-1, 0 cm, through 5X-CC, 10 cm

F11. Grain density, bulk density, porosity, and *P*-wave velocity, p. 44.

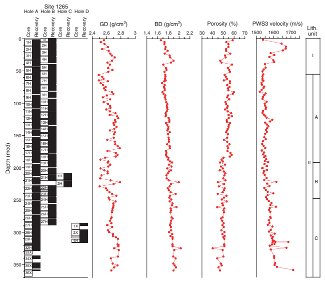

F12. Physical property measurements, p. 45.

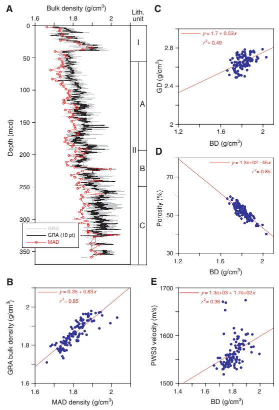

F13. XRD diffractogram of an opaque mineral and matrix, p. 46.

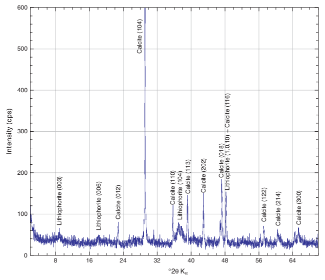

F14. Nannofossil-bearing foraminifer ooze with sharp contacts with nannofossil ooze, p. 47.

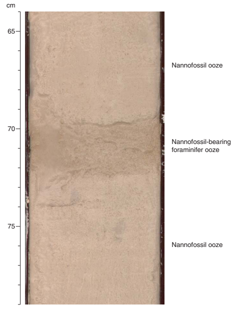

Depth: Hole 1265A: 48.0–312.4 mbsf (55.9–359.5 mcd); Hole 1265B: 48.3–251.9 mbsf (55.9–288.8 mcd); Hole 1265C: 185.0–204.3 mbsf (208.4–229.9 mcd); Hole 1265D: 248.0–274.9 mbsf (285.9–315.9 mcd)
Age: late Miocene to late Paleocene
Lithology: nannofossil ooze and foraminifer-bearing nannofossil ooze

Unit II consists predominantly of light gray to very pale brown nannofossil ooze with rare intervals of darker brown foraminifer-bearing nannofossil ooze. Three subunits (IIA, IIB, and IIC) are defined by markedly higher MS and slightly lower L* within Unit IIB (Fig. F7). Carbonate content averages 94 ± 3 wt% within Unit II, excluding the occasional clay-rich horizons present within the Paleocene and Eocene part of the sequence.

Subunit IIA

Interval: 208-1265A-6H-1, 50 cm, through 18H-7, 0 cm; 208-1265B-6H-4, 108 cm, through 19H-3, 105 cm
Depth: Hole 1265A: 48.0–169.0 mbsf (55.9–191.0 mcd); Hole 1265B: 48.3–170.3 mbsf (55.9–192.7 mcd)
Age: late Miocene to late Eocene
Lithology: nannofossil ooze and foraminifer-bearing nannofossil ooze

Subunit IIA consists predominantly of very pale brown to light gray nannofossil ooze. Rare intervals of slightly darker foraminifer-bearing nannofossil ooze are present between ~90 and ~120 mcd, and the basal portion of the unit is a clay-bearing nannofossil ooze. Carbonate content averages 94 ± 2 wt%. The contact between Unit I and Subunit IIA is marked by a downcore shift in predominance from foraminifer-bearing nannofossil ooze to nannofossil ooze, a step increase in the value and variability of MS, and a marked decrease in L* (Fig. F7). Cyclicity in both L* and MS values is present throughout Subunit IIA, with these values generally showing an inverse relationship (Fig. F16A).

Blebs are rare to absent. Discrete centimeter to decimeter intervals of fining-upward nannofossil foraminifer oozes and nannofossil-bearing foraminifer oozes are present at ~63 mcd (Sample 208-1265A-6H-6, 17 cm; 55.17 mbsf) and ~85.2 mcd (interval 208-1265A-8H-7, 10–35 cm; 75.30–75.55 mbsf) and are interpreted as turbidites or gravity flows. Centimeter-thick horizons of *Braarudosphaera*-dominated nannofossil ooze are present at the centimeter to decimeter scale from ~152.7 to ~162.4 mcd (Core 208-1265A-15H; 133.00–142.64 mbsf). Centimeter-scale mottling produced by finely disseminated to concentrated Mn oxide grains first appears at ~173.2 mcd (Core 208-1265A-17H; 152.00–161.51 mbsf) and increases in abundance markedly downcore.

At the boundary between Subunits IIA and IIB, which is near the Eocene–Oligocene transition at ~190 ± 4 mcd (see **"Biostratigraphy,"** p. 10), MS increases and L* decreases (Fig. F17). The clay mineral assemblage was examined for sediments in the lowermost part of Subunit IIA at ~191.60 mcd (Sample 208-1265A-18H-7, 63 cm; 169.60 mbsf). X-ray diffraction (XRD) diffractogram results are presented in Figure **F18.** The loss of the 7-Å peak in the heated sample compared with the untreated and glycolated samples and the lack of a discernable 14-Å peak indicate an absence of chlorite. All 12- to 15-Å peaks in the untreated sample

F15. Oscillatory patterns in sediment color, L*, and MS, p. 48.

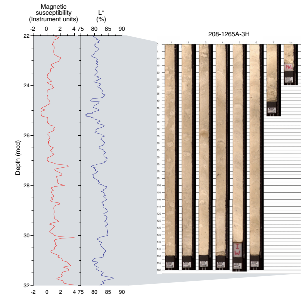

F16. Typical cycles in MS and L*, p. 49.

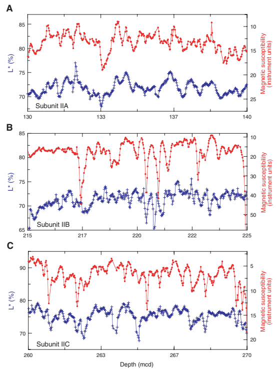

F17. Red-green-blue color variation, L*, and MS across the E/O boundary, p. 50.

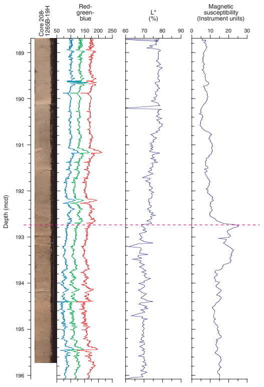

F18. Untreated, heated, and glycolated XRD diffractograms, p. 51.

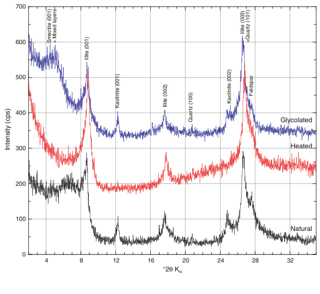

shift to ~10 Å in the heated sample and to 16–20 Å in the glycolated sample, indicating an abundance of mixed-layer smectite. The clay mineral assemblage, therefore, mainly contains illite, kaolinite, smectite, and smectite-relative mixed-layered clays associated with minor quartz and feldspar.

Subunit IIB

Interval: 208-1265A-18H-7, 0 cm, through 23X-7, 23 cm; 208-1265B-19H-3, 105 cm, through 24H-3, 36 cm; 208-1265C-1H-1, 0 cm, through 2H-CC, 32 cm
Depth: Hole 1265A: 169.0–218.2 mbsf (191.0–248.7 mcd); Hole 1265B: 170.3–217.1 mbsf (192.7–248.5 mcd); Hole 1265C: 185.0–204.3 mbsf (208.4–229.9 mcd)
Age: late to early Eocene
Lithology: nannofossil ooze and foraminifer-bearing nannofossil ooze

Subunit IIB is a light gray to very pale brown nannofossil ooze with occasional intervals of foraminifer-bearing nannofossil ooze. The boundary between Subunits IIA and IIB coincides with the interval containing the E/O boundary and is marked by a downhole increase in MS and in a* and b* chromaticity values and by a decrease in L* and red-green-blue values (Figs. F7, F9, F17). Note that because of differential preservation and core recovery, the Subunit IIA/IIB boundary is ~1.75 mcd shallower in Hole 1265A (190.98 mcd) than in Hole 1265B (192.73 mcd) (see **"Biostratigraphy,"** p. 10, and **"Composite Depth,"** p. 4). Subunit IIB is characterized by higher and more variable MS and lower L* relative to Subunits IIA and IIC. These differences may reflect slightly greater clay, ash, and oxide content, although the average carbonate content (94 ± 2 wt%) of Subunit IIB is similar to that of Subunits IIA and IIC. Pronounced oscillations in both sediment L* and MS are present in the upper part of this subunit (Fig. F16B). Relatively large MS variations are generally correlated with higher L* and appear related to the volcanic ash layers in this subunit.

Blebs are rare in the upper ~20 m of Subunit IIB and common in the lower ~30 m. Centimeter-scale mottling, produced by disseminated to highly concentrated Mn oxide nodules, is more abundant than in Subunit IIA. Calcareous dinoflagellate cysts are unusually abundant from ~194.3 to ~204.1 mcd (Core 208-1265A-19H; 171.00–180.82 mbsf) and merit minor modifier status; dinoflagellate cysts are rare in deep-ocean environments and may reflect downslope transport. Distinct centimeter-scale ash-rich layers are common from ~221.3 to 248.7 mcd (Cores 208-1265A-21H through 23H; 190.00–218.96 mbsf) and are indicated by prominent spikes in MS (Figs. F7, F19).

F19. Volcanic ash intervals, Subunit IIB, p. 52.

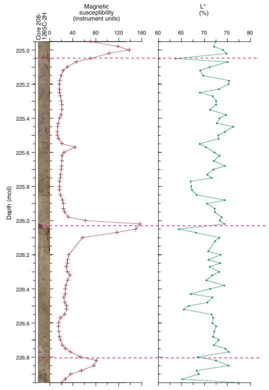

Subunit IIC

Interval: 208-1265A-23H-7, 23 cm, through 36X-CC; 208-1265B-24H-3, 36 cm, through 27H-CC, 10 cm; 208-1265D-1X-1, 0 cm, through 5X-CC, 10 cm
Depth: Hole 1265A: 218.2–312.4 mbsf (248.7–359.5 mcd); Hole 1265B: 217.1–251.9 mbsf (248.5–288.8 mcd); Hole 1265D: 248.0–274.9 mbsf (285.9–315.9 mcd)
Age: early Eocene to late Paleocene
Description: nannofossil ooze and foraminifer-bearing nannofossil ooze

Subunit IIC consists of light gray to white nannofossil ooze and is differentiated from Subunit IIB by lower MS and a step increase in L* (Fig. F7). Subunit IIC is characterized by an initial downcore increase in MS that peaks at ~316 mcd and then decreases through ~327.2 mcd (Sample 208-1265A-32H-5, 55 cm). L* shows a similar downcore increase to ~300 mcd and is relatively high through the remainder of the subunit. Carbonate content averages 93 ± 2 wt% when excluding the clay-rich horizon of the P/E boundary interval. Cyclicity represented by generally positive covariation in L* and MS is well developed in Subunit IIC (Fig. F16C).

Blebs and mottling, along with diffuse darker laminae at a centimeter scale, decrease in abundance downcore and are absent below ~294.9 mcd (Section 208-1265A-27H-CC; 257.02 mbsf). To determine the composition of bleb halos and sediment mottling, a millimeter-scale black mottle from ~294.5 mcd (Sample 208-1265A-D-27H-7, 47 cm; 256.47 mbsf) was analyzed by XRD (Fig. F13). The XRD diffractogram indicates calcite as the dominant mineral component but also shows the presence of the Mn oxide lithiophorite ($[Al,Li]MnO_2[OH]_2$), which suggests that bleb halos and sediment mottling comprise submillimeter-scale Mn oxide grains. We note that the prevalence of these Mn oxides generally coincides with intervals of higher interstitial water Mn concentrations (Fig. F20).

F20. Chromaticity, Mn and Fe, and grain density, p. 53.

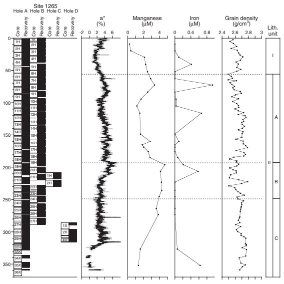

Chalky centimeter-scale layers of nannofossil ooze, as well as siliceous intervals and chert nodules, are first present at ~285 mcd (interval 208-1265A-27H-3, 130–145 cm; 251.3–251.5 mbsf) and are particularly abundant from ~289 to ~299 mcd (Core 208-1265A-27H; 247.00–257.02 mbsf). A partially silicified limestone layer is present at 354.13–354.23 mcd (interval 208-1265A-35X-5, 65–75 cm; 308.35–308.45 mbsf). Hole 1265A ends at 359.93 mcd (Section 208-1265A-36X-CC; 312.41 mbsf) with a chert gravel to coarse sand, an artifact produced by XCB drilling. From this, we infer an increase in chert abundance in the lowermost part of Hole 1265A. A porcellanite nodule from 292.65 mcd (Section 208-1265A-27H-12; 254.62 mbsf) was examined to determine its mineral composition using optical microscopy and bulk XRD analysis. Optical microscopy revealed siliceous material characterized by calcite crystal habits, whereas the bulk XRD diffractogram shows quartz and opal-CT as major mineral components with a minor calcite component (Fig. F21). Thus, the presence of opal-CT pseudomorphs suggests that this porcellanite formed by diagenetic replacement of calcium carbonate rather than as a cement. Given the paucity of biosiliceous components in Leg 208 sediments, a likely source of silica for this porcellanite and chert could be volcanic ash dissolution or silicate weathering in underlying basement rock. This interpretation is consistent with frequent volcanic ash layers in Subunits IIB and IIC (Fig. F7) and increased downcore silicon contents in interstitial waters (see **"Geochemistry,"** p. 22).

F21. XRD diffractogram and image of a "proto-chert" nodule, p. 54.

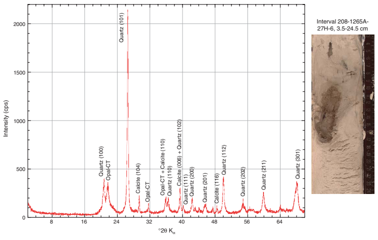

F22. Digital image, MS, and chromaticity of a clay layer, p. 55.

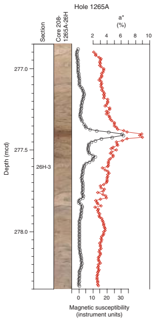

Peaks in MS and chromaticity a* coincide with a ~5-cm interval of reddish nannofossil clay at 277.4 mcd (interval 208-1265A-26H-3, 53–58 cm), which likely corresponds to a similar clay-rich layer (Chron C24n clay layer) recovered in early Eocene sediments from Sites 1262, 1263, 1266, and 1267 (Fig. F22). The presence of this horizon, if truly time coincident and depth variable, may indicate a rapid but short-lived event of carbonate dissolution or nondeposition.

The P/E boundary interval was recovered in Hole 1265A at ~315.87 mcd (Sample 208-1265A-29H-7, 71 cm; 275.09 mbsf), whereas only the lowermost Eocene was recovered from the base of Hole 1265D at

~315.88 mcd (Sample 208-1265D-5H-CC, 10 cm; 274.90 mbsf). The P/E boundary interval occurs at the contact between underlying Paleocene nannofossil ooze and a reddish brown nannofossil clay of the lowermost Eocene (Fig. F23). This is accompanied by a dramatic upcore increase in MS and chromaticity a* and decrease in carbonate content. Nannofossil ooze of the underlying Paleocene averages 85–90 wt% carbonate and decreases abruptly to ~30 wt% at the boundary. Following the sharp increase in values above the boundary, MS gradually returns to lower baseline values in a stepped fashion over a 50-cm interval. A similar progression is seen in both carbonate content and chromaticity a* as the sediment composition changes from nannofossil clay at the boundary, upward into clay-bearing nannofossil ooze, and finally to very pale brown nannofossil ooze. This marked decline in carbonate content across the P/E boundary likely represents a basin-wide dissolution event, developing in response to a shoaling of the CCD. Given that carbonate content decreases to ~0 wt% at Site 1263, a site of shallower paleodepths, we would expect similarly low carbonate contents at Site 1265. Therefore, it is probable that the lowermost Eocene may not have been completely recovered in either Hole 1265A or Hole 1265D.

BIOSTRATIGRAPHY

At Site 1265, Pleistocene through upper Paleocene sediments were recovered. Nannofossils are present in all samples with generally moderate preservation, and reworking occurs in lower Miocene, lower Oligocene, and upper and middle Eocene samples (Fig. F24). Planktonic foraminifers are present at moderate to high abundances with variable preservation. In the lower Miocene through middle Eocene, reworking is common and preservation is moderate to poor, particularly in lowermost Oligocene through middle Eocene samples (Fig. F24). Benthic foraminifers are rare and have good preservation in the upper and lower part of the section; between 43 and 257 mcd (upper Miocene through uppermost lower Eocene), they are common to abundant and have variable preservation because of extensive downslope transport and reworking. Samples from this interval contain common large ostracods and common to abundant echinoid spines.

Examination of calcareous nannofossils and planktonic foraminifers permitted preliminary zonal and stage assignments (Fig. F24; Tables T5, T6, T7, T8). Biochronological ages plotted against depth (mcd) delineate overall sedimentation rates (Fig. F25) (see "Age Model and Mass Accumulation Rates," p. 31). Unconformities are present at the Miocene/Pliocene boundary and in the middle Eocene, but the lower Eocene through upper Paleocene section appears to be complete at shipboard biostratigraphic resolution. Benthic foraminifers indicate upper abyssal depths (2000–3000 m) from the middle Eocene through the Pleistocene. The paleodepth could not be ascertained for the early Eocene and was lower bathyal (~1500–2000 m) during the late Paleocene.

Calcareous Nannofossils

Calcareous nannofossil assemblages were examined in core catcher samples from all holes and from additional samples within cores from Hole 1265A (Table T5). Depths and age estimates of key biostratigraphic events are shown in Table T6. Nannofossils are abundant to common

F23. Digital image, carbonate, MS, and chromaticity across the P/E boundary, p. 56.

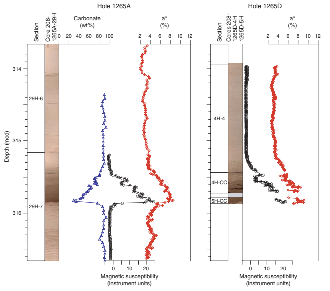

F24. Planktonic foraminiferal and calcareous nannofossil biozonation, p. 57.

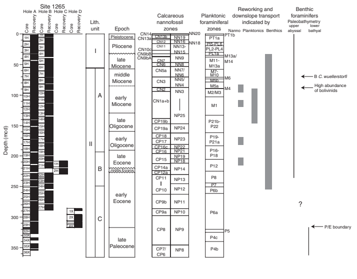

T5. Selected calcareous nannofossil datums, p. 92.

T6. Range and abundance of calcareous nannofossils, p. 94.

T7. Selected planktonic foraminiferal datums, p. 95.

T8. Range and abundance of planktonic foraminifers, p. 96.

F25. Sedimentation rates, p. 58.

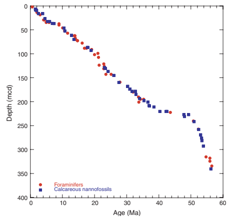

through the recovered section and have varying preservation. The Pliocene–Pleistocene assemblages in Cores 208-1265A-1H through 3H and 208-1265B-1H through 3H consist of abundant nannofossils with good preservation. From Core 208-1265A-4H to the bottom of the hole, nannofossil preservation deteriorates and the assemblages show variable degrees of dissolution and overgrowth.

Pleistocene–Pliocene (0 to ~33 mcd)

The Pliocene/Pleistocene boundary is placed at 8.5 mcd, between the lowermost occurrence (B) of medium *Gephyrocapsa* spp. and uppermost occurrence (T) of *Discoaster brouweri*. Sample 208-1265C-1H-1, 1 cm, contains an upper Pleistocene assemblage of Zone CN14 (NN20). Section 208-1265A-1H-CC contains an upper Pliocene assemblage of Subzone CN12d (NN18). Sections 208-1265A-2H-CC and 3H-CC are placed in lower Pliocene Zone CN11 and Subzone CN10c, respectively. The presence of the upper Miocene ceratolith *Nicklithus amplificus* in Sample 208-1265A-4H-1, 15 cm, indicates that the Miocene/Pliocene boundary is at ~32.7 mcd within an unconformity spanning a time interval of at least 0.9 m.y. and corresponds to Subzones CN10b through CN9bC.

Miocene (~33–129 mcd)

Within Core 208-1265A-4H, assemblages of some of the Miocene Subzones CN9bB through CN1c (NN11 through NN2) were observed. From 54 to 85 mcd, the regular biostratigraphic succession is disturbed by numerous turbidite layers and intense reworking of lower Miocene and Eocene nannofossils into the middle Miocene assemblages (e.g., in samples from Section 208-1265A-6H-6 and Cores 208-1265A-8H and 7H). From 76 to 128 mcd, the nannofossil assemblages are partially dissolved but contain the lower Miocene biostratigraphic markers *Sphenolithus belemnos* in Core 208-1265A-9H and *Sphenolithus disbelemnos* in Cores 208-1265A-11H and 12H, respectively. Abundant placoliths (*Cyclicargolithus* spp.) and strongly overgrown discoasterids, probably belonging to *Discoaster deflandrei* gr., are also present. Other lower Miocene markers such as *Discoaster druggii* and *Triquetrorhabdulus carinatus* are absent or very rare. The assemblages in this interval do not show intense reworking. The presence of *S. disbelemnos* in Sections 208-1265A-10H-CC and 11H-CC (107.3–118.6 mcd) and the range of *Sphenolithus delphix* from Section 208-1265A-12H-CC through Sample 208-1265A-13H-1, 70 cm (129.1–130.6 mcd), and in Core 208-1265B-13H indicate that the O/M boundary is at ~129 mcd.

Oligocene (129 to ~190 mcd)

Sample 208-1265A-12H-CC through Core 208-1265A-18H are Oligocene, with sediments in the interval from Section 208-1265A-12H-CC through Sample 15H-5, 70 cm, representing the upper Oligocene Subzone CN1a+b and Zone CP19 (NN1–NP24), as indicated by the presence of *Sphenolithus ciperoensis* and *Sphenolithus distentus*. Lower Oligocene Zones CP18, CP17, and CP16 (NP23–NP21) were recognized in the interval from Sample 208-1265A-15H-5, 137 cm, through Section 18H-CC. Major components of the assemblages are *Dictyococcites* spp., *Sphenolithus predistentus, Sphenolithus moriformis, Zygrhablithus bijugatus,* and *Cyclicargolithus* spp., with reworked upper Eocene forms. A nannofossil assemblage with abundant *Braarudosphaera bigelowii* occurs in discrete layers in Sections 208-1265A-15H-2, 15H-4, and 15H-6 (154.9, 157.6, and 161.0 mcd, respectively). Similar "*Braarudosphaera* layers" occur in coeval sediments in the upper part of Zone CP18 (NP23) at Site 1264.

Eocene/Oligocene Boundary Interval (185–194 mcd)

The major nannofossil events that characterize the Eocene–Oligocene transition were recognized in Cores 208-1265A-18H through the uppermost part of 19H, with the biostratigraphic signal partially blurred by reworking of lower Eocene nannofossils. The boundary between Subzones CP16c and CP16b (NP22/NP21), the T of *Ericsonia formosa,* is distinct. Rare specimens of *Isthmolithus recurvus* occur in Zones NP22 and NP21. The highest occurrence of *Discoaster saipanensis* defines the boundary between Subzone CP16a and Zone CP15 (NP21/NP20) and is recorded between Section 208-1265A-18H-CC and Sample 19H-1, 30 cm, whereas the highest occurrence of *Discoaster barbadiensis* was difficult to locate because the species is rare and occurs discontinuously. The highest occurrence of *D. saipanensis* places sediments below ~190 mcd in the uppermost Eocene.

Eocene (190–316 mcd)

Major components of the diverse Eocene assemblages in Cores 208-1265A-20H through 29H are *Chiasmolithus* spp., *Coccolithus eopelagicus, Dictyococcites* spp., *Discoaster* spp., *Ericsonia* spp., *Reticulofenestra umbilicus, Reticulofenestra dictyoda, Sphenolithus* spp., and *Z. bijugatus*. Dissolution and overgrowth of *Discoaster* specimens are common and hamper the identification of taxa in some samples. Unconformities are present in the middle Eocene. One unconformity representing at least 3.2 m.y. occurs in Core 208-1265A-20H because the T of *Chiasmolithus grandis* (37.1 Ma) occurs in Section 208-1265A-20H-3, and the B of *Dictyococcites bisectus* (38.5 Ma) and the B of *Dictyococcites scrippsae* (40.3 Ma) both occur in Section 208-1265A-20H-4. Another unconformity, spanning ~7 m.y. of Zones CP14–CP13 (NP16–NP15), occurs in Core 208-1265A-21H between 216.0 and 224.9 mcd.

The lower Eocene zonal boundaries could be recognized (Fig. F24) in Cores 208-1265A-22H through 29H, with the exception of the Zone CP11/CP10 boundary. The marker species of this boundary, *Toweius crassus,* is present in older sediments within Subzone CP9b and thus is not a reliable marker, as observed at other Leg 208 sites. Lower Eocene assemblages have moderate preservation, consistent reworking of Paleocene taxa, and are dominated by overgrown specimens of *Tribrachiatus orthostylus, Sphenolithus radians, Z. bijugatus,* and discoasters (e.g., *Discoaster lodoensis, Discoaster diastypus,* and *Discoaster multiradiatus*).

Paleocene/Eocene Boundary Interval (290–316 mcd)

As at other Leg 208 sites, the nannofossil assemblage at the Paleocene–Eocene transition is characterized by common specimens of *Rhomboaster cuspis* and *Rhomboaster calcitrapa,* which provide a distinct nannofossil biostratigraphic signal. Poorly preserved specimens of the *Rhomboaster–Tribrachiatus* plexus that precede the lowest occurrence of the lowermost Eocene marker *T. orthostylus* have rare and scattered occurrences in Cores 208-1265A-26H through 29H and are often difficult to recognize because of overgrowth; therefore, they cannot be used to confidently define the boundaries between Subzones CP9b and CP9a (NP11/NP10) and Subzone CP9a and Zone CP8 (NP10/NP9). The lowest occurrence of *S. radians* in Section 208-1265A-26H-2 (~275.5 mcd) and the lowest occurrence of *D. diastypus,* the marker of the base of Subzone CP9a in Sections 208-1265A-27H-5 and 27H-6 (~292 mcd), have been used to approximate the boundaries between Subzones CP9b and CP9a (NP11/NP10) and Subzone CP9a and Zone CP8 (NP10/NP9). In the sediments just above the benthic extinction event (BEE) (Sections 208-1265A-27X-2 through 34X-1), the genus *Fasciculithus* shows a distinct distribution pattern in the uppermost part of its range, with a decrease in relative abundance (between Samples 208-1265A-29H-6, 100 cm, and 29H-7, 15 cm) coincident with an increase in relative abundance of *Z. bijugatus* just above the BEE, as also observed at Site 1262. The highest occurrence of the genus *Fasciculithus* is within Section 208-1265A-29H-3.

Paleocene (316–359 mcd; bottom of the hole)

Paleocene assemblages placed in Zones NP9 and NP8 (CP8 and CP7) are present in the lower part of the record at Site 1265 (Cores 208-1265A-30X through 36X and 208-1265C-5X). The assemblages are generally diverse and moderately preserved and consist mainly of common *Discoaster* taxa (*D. multiradiatus, Discoaster nobilis,* and *Discoaster mohleri*) and *Toweius* spp., *Coccolithus pelagicus, Prinsius* spp., *Chiasmolithus* spp., *Cruciplacolithus* spp., and *Ericsonia* spp. Reworked Cretaceous specimens occur in Core 208-1265A-36X. The lowest occurrence of *D. multiradiatus,* the marker of the base of Zone NP9 (CP8), is between Sample 208-1265A-34X-3, 70 cm, and Section 34X-CC (~340.2 mcd).

Planktonic Foraminifers

Planktonic foraminifers are abundant and generally well preserved in core catcher samples throughout much of the Neogene, but reworking and downslope transport of older microfossils is commonplace in assemblages from the Pliocene through the middle Eocene. Preservation in the Paleogene is highly variable, with middle Eocene through lower Oligocene assemblages exhibiting marked dissolution. Upper Paleocene assemblages from the lowermost part of the section display signs of diagenesis.

Core depths for biochronological datums are reported in Table T7 and incorporated in Figure F25; additional samples from Core 208-1265A-29H were studied through the P/E boundary interval. Shipboard examination of assemblages permitted preliminary determination of the stratigraphic ranges for many Cenozoic planktonic foraminifers (Table T8).

Pleistocene–Pliocene (0–33 mcd)

Section 208-1265A-1H-CC (11.1 mcd) contains a typical Pleistocene temperate water fauna. Common species are *Globorotalia crassaformis, Globorotalia truncatulinoides, Globorotalia tumida, Globoconella inflata, Globigerinoides ruber, Globigerinoides sacculifer, Globigerinella siphonifera, Hirsutella scitula,* and *Neogloboquadrina pachyderma* (dextral). The Pliocene/Pleistocene boundary, as approximated by the base of Subzone

PT1a (2.03 Ma), is placed between Sections 208-1265A-1H-CC (11.1 mcd) and 208-1265B-2H-CC (16.1 mcd) at a depth of ~13.6 mcd.

The presence of *Hirsutella margaritae* and the absence of *Globigerina nepenthes* indicate that Section 208-1265A-2H-CC (21.3 mcd) belongs to Zone PL2 (3.88–4.37 Ma). Other taxa common in Section 208-1265A-2H-CC are *Dentoglobigerina altispira, Sphaeroidinellopsis* spp., *Globorotalia tosaensis, G. sacculifer, Globigerinoides extremus, Globigerina bulloides, Orbulina universa, G. inflata,* and *Globoconella conomiozea.* Thus, the upper Pliocene (Zones PL3–PL6) is either confined to a condensed interval within Core 208-1265A-2H or is missing.

The uppermost occurrence of *G. nepenthes* (4.37 Ma) is between Sections 208-1265A-2H-CC and 3H-CC at ~26.6 mcd. The presence of *Hirsutella cibaoensis, Globorotalia plesiotumida,* and *G. extremus* and the absence of *Globorotalia lenguaensis* restricts Section 208-1265A-3H-CC (31.9 mcd) to Zones PL1/M14 (4.37–6.0 Ma). Unfortunately, the biostratigraphic position (Section 208-1265A-3H-CC) could not be further refined because of the scarcity of the marker *G. tumida* and the elimination of Subzone PL1a (Lourens et al., in press).

Miocene (30–129 mcd)

Section 208-1265A-4H-CC (42.5 mcd) is ascribed to Subzone M13a based on the presence of *Neogloboquadrina acostaensis* and *G. lenguanensis,* and the absence of both *G. extremus* and *G. plesiotumida,* restricting the age of Section 208-1265A-4H-CC to 8.49–9.89 Ma. The co-occurrence of *Paragloborotalia siakensis* and *G. nepenthes* indicates that Section 208-1265A-5H-CC (54.32 mcd) is older than 10.7 Ma but younger than 11.64 Ma. Thus, Section 208-1265A-5H-CC is assigned to Zone M11 of the middle Miocene.

The lowermost occurrence of *Fohsella peripheroacuta* (14.02 Ma) is between Sections 208-1265A-6H-CC and 7H-CC at ~70.0 mcd. The presence of *F. peripheroacuta, Fohsella peripheroronda, Menardella praemenardii, Orbulina* spp., *Sphaeroidellopsis* spp., *Globigerina woodi,* and *Globoconella miozea* indicates that Section 208-1265A-6H-CC belongs to Zone M7. Section 208-1265A-7H-CC (~75.0 mcd) is below the lowermost occurrence of *Orbulina* spp. but above the B of *Praeorbulina glomerosa* and is assigned to Subzone M5b (14.7–16.2 Ma). *Globigerinoides sicanus* occurs in Section 208-1265A-8H-CC (85.74 mcd), and its descendant taxa (*P. glomerosa* and *Orbulina suturalis*) are absent. This sample is therefore assigned to Subzone M5a, and the B of *G. sicanus* is between Sections 208-1265A-8H-CC and 9H-CC at ~91 mcd, but the middle Miocene (Subzone M5a through Zone M12) sequence in Cores 208-1265A-6H through 9H contains slumps, making age assignments difficult.

Specimens referable to *Catapsydrax dissimilis* are present in Section 208-1265A-9H-CC, suggesting that its uppermost occurrence (17.51 Ma) is at ~91 mcd. The overall absence of the marker *Globigerinatella insueta* from Site 1265 precludes differentiation of Zones M2 and M3, but the presence of *Globoquadrina binaiensis* (19.08–19.98 Ma) corroborates assigning Section 208-1265A-9H-CC to Zone M2. The apparent juxtaposition of Subzone M5a and Zone M2 at ~91 mcd suggests that the section within Core 208-1265A-9H is condensed. The co-occurrence of *Globoquadrina dehiscens* and *Paragloborotalia kugleri* in Sections 208-1265A-10H-CC (107.27 mcd) and 11H-CC (118.63 mcd) places them in Subzone M1b (21.03–21.44 Ma).

Oligocene/Miocene Boundary Interval (120–140 mcd)

The O/M boundary interval includes the lowermost subzone of the Miocene (M1a) and the uppermost zone of the Oligocene (P22). Section 208-1265A-11H-CC is assigned to Subzone M1a based on the presence of *P. kugleri* and the absence of *G. dehiscens*. This sample, however, displays extensive reworking as evidenced by the presence of lower Eocene morozovellids. The extreme scarcity of *P. kugleri* in Section 208-1265A-12H-CC is a strong indication that the O/M boundary is near this sample at ~129 mcd, in agreement with calcareous nannofossil evidence (see **"Calcareous Nannofossils,"** p. 10). Section 208-1265A-13H-CC (~140 mcd) contains a typical Zone P22 assemblage of well-preserved *Globoquadrina globularis, Globoquadrina tripartita, Globigerina angulisuturalis,* and *G. ciperoensis* and no *P. kugleri*.

Oligocene (129–187 mcd)

Section 1265A-14H-CC (150.38 mcd) is assigned to Subzone P21b based on the co-occurrence of *G. angulisuturalis, G. ciperoensis, Globoquadrina selli,* and *G. tripartita*. The presence of abundant *Chiloguembelina cubensis* at 162.34 mcd indicates that the lower/upper Oligocene boundary is between Sections 208-1265A-14H-CC and 15H-CC at ~156 mcd.

Preservation declines dramatically downhole, and the assemblage in Section 208-1265A-16H-CC consists largely of shell fragments. This foraminiferal "hash" does, however, contain a few thick-shelled specimens of *Subbotina angiporoides,* indicating an age >30 Ma. Section 208-1265A-16H-CC (171.54 mcd) is tentatively assigned to Zone P19. Preservation improves in Section 208-1265A-17H-CC (182.69 mcd), which contains rare "*Globigerina*" *ampliapertura* and *Pseudohastigerina* spp. but also numerous reworked specimens of *Globigerinatheka* spp., *Acarinina* spp., and *Morozovella* spp. Hence, Section 208-1265A-17H-CC is assigned to Zone P18.

Eocene/Oligocene Boundary Interval (182–204 mcd)

The E/O boundary record suffers from extensive reworking and severe dissolution and spans Zones P18–P16 (Sections 208-1265A-17H-CC through 19H-CC; 182.7–204.1 mcd). Section 208-1265A-17H-CC contains a lowermost Oligocene (Zone P18) assemblage. The assemblage in Section 208-1265A-18H-CC (190.0 mcd) is poorly preserved and contains abundant spines of *Hantkenina* spp., as well as thick-shelled *Globigerinatheka* spp. that are likely reworked. It also contains extremely rare specimens of poorly preserved *Turborotalia cerroazulensis cunialensis,* which is indicative of a latest Eocene age. Consequently, the E/O boundary is placed within Core 208-1265A-18H and likely coincides with the lithologic change at 191.0 mcd (see **"Subunit IIB,"** p. 8, in "Unit II" in "Description of Lithostratigraphic Units" in "Lithostratigraphy"). Sections 208-1265A-18H-CC and 19H-CC are assigned to Zone P16 based largely upon the abundance of *Globigerinatheka* spp. and hantkeninid spines, although this interval has been extensively reworked. Other faunal elements of Section 208-1265A-19H-CC include *S. angiporoides, Subbotina linaperta, Pseudohastigerina* spp., and *Hantkenina alabamensis*.

Eocene (191–316 mcd)

An incomplete Eocene record was recovered in Cores 208-1265A-19H through 29H. Acarininid diversity is high in Section 208-1265A-20H-CC (~212 mcd), which contains *Acarinina bullbrooki, Acarinina spinuloinflata, Acarinina topilensis, Acarinina rohri,* and *Acarinina crassata.* Also preserved in this sample are *"Globigerinatheka" senni, Globigerinatheka index, Globigerinatheka subconglobata, Morozovella spinulosa, H. alabamensis,* and *Subbotina inaequispira.* The general absence of the marker *Orbulinoides beckmanni* precludes identification of Zone P13, hindering differentiation of Zones P12 and P14, so Section 208-1265A-20H-CC is loosely assigned to Zones P12–P14. A P12/P14 zonal boundary designation for Section 208-1265A-20H-CC suggests that the middle/upper Eocene boundary may be incomplete (Fig. **F24**).

A more significant unconformity separates Sections 208-1265A-20H-CC and 21H-CC (Fig. **F24**). Section 208-1265A-21H-CC (225.43 mcd) contains abundant well-preserved *Morozovella aragonensis*/*Morozovella caucasica,* as well as *Subbotina lozanoi, "G." senni,* and assorted acarininids (e.g., *A. bullbrooki* and *A. spinuloinflata*). This assemblage typifies Zone P9/P10, which corresponds to the lower/middle Eocene boundary (~49 Ma). Thus, both the upper and lower boundaries of the middle Eocene are marked by unconformities, which is in agreement with calcareous nannofossil data (see **"Calcareous Nannofossils,"** p. 10). Section 208-1265A-22H-CC (238 mcd) is assigned to Zone P9 and contains an assemblage similar to that found in Section 21H-CC, although less well preserved.

Section 208-1265A-23H-CC (~250 mcd) contains a well-preserved assemblage with a suite of morozovellids including *Morozovella subbotinae, Morozovella gracilis, Morozovella lensiformis, M. aragonensis,* and *Morozovella aequa.* The presence of transitional forms linking *M. aragonensis* to ancestral *M. lensiformis* indicates that this sample can be assigned to Zone P7. The absences of *A. spinuloinflata* and *A. bullbrooki* distinguish Section 208-1265A-23H-CC from overlying samples.

Assemblages in Samples 208-1265B-25H-1, 66 cm, and 25H-1, 78 cm, across a distinctive clay layer at ~257.3 mcd indicate that the uppermost occurrence of "large" (>150 µm) biserial planktonic species and the zonal boundary between Subzone P6b and Zone P7 may be correlative with this layer. Thus, Sample 208-1265B-25H-1, 66 cm (257.3 mcd), is assigned to Zone P7 and Sample 208-1265B-25H-1, 78 cm (257.4 mcd), is assigned to Subzone P6b. Section 208-1265A-24H-CC (~261.0 mcd) is also assigned to Subzone P6b based on the absence of *M. aragonensis* and the presence of *Morozovella marginodentata, M. gracilis/Morozovella formosa* morphotypes, and "large" biserial taxa.

Sections 208-1265A-25H-CC through 27H-CC (272.0–295.0 mcd) contain well-preserved assemblages that are typical of Subzone P6a. Some of the more common species are *M. subbotinae, M. gracilis, M. aequa, Acarinina soldadoensis, Acarinina coalingensis, Igorina broedermanni, Subbotina triangularis, Subbotina velascoensis,* and *Globanomalina planoconica.* Diminutive high-spired acarininids tentatively ascribed to *Acarinina chascanona* and "large" biserial forms are also present.

P/E Boundary Interval (295–317 mcd)

This critical boundary interval is confined to Zone P5 between Sections 208-1265A-28H-CC and 29H-CC. Additional samples were taken from Core 208-1265A-29H to increase stratigraphic resolution across the P/E boundary at ~315.8 mcd. The top of Zone P5 could only be approximated because of the overall scarcity of *M. velascoensis*. Section 208-1265A-28H-CC (~306 mcd) contains a well-preserved, diverse assemblage composed of assorted morozovellids, acarininids, subbotinids, globanomalinids, igorinids, and “large” biserial species. Preservation declines downhole from 315.24 to 315.81 mcd. Carbonate content decreases, and planktonic foraminiferal shells are mostly fragmentary and diminutive. Preservation improves immediately below the P/E boundary clay layer (315.86–316.44 mcd) as diversity and shell sizes increase within these uppermost Paleocene assemblages. No P/E boundary “excursion” taxa were seen within this series of samples. Section 208-1265A-29H-CC (~317 mcd) contains a diverse, well-preserved assortment of morozovellids, acarininids, subbotinids, globanomalinids, and igorinids.

Paleocene (316–355 mcd)

Preservation throughout the upper Paleocene is variable but generally declines downhole. Sections 208-1265A-29H-CC through 31H-CC are assigned to Zone P5. The assemblages are dominated by acarininids, although members of the genera *Globanomalina* and *Morozovella* are common. *Globanomalina pseudomenardii* has its uppermost occurrence (delimiting the zonal boundary between Subzone P4c and Zone P5; 55.9 Ma) between Sections 208-1265A-31H-CC and 32H-CC at ~324 mcd. The lowermost Section 208-1265A-35X-CC at ~355 mcd is from a chalky interval that belongs to Subzone P4a. The assemblage contains *G. pseudomenardii, Acarinina subsphaerica, Acarinina nitida, Acarinina mckannai, Igorina tadjikistanensis, M. velascoensis, Morozovella acutispira,* and *Morozovella acuta.*

Benthic Foraminifers

All core catcher samples from Holes 1265A and 1265D were semiquantitatively investigated for benthic foraminifers. In addition, samples were studied from the mudline and from intervals in Hole 1265B that were not recovered in Hole 1265A and across the P/E boundary in Hole 1265C (Table T9).

T9. Selected benthic foraminifers, p. 97.

In many samples, benthic foraminifers are rare compared to planktonic foraminifers, with the exception of those in the lowermost Eocene, where the assemblages have suffered strong dissolution. In addition, benthic foraminifers are more common in many samples between 43 and 257 mcd (Sections 208-1265A-4H-CC and 23H-CC) (Table T9). In these samples, preservation is extremely variable and very large thick-walled specimens are broken and/or abraded, whereas small thin-walled specimens are well preserved. Many of these samples contain reworked planktonic and/or benthic foraminifers, and the benthic faunas indicate downslope transport. Typical indicators of downslope transport are abundant large siphonodosariid species (e.g., *Siphonodosaria pomuligera*), large nodosariids, large specimens of *Oridorsalis umbonatus, Globocassidulina subglobosa, Vulvulina spinosa,* and *Plectofrondicularia paucicostata* (Table T9). The latter species has been recorded as *Plectofrondicularia lirata* in the upper Eocene at several South Atlantic DSDP sites to the east and west of the Mid-Atlantic Ridge over a large depth range and may represent downslope transport at many of these sites (Tjalsma, 1983; Clark and Wright, 1984). At Site 1265, the species occurs in foraminiferal turbidites in the upper Eocene through Miocene.

Benthic foraminiferal assemblages from Site 1265 indicate deposition at upper abyssal depths (2000–3000 m) in samples from above 238 mcd (Cores 208-1265B-1H through 208-1265A-22H; middle Eocene and younger), although for some samples paleodepths could not be determined because of downslope transport (Table T9). Paleodepths could not be estimated for samples between 250 and 275 mcd (Section 208-1265A-23H-CC through Sample 34X-1, 27–28 cm; lower Eocene) because benthic foraminifers are not reliable depth indicators for that period (Müller-Merz and Oberhänsli, 1991). Samples below 275 mcd (upper Paleocene) were deposited at lower bathyal depths (~1500–2000 m).

Benthic foraminiferal assemblages between 0 and 2 mcd (Samples 208-1265B-1H-1, 0–2 cm, and 208-1265A-1H-1, 0–2 cm) contain assemblages with common *Epistominella exigua, Cassidulina laevigata, G. subglobosa, Cibicidoides wuellerstorfi, Cibicidoides mundulus, O. umbonatus,* and *Pyrgo* spp., with few specimens of the *Uvigerina peregrina* group, *Pullenia* spp., *Bulimina rostrata, Bolivinita pseudothalmanni,* and *Gyroidinoides* spp., and rare *Hoeglundina elegans;* in contrast to Site 1264, *Osangularia culter* is absent. These samples do not contain pleurostomellid and siphonodosariid species and were probably deposited after the "*Stilostomella* extinction" at 0.65 Ma (Hayward, 2002). At present, similar assemblages occur along Walvis Ridge between ~3000 and 4000 m (Schmiedl et al., 1997). At these depths, bottom waters are derived from northern sources (North Atlantic Deep Water), as indicated by the common presence of *C. wuellerstorfi*. The common occurrence of *E. exigua* indicates seasonally fluctuating primary productivity in the overlying waters.

Assemblages in samples between 4 and 65 mcd (Sections 208-1265B-1H-CC and 208-1265A-6H-CC) resemble those in the upper samples but lack *E. exigua* and contain pleurostomellid and siphonodosariid species in addition to those listed (Table T9). *C. wuellerstorfi* has its lowest occurrence between Sections 208-1265A-6H-CC and 7H-CC (65 and 75 mcd), which is several millions of years before its first appearance at Site 1264. This first appearance is close in time to the first appearance of the species in the Atlantic Ocean at ~13.7 Ma (e.g., Thomas, 1986; age recalculated to the timescale of Leg 208). Samples between 43 and 65 mcd commonly contain evidence of downslope transport and/or reworking (Table T9).

Assemblages between 75 and 198 mcd (Sections 208-1265A-7H-CC through 208-1265B-19H-CC) resemble the assemblages in the higher samples but lack *C. wuellerstorfi* and contain long-lived abyssal to lower bathyal taxa such as *Cibicidoides* spp., *O. umbonatus, Pullenia* spp., and *Siphonodosaria* spp. Typical middle Miocene and younger taxa (e.g., *Bulimina exilis, B. rostrata, B. pseudothalmanni,* and *Sigmoilopsis schlumbergeri*) have their lowermost appearances in this interval, and pre-middle Miocene taxa (e.g., *Anomalinoides spissiformis, Nonion havanense,* and *Bolivinoides huneri*) have their uppermost appearances. Many samples contain evidence of downslope transport and/or reworking (Table T9). The reworked specimens are generally derived from middle bathyal (600–1000 m) or greater depths.

Between 85 and 87 mcd (lower part of Core 208-1265-8H), benthic foraminiferal assemblages contain high relative abundances (>75%) of small smooth-walled bolivinid species, as in coeval sediments at Site 1264. These occurrences reflect an unusual event in benthic foraminiferal faunas at ~18 Ma, which was recognized in the eastern Atlantic and western Indian Oceans and is called the high abundance of bolivinids event (Smart and Murray, 1994; Smart and Ramsay, 1995).

Nuttallides truempyi has its uppermost occurrence in Section 208-1265A-19H-CC (204 mcd). Samples between 204 and 249 mcd (Sections 208-1265A-19H-CC through 23H-CC) contain typical species-rich upper abyssal middle–upper Eocene assemblages, with *N. truempyi, Bulimina semicostata, Cibicidoides praemundulus, Cibicidoides grimsdalei, O. umbonatus, Gyroidinoides* spp., *A. spissiformis, N. havanense,* and common *Siphonodosaria* spp. as well as unilocular, laevidentalinid, and pleurostomellid taxa. Evidence for downslope transport is present throughout this interval (Table T9).

Samples 208-1265A-25H-1, 66–67 cm, through 29H-7, 65–66 cm (257–317 mcd), contain much less species rich assemblages, as is typical for the lower Eocene in the South Atlantic over a large depth range (Clark and Wright, 1984; Müller-Merz and Oberhänsli, 1991; Thomas and Shackleton, 1996). These assemblages are characterized by the presence of rare *Aragonia aragonensis* and small smooth-walled species of *Abyssamina* and *Clinapertina,* small smooth-walled buliminid species (e.g., *Bulimina kugleri* and *Bulimina simplex),* and small specimens of *N. truempyi, O. umbonatus, A. spissiformis,* and *N. havanense. Tappanina selmensis* and *Siphogenerinoides brevispinosa* are rare to common, as are specimens of unilocular, laevidentalinid, and pleurostomellid taxa. Two samples in relatively clay rich intervals at 257.3 mcd (Sample 208-1265B-25H-1, 65–66 cm) and 277.4 mcd (Sample 208-1265A-26H-3, 55–56 cm) contain assemblages with a relatively low species richness and common to abundant *Clinapertina* and *Abyssamina* spp.

In the lowermost part of this interval (315.4–315.8 mcd; Samples 208-1265A-29H-7, 30–31 cm, through 29H-7, 65–66 cm, and Section 208-1265D-4H-CC), species richness is extremely low and long-lived unilocular and laevidentalinid taxa are absent. Abundant taxa are *Abyssamina quadrata, B. kugleri, O. umbonatus,* and *N. truempyi.* The lowermost samples in this interval contain minute specimens of *N. truempyi, T. selmensis, O. umbonatus, B. kugleri, B. simplex,* and *A. quadrata;* most are dominated by *N. truempyi* and one by *O. umbonatus.* Similar assemblages have been described from immediately after the P/E BEE on Walvis Ridge (Müller-Merz and Oberhänsli, 1991; Thomas and Shackleton, 1996).

The BEE occurs between Samples 208-1265A-29H-7, 65–66 cm, and 29H-7, 70–71 cm (315.81 and 315.86 mcd), and between Sections 208-1265D-4H-CC and 5H-CC. At Site 1265, a few very small specimens of species that usually become extinct at the BEE are present in the lower few samples above the event (*Bulimina thanetensis* and *Paralabamina lunata*) (Table T9). The specimens are small and thin walled like the other species in the assemblage and show no signs of reworking.

Samples from below the BEE through the bottom of the hole (317–355 mcd) contain typical extremely species rich Paleocene lower bathyal through abyssal assemblages with *Stensioeina beccariiformis, P. lunata, Paralabamina hillebrandti, Pullenia coryelli,* large thick-walled species of *Gyroidinoides* such as *G. beisseli, G. globosa,* and *G. quadrata,* and large agglutinant taxa (e.g., *Clavulinoides* spp., *Marssonella oxycona,* and *Gaudryina pyramidata*). *Aragonia velascoensis* is rare at Site 1265. As at Site 1263 and in contrast with Site 1262, lower bathyal indicator species such as *Alabamina creta, Bolivinoides delicatulus, Coryphostoma midwayensis,* and *Neoflabellina semireticulata* are present, but they are less common than at Site 1263, indicating lower bathyal depths (1500–2000 m).

PALEOMAGNETISM

Drilling and Core Orientation

Every other core at Site 1265 was recovered with a nonmagnetic core barrel until the first core barrel had to be drilled over (see Table T1; "Operations," p. 2). As at other sites, no obvious difference was noticed in the magnetic data between sediments recovered with the nonmagnetic barrel and those with a standard core barrel. All APC cores in Holes 1265A and 1265B were successfully oriented with the Tensor tool with the exception of Cores 208-1265A-1H and 2H, 208-1265B-1H through 3H, and 22H, 23H, 25H, and 26H (see Table T1; "Operations," p. 2).

Archive-Half Measurements

The archive halves of 70 cores from Holes 1265A, 1265B, 1265C, and 1265D were measured in the pass-through magnetometer. Natural remanent magnetization (NRM) was measured on all cores. Most cores were demagnetized at 10 and 15 mT, with the notable exception of Sections 208-1265A-7H-3 through 18H-2, which were demagnetized only at 15 mT to speed core flow through the core laboratory. As at other sites, a strong vertical overprint was largely removed by demagnetization to 10 mT.

The working half of Section 208-1265B-10H-2 was demagnetized to test the effect of core scraping on the magnetization of soft-sediment split cores. The archive halves are routinely scraped by the sedimentologists with a metal spatula over a plastic film. This is done to remove surface roughness created by splitting, which shows up in the color reflectance data as an artificial darkening of color. To check that this process does not adversely affect the magnetization of the softer sediments, the archive halves of Sections 208-1265B-7H-5 and 7H-6 were measured both before and after smoothing. It was discovered that a dramatic change in both inclination and intensity resulted after smoothing (Fig. F26A, F26B). Following this discovery, an additional section was tested more thoroughly. Section 208-1265B-10H-2 was demagnetized to 15 mT and measured as a whole round. The section was then split, redemagnetized to 15 mT, and remeasured. The archive half was then smoothed with a plastic spatula, and the working half was smoothed with a metal spatula. The halves were then remeasured, redemagnetized to 15 mT, and measured again. The results show no significant differences between the nonsmoothed and smoothed halves (Fig. F26C, F26D). The large increase in magnetization following smoothing seen in Sections 208-1265B-7H-5 and 7H-6 was not observed either. The inclination data from the archive half (Fig. F26C) closely parallel those of the whole round. The working-half data, however, do show some shallowing compared to the whole-round data. It is concluded from this admittedly limited experiment that the smoothing has little to no effect on the magnetization of the split cores but that the splitting process can occasionally have some effect. The test results on Sections 208-1265B-7H-5 and 7H-6 are difficult to explain, but it is suspected that the inclination record from these sections was anomalous to begin with.

F26. Effects of core scraping on magnetization, p. 59.

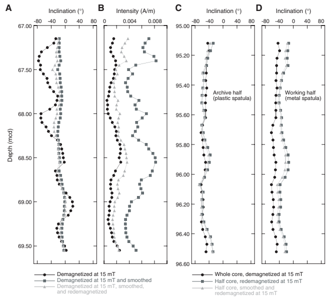

Remanent Magnetization Intensity

The initial NRM before demagnetization of sediments is on the order of 10^{-3} to 10^{-2} A/m and primarily reflects the vertical downward overprint, as at other sites (Fig. **F27**). The overprint is easily removed after alternating-field (AF) demagnetization to 10 mT. After AF demagnetization at a peak field of 15 mT, intensities are reduced by about an order of magnitude (Fig. **F27**).

The interval from 0 to 55 mcd (lithostratigraphic Unit I) is characterized by low initial MS values (Fig. **F28**), a concave trend of depositional remanent magnetization (DRM) (a trough at 20–25 mcd) (Fig. **F27**), and a convex trend of DRM normalized by initial susceptibility (nDRM) (a peak at 20–25 mcd) (Fig. **F29**). Assuming no change in geomagnetic field intensity, this indicates that a magnetic property change resulting from diagenesis and/or magnetic grain-size changes might be gradually developed in this unit. In the interval from 55 to 316 mcd, however, it appears that intensity changes are largely controlled by changes in ferromagnetic concentrations. Below 316 mcd, negative MS values (Fig. **F28**) show that calcite is dominating the MS signal.

Magnetostratigraphy

Portions of the magnetostratigraphy at Site 1265 are relatively good compared to the records from Sites 1263 and 1264. Most of the age-depth tie points (Table **T10**) are taken from Hole 1265A, which generally provides the best inclination record. The Pliocene–Pleistocene data are not particularly well resolved (Fig. **F30A**), but initial estimates of major boundaries roughly agree with the biostratigraphy (see **"Biostratigraphy,"** p. 10) (Table **T5**). The Brunhes/Matuyama boundary (0.781 Ma) is placed at ~3.8 mcd, and it is bracketed by the top of nannofossil datums *Pseudoemiliania lacunosa* (0.46 Ma) at ~2.32 mcd and large *Gephyrocapsa* spp. (1.22 Ma) at ~5.07 mcd. The base of Chron C3n, just above the Miocene/Pliocene boundary, appears to fall in a core gap in Hole 1265A sediments but otherwise is well resolved, and the placement at ~32.9 mcd agrees well with the biostratigraphic placement of the Miocene/Pliocene boundary at ~32.7 mcd (see **"Biostratigraphy,"** p. 10, **"Age Model and Mass Accumulation Rates,"** p. 31, and Table **T17**).

Most of the middle to upper Miocene is condensed or poorly resolved, but the lower Miocene to uppermost Oligocene is characterized by a recognizable polarity sequence that is well resolved for Hole 1265A (Fig. **F30B**). The placement of the top of Chron C6n (18.748 Ma) at ~90.4 mcd was chosen to approximately agree with the bottom of nannofossil datum *S. belemnos* (18.92 Ma) at ~93 mcd. The sequence from Chrons C5En to C6Cn is nicely resolved with the exception of Chron C6AAn and Subchron C6AAr.1n, which appear to be missing or fall in a core gap. Alternatively, the normal chron, tentatively identified as Chron C6An may, in part, be one of these two events. All three short normals in Chron C6Cn are well resolved, allowing the placement of the O/M boundary between ~124.6 and 125.0 mcd; this is offset from the biostratigraphic placement of the boundary at ~129 mcd.

In the Oligocene, the sequence becomes less identifiable and only Chrons C8n and C9n have been tentatively identified (but are not included in the age-depth model) (Table **T18;** Fig. **F48**). As at other sites, Chron C13n is identifiable in sediments from both holes and is constrained by the tops of *E. formosa* and *D. saipanensis*.

F27. Intensities, 0- and 15-mT demagnetization, p. 60.

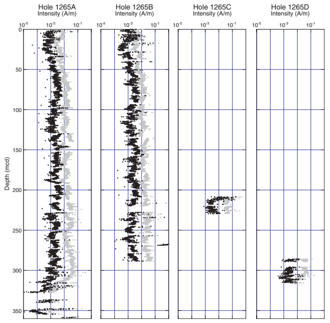

F28. Initial MS, p. 61.

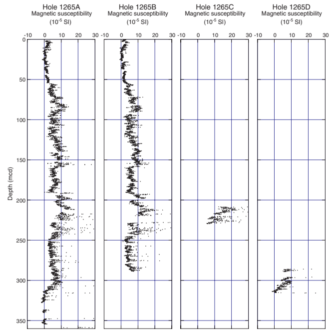

F29. nDRM$_{15\ mT}$, p. 62.

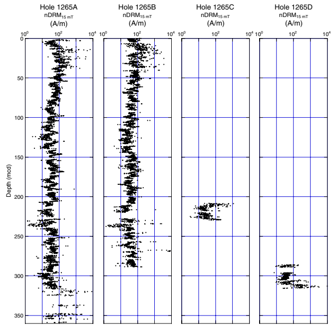

T10. Magnetostratigraphic age-depth tie points, p. 98.

F30. Magnetostratigraphic interpretation, p. 63.

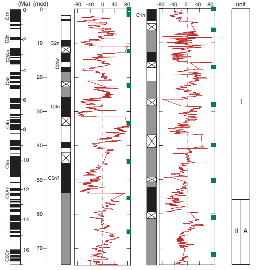

The inclination record in the Eocene shows a bias toward negative values as at other sites, and no attempt to interpret the data in terms of polarity intervals has been made. Below the P/E boundary, however, Chron C24r is well resolved, as is the top of Chron C25n.

GEOCHEMISTRY

Volatile Hydrocarbons

A total of 30 headspace samples from Site 1265 (all from Hole 1265A) were analyzed (Table T11). The concentration of CH_4 (C_1) in most of the samples was at an atmospheric background level (range = 1.6–2.0 ppmv) and did not exceed 2.4 ppmv in any sample. No hydrocarbon gases higher than C_1 were detected.

T11. Composition of headspace gases, p. 99.

Interstitial Water Chemistry

Interstitial waters from 26 samples were collected at Site 1265: 19 from Hole 1265A (9.1–351.9 mcd) and 7 from Hole 1265B (165.2–273.3 mcd). The samples from the two holes were taken to constitute a single depth profile using the composite depth scale. Slight differences in lithology may cause minor breaks in the concentration-depth gradients of some chemical parameters. Chemical constituents were determined according to the procedures outlined in "Geochemistry," p. 23, in the "Explanatory Notes" chapter. Results of the chemical analyses are presented in Table T12.

T12. Results of interstitial water analyses, p. 100.

pH, Salinity, Alkalinity, Chloride, and Sodium

The pH of pore waters at Site 1265 ranges from 7.18 to 7.42 (average = 7.30 ± 0.06) (Table T12). All values are lower than the average seawater value of 8.1, and no distinct depth trend is recognizable. Salinity typically ranges from 34.0 to 35.5 (mean = 35.1 ± 0.4).

Alkalinity is relatively constant with depth (excluding two suspiciously high values of 3.48 mM at 29.7 and 165.2 mcd, plus three anomalously low values of 2.22, 2.17, and 2.25 mM at 9.1, 326.6, and 351.9 mcd, respectively), and the average value is 2.60 ± 0.05 mM (Fig. F31A). Apart from the three anomalously low values, all interstitial water samples have a higher alkalinity than average seawater (2.33 mM; International Association of Physical Sciences of the Ocean certified value).

F31. Chemical constituents in interstitial waters, p. 67.

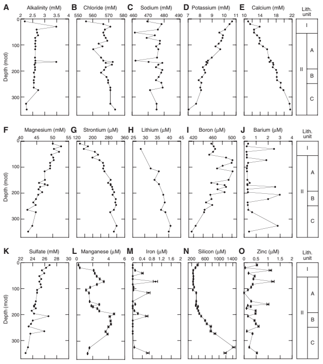

The chloride concentrations at Site 1265 increase from 556 mM at 9.1 mcd and peak at values of ~568 mM between 19.6 and 73.9 mcd (Fig. F31B). Below this chloride peak, concentrations drop to 560 mM at 116.2 mcd and then generally increase downhole to a maximum of 574 mM at the bottom of the section (351.9 mcd). The sodium profile does not exhibit a significant downhole trend, with concentrations varying between 423 and 479 mM (Fig. F31C).

Potassium, Calcium, Magnesium, Strontium, and Lithium

Site 1265 downhole trends in potassium, calcium, and magnesium are consistent with those resulting from exchange with basaltic basement at depth (Gieskes, 1981), with potassium and magnesium decreasing and calcium increasing with depth (Fig. F31D, F31E, F31F). Calcium values increase from 11.0 (9.1 mcd) to 21.5 mM (351.9 mcd) (Fig. F31E). The magnitude of the downhole increase in calcium concentrations (10.5 mM) is larger than those observed at Sites 1262, 1263, and 1264.

The magnesium pore water profile (Fig. F31F) at Site 1265 is characterized by a general decrease with depth from 50.0 mM in the shallowest sample (9.1 mcd) to 42.3 mM at the base of the section (351.9 mcd). Pore water potassium concentrations decrease with depth from 10.7 (9.1 mcd) to 7.0 mM (351.9 mcd) (Fig. F31D).

Strontium concentrations increase downhole from 136 µM in the shallowest sample (9.1 mcd) and peak at values between 277 and 319 µM below 148.7 mcd (Fig. F31G). The strontium pore water profile indicates a source of strontium to the interstitial waters below 148.7 mcd and diffusion of this strontium into the sediments above. This strontium source is most likely the result of the dissolution and recrystallization of carbonates (e.g., Baker et al., 1982).

Lithium concentrations increase gradually from 28.3 µM in the shallowest sample analyzed (29.7 mcd) to 40.0 µM at the base of the section (351.9 mcd) (Fig. F31H). Similar lithium pore water profiles were observed at Sites 1262 and 1263 and also below ~150 mcd at Site 1264. The increase with depth suggests a source of lithium from the sediment to the pore waters.

Boron and Barium

Pore water boron concentrations generally increase from 457 to 501 µM over the depth interval from 9.1 to 72.6 mcd then decrease downhole to a value of 416 µM at the bottom of the section (351.9 mcd) (Fig. F31I). Laboratory experiments under controlled temperatures and pressures have shown that boron is leached from terrigenous sediments into fluids (e.g., James et al., 2003). Likewise, a study of Ocean Drilling Program Leg 186 interstitial water samples (Deyhle and Kopf, 2002) concluded that the removal of boron from clays and volcanic ash was responsible for boron enrichment in the pore waters. Therefore, the pore water boron peak centered at ~72.6 mcd could indicate either increased concentrations of terrigenous sediment or the enhanced dissolution of terrigenous components in this interval.

Pore water barium values fluctuate between 0.19 and 2.97 µM downhole, with a zone of consistently low barium concentrations occurring from 83.5 to 168.8 mcd (Fig. F31J).

Sulfate, Manganese, and Iron

The sulfate pore water profile at Site 1265 displays a slight decrease downhole from 26.8 mM in the shallowest sample (9.1 mcd) to 22.8 mM at the base of the section (351.9 mcd) (Fig. F31K). The sulfate concentrations at Site 1265 (average = 24.7 ± 1.1 mM) are high enough to indicate a lack of sulfate reduction associated with the microbial decomposition of organic matter (e.g., Gieskes, 1981).

The Site 1265 manganese pore water profile (Fig. F31L) increases sharply from 0.22 µM at the top of the section (9.1 mcd) to 2.11 µM at 29.7 mcd. Manganese pore water concentrations continue to rise with depth to peak at a value of 3.38 µM at 72.6 mcd before dropping to values between 1.15 and 1.67 µM in the section spanning from 94.5 to 148.7 mcd. After this interval of low values, pore water manganese increases downhole to peak at values between 3.60 and 4.66 µM from

196.1 to 273.3 mcd before dropping to 1.35 µM at the base of the section (351.9 mcd). Below ~182 mcd, dark grains and nodules were apparent in the sediments. A few large (~600 µm in diameter) nodules incorporating planktonic foraminifer tests were picked from washed core catchers 208-1265A-18H and 27H for geochemical analysis (Fig. **F32**). Similar nodules were analyzed by XRD and found to be composed of calcite and a manganese oxide called lithiophorite (see **"Lithostratigraphy,"** p. 5). The manganese oxide nodules are associated with the peak in pore water manganese between 196.1 and 273.3 mcd, but it is unclear whether the nodules contributed to the enhanced pore water concentrations or the higher values of dissolved manganese in this interval resulted in oxide precipitation. Analysis of the manganese oxide nodule samples is necessary before the chemical composition of the nodules can be used to aid the interpretation of the pore water profiles at Site 1265.

F32. Manganese oxide nodules, p. 68.

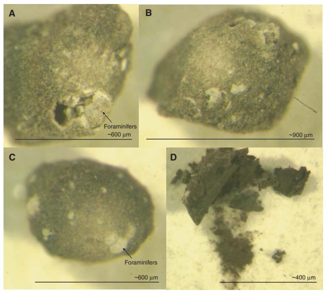

Pore water concentrations of dissolved iron are typically low and often below the detection limit throughout the section (Table **T12;** Fig. **F31M**), but distinct peaks with iron concentrations between 0.41 and 0.94 µM are present at 40.7, 72.6, 116.2, 206.2, and 351.9 mcd.

Silicon and Zinc

Dissolved silicon in pore fluids from Site 1265 decreases slightly from 369 µM at a depth of 9.1 mcd to values of ~250 µM between 29.7 and 105.0 mcd. Below this, silicon concentrations increase to values of ~330 µM between 116.2 and 165.2 mcd before increasing significantly downhole to a peak of 1428 µM at 326.6 mcd. The maximum concentration of dissolved silicon measured in the pore waters of Site 1265 sediments is very similar to that observed at Site 1263 (1498 µM) and is almost three times the maximum observed at Site 1262 and during the study of Leg 74 interstitial waters (Gieskes et al., 1984). Chert deposits were recovered below ~285 mcd (see **"Lithostratigraphy,"** p. 5), and it is possible that chert formation processes contributed to the high dissolved silicon concentrations (Hesse, 1990).

Zinc concentrations are consistently low and vary between 1.2 and 0 µM (below detection limits) (Fig. **F31O**).

Summary of Interstitial Water Chemistry

Although the calcium, potassium, and magnesium interstitial water profiles at Site 1265 suggest that a simple diffusion profile between seawater and basement basalt is responsible for the chemistry of the pore waters, other elements including strontium, lithium, manganese, and silicon indicate that diagenetic processes occurring in the sediments also have a strong impact on the interstitial water chemistry. The pore water profiles of strontium, lithium, boron, and silicon from Site 1265 show remarkable similarities with the same profiles from Site 1263, suggesting similar process are controlling the pore water chemistry at both sites.

T13. Inorganic carbon and calcium carbonate, p. 101.

Sediment Geochemistry

Carbonate determinations by coulometry were made for a total of 182 samples from Site 1265 (Table **T13**). The values for carbonate are generally high (mean = 89.1 wt%) and range from 30.0 to 98.4 wt% (Table **T13;** Fig. **F33**). Closely spaced (every 2 to 10 cm) samples from Hole

F33. Sedimentary carbonate, p. 69.

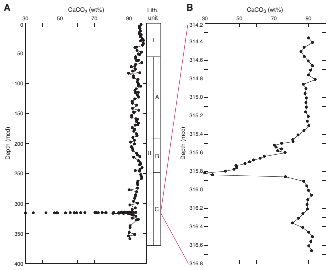

1265A were analyzed for carbonate content across the P/E boundary section (Fig. **F33B**). Carbonate content drops from ~90 to 30 wt% below 316 mcd within <10 cm of sediment. The lowest carbonate values are significantly higher than the 1.33 wt% carbonate values observed in the P/E sediments at Site 1263. Above 315.8 mcd, the carbonate values increase uphole to ~70 wt% over ~30 cm before climbing back to >80 wt%.

Extractable Hydrocarbons

Extraction of organic matter was attempted on several sample residues after squeezing interstitial water. Analyzable amounts of extracts were obtained from 15 to 40 g of carbonate-rich lithologies in Samples 208-1265A-5H-5, 140–150 cm (52.1 mcd), 9H-5, 140–150 cm (94.5 mcd), 14H-5, 140–150 cm (148.7 mcd), and 208-1265B-20H-5, 140–150 cm (206.2 mcd). All samples were extracted in an ultrasonic bath for 12 hr or longer in an attempt to collect heavier compounds.

The aliphatic hydrocarbon fraction of samples was dominated by unidentified branched isoprenoids and mono-unsaturated isoprenoids over C_{12}–C_{22} *n*-alkanes (Fig. **F34**). Regular isoalkanes and anteisoalkanes were not observed. Most of the peaks other than *n*-alkanes remained unidentified; they are divided into two homologous groups based on their mass spectral patterns. Molecules belonging to Group A are saturated hydrocarbons that show mass spectral patterns dominated by m/z $14n + 1$, where n represents the carbon number (Fig. **F34**). Each compound of Group A generally shows a similar mass spectral distribution as *n*-alkanes, which exhibit an exponential decrease of mass fragment abundances for m/z 71 and larger. However, Group A exhibits considerable depression at m/z 91, 141, 183, and 225 and higher abundances at m/z 155 and 169 relative to the *n*-alkane with the same carbon number (Fig. **F35A, F35B**). The m/z 113 from each molecule of Group A characteristically associates with m/z 111, showing twin spectra. Each molecule belonging to Group B is interpreted to be unsaturated. The mass spectral pattern shows prominent abundances at m/z 111 and 153 and a depressed abundance at m/z 97, suggesting similar structure with molecules of Group A in configuration (Fig. **F35C, F35D**).

F34. Mass chromatogram for hexane eluate, p. 70.

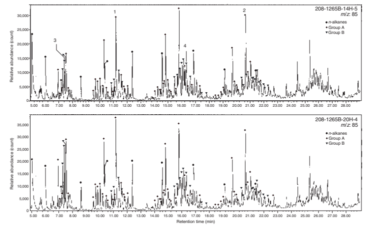

F35. Mass spectra of selected peaks in hexane eluate, p. 71.

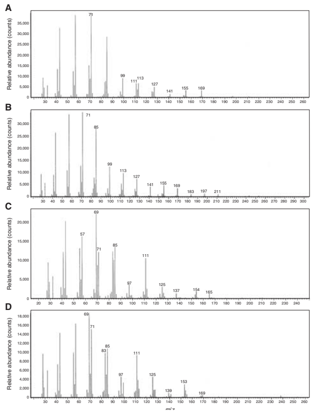

Samples 208-1265A-14H-5, 140–150 cm, and 20H-5, 140–150 cm, showed almost identical total ion chromatograms and mass fragment ratios at m/z 85 of aliphatic hydrocarbons with a predominance of homologous Groups A and B, suggesting that the majority of aliphatic hydrocarbons from these samples have a unique source (i.e., molecules belonging to Groups A and B are most likely from a single contaminant). The samples analyzed here are too lean in extractable organic matter to be accurately characterized under the mask of contamination.

Any long-chain alkanes indicative of terrestrial higher plants, namely n-C_{27-33} with strong odd carbon number preference in hexane eluates, or longer straight-chain alkenones (C_{37} or larger) in dichloromethane eluates were not detected in any samples.

DOWNHOLE MEASUREMENTS

Logging Operations

Following the completion of APC and XCB coring operations (bit size = $11^7/_{16}$ in) in Hole 1265A, the hole was conditioned with a wiper trip and was displaced with 142 bbl of 8.9-lb/gal sepiolite mud. The drill pipe was withdrawn to 69 mbsf in preparation for logging. All three scheduled tool strings were run: the triple combo tool string with the LDEO high-resolution MGT on top and the Temperature/Acceleration/Pressure (TAP) tool on bottom, the FMS-Sonic tool string, and the three-component WST (WST-3) for a checkshot survey (see **"Downhole Measurements,"** p. 27, in the "Explanatory Notes" chapter). A summary of the logging operation, including tools used, is provided in Figure **F36** and Table **T14.** The heave conditions were good, typically <2 m throughout the logging operation. However, the wireline heave compensator stroked out once during the repeat run of the triple combo tool string in Schlumberger mode. A total of four main and two short repeat passes were made with no bridges encountered, and the bottom of the hole was reached on all passes (Fig. **F36**). The tool string rig-up began at 1200 hr on 10 April, and the full operation was completed by 1000 hr on 11 April.

F36. Logging operations summary, p. 72.

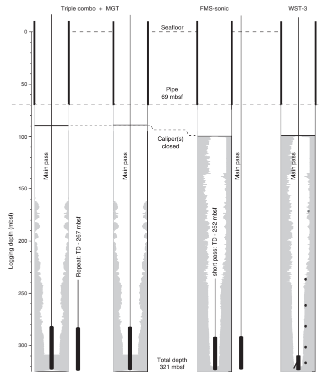

T14. Breakdown of logging operations, p. 102.

The triple combo tool string was run first and was successfully lowered into the bottom of the hole at 321 mbsf logging depth. The triple combo caliper readings suggested that the upper section of the hole was enlarged to 18 in (i.e., wider than the maximum caliper extension). Upon completion of the main pass, a short repeat pass was performed at the bottom of the hole with the neutron source (Accelerator Porosity Sonde [APS]) turned off to prevent activation of gamma radiation before the MGT run. Control of the triple combo tool string was then transferred to the downhole measurements laboratory, and the tool string was again lowered to the bottom of the hole. The formation was logged uphole for one main pass, with the tool string in "Lamont mode" for MGT data acquisition. At the end of this pass, the tool string was retrieved to the rig floor. No TAP tool data were recorded during this run.

The FMS-sonic tool string was rigged up and run to the bottom of the hole. To save time, the main pass was followed by a short pass in the bottom of the hole because the interval of interest was the lower part of the borehole. The FMS images are good in the bottom part of the hole and progressively degrade uphole as the pad contact was on only one axis for most of the hole. The other axis was larger than the 15-in caliper of the FMS-sonic tool string. The Dipole Sonic Imager (DSI) was run in primary (compressional [*P*]) and secondary (shear [*S*]) modes, *P* and *S* monopole and dipole shear modes, and also in first motion detection (FMD) mode. As a result of the slowness of the formation and the large hole size, the *P*-wave velocity logs of the FMD mode are incomplete and the *S*-wave log is not usable. The FMS-sonic tool string was retrieved from the rig floor at 0500 hr on 11 April.

F37. Quality control of downhole logging runs, p. 73.

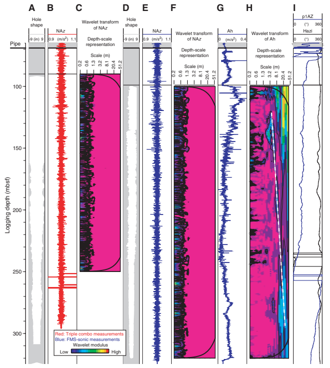

The final tool string, the WST-3, was successfully run to the bottom of the hole. A total of six checkshot stations were acquired with a spacing conditioned by previously defined lithologic changes and hole condition. In summary, three tool strings were run during the logging operation, with four main logging passes. All main passes were from total depth into pipe, providing a logged section of 252 m (Fig. **F36**).

Data Quality

The triple combo caliper indicated that the hole conditions were good in the lower-middle part of the borehole (from total depth, 321 to 210 mbsf). Above 210 mbsf and up to 160 mbsf, the caliper indicated minor localized washouts (Fig. **F37A**). The upper section of the hole, logged with the caliper (160–89 mbsf), is characterized by a hole diameter exceeding the maximum extension of the caliper (18 in). A hole diameter of this magnitude normally would degrade the quality of the data acquired with tools that require contact with the borehole wall (e.g., the density or porosity tools). Remarkably, with the exception of a malfunction of the porosity (APS) sonde at the end of the main pass (from 140 mbsf to pipe depth [69 mbsf]), little evidence of deterioration for data quality exists uphole in these logs.

The tool string accelerometer data from the MGT indicate that stick-slip of the tool remained at low levels through most of the hole except in four short (<1 m) intervals at ~255 mbsf (Fig. F37B). As a further check, a wavelet analysis of the accelerometer data was undertaken. The wavelet transform analysis of the acceleration data allows the multiscale components of the tool acceleration to be deciphered (Fig. F37C). The analyzed record (90–250 mbsf) is characterized by acceleration/deceleration of generally <0.6 m, indicating almost perfect heave compensation during this run. No intervals of intermediate scale (~4 to 7 m), usually attributed to localized stick-slip displacement over washout, were detected. Even without acceleration data for the triple combo tool string in Schlumberger mode, similar results are expected for this tool string.

In the upper part of the hole (99–135 mbsf; calipers closed at 99 mbsf), one axis of the FMS-sonic caliper readings clearly indicates a narrower diameter than that indicated by the triple combo caliper (Fig. F37D). This observation indicates that the hole is elliptical in shape and that hole conditions were better than suggested by the triple combo tool string data. As for the triple combo tool string, vertical acceleration of the FMS-sonic tool string remained at levels characteristic of no stick-slip displacement (Fig. F37E, F37F). Rapid rotation of the FMS-sonic tool string may impair the quality of the microresistivity images. As a quality check, a wavelet analysis of the horizontal acceleration record was undertaken (Fig. F37G). The depth-scale representation is characterized by a progressive decrease in rotation wavelength/smoothness uphole, decreasing from >20 m in the upper part of the hole, to 8 m in the middle interval with washouts (170–210 mbsf), to 3 m above (Fig. F37H). The interval above 140 mbsf shows the highest horizontal acceleration of the record, as only one axis of the FMS-sonic tool string was in contact with the formation. Below 240 mbsf, localized and rapid variations in horizontal acceleration are rare and of low amplitude and do not impair data quality. As a result, the tool orientation is smoothly guided by the change in hole azimuth (Fig. F37I) and the quality of the microresistivity images is good in the bottom part of the hole and progressively degrades uphole.

Because of the low natural gamma radiation (NGR) level of the penetrated formation, the seafloor could not be detected through the pipe. Consequently, the original triple combo logs (main pass) were depth shifted (–3075.0 m) to the seafloor using the upper part (70–120 mbsf) of the total gamma radiation data from the Hostile Environment Natural Gamma Ray Sonde (HNGS) and the NGR data acquired with the whole-core MST (Fig. F38B). The logging data seafloor depth differs by 4.0 m from the seafloor depth determined by the driller. Using this reference scale, the pipe depth was placed at 69 mbsf. Data from the triple combo tool string are good, with excellent repeatability and only minor depth mismatches between the main pass and the short repeat section (Fig. F38C). This earlier run served as a reference by which the features in the equivalent logs of subsequent runs (gamma radiation data from

F38. Depth shifting using NGR logs, p. 74.

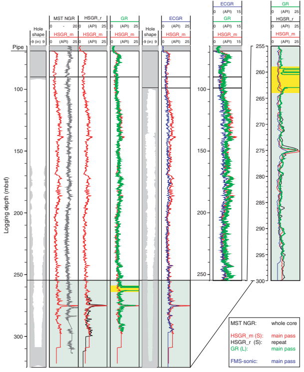

the MGT and environmentally corrected gamma radiation from the Scintillation Gamma Ray Tool [SGT] on the FMS-sonic tool string) were matched (Fig. **F38D, F38F**). In detail, gamma ray data from the HNGS, MGT, and SGT are also well matched, providing easy depth shifting for the MGT and FMS-sonic logging runs (Fig. **F38G, F38H**). The depth adjustments required to match the gamma radiation log were subsequently applied to all the other logs from the same tool string.

Logging Stratigraphy

The logged section is characterized by subtle variations around very low mean values. For example, total gamma ray counts do not exceed 25 API and are mostly centered at 6 API (Fig. **F39A, F39B, F39C**). The spherically focused resistivity, medium-induction phasor-processed resistivity, and deep-induction phasor-processed resistivity are commonly plotted on a logarithmic scale because the values typically range over a few orders of magnitude. Here, resistivities are between 0.5 and 1.5 Ωm and are plotted on a linear scale (Fig. **F39D**). Highest variabilities are recorded in porosity and density logs (Fig. **F39E, F39F**) and their associated parameters, the capture cross section (Σf) and the photoelectric factor (PEF). When reliable, the sonic log is correlated with density and shows an increase in compressional velocity downhole (Fig. **F39G**).

Based on the homogeneity of the formation, one log unit and four subunits have been defined (Fig. **F39H**). These subunits are differentiated by density, porosity, and resistivity logs.

F39. Downhole log stratigraphy, p. 76.

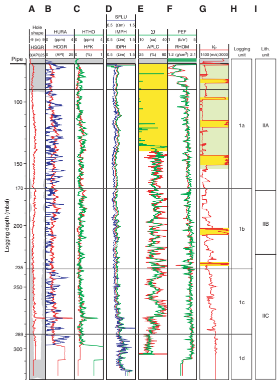

Logging Subunit 1a

Depth: base of pipe (69 mbsf) to 170 mbsf

Logging Subunit 1a is characterized by a downhole increase in density (from 1.8 to 1.9 g/cm^3) concomitant with a decrease in porosity and high-frequency fluctuations in these properties. Resistivity values are low (~0.8 Ωm) (Fig. **F39**). Logging Subunit 1a correlates with lithostratigraphic Subunit IIA, containing lower Oligocene to upper Miocene nannofossil ooze and foraminifer-bearing nannofossil ooze (see **"Subunit IIA,"** p. 7, in "Unit II" in "Description of Lithostratigraphic Units" in "Lithostratigraphy").

Logging Subunit 1b

Depth: 170–235 mbsf

Overall, this subunit is characterized by cyclic fluctuations of intermediate frequency in the porosity log and by high variability in PEF, which correlates with resistivity (Fig. **F39**). The lower boundary of logging Subunit 1b is defined by the minimal value in the gamma ray log and a step in the sonic log. Density fluctuates around a mean value of 1.9 g/cm^3. Logging Subunit 1b correlates mainly with lithostratigraphic Subunit IIB, containing lower to upper Eocene nannofossil ooze and foraminifer-bearing nannofossil ooze, and the upper part (~10 m) of lithostratigraphic Subunit IIC, containing Paleocene to lower Eocene nannofossil ooze and foraminifer-bearing nannofossil ooze (see **"Subunit IIB,"** p. 8, and **"Subunit IIC,"** p. 8, both in "Unit II" in "Description of Lithostratigraphic Units" in "Lithostratigraphy").

Logging Subunit 1c

Depth: 235–289 mbsf

Logging Subunit 1c is characterized by low-frequency cycles in porosity. Four well-defined high-amplitude cycles are clearly visible in this log. Subtle increases downhole in NGR from thorium and potassium and in resistivity mark the upper limit of this subunit. Logging Subunit 1c correlates with the bottom part of lithostratigraphic Subunit IIC, containing Paleocene to lower Eocene nannofossil ooze and foraminifer-bearing nannofossil ooze (see **"Subunit IIC,"** p. 8, in "Unit II" in "Description of Lithostratigraphic Units" in "Lithostratigraphy").

Logging Subunit 1d

Depth: 289 mbsf to the bottom of the hole (321 mbsf)

High-frequency variations in the porosity values characterize logging Subunit 1d. This subunit also shows an increase in the variability of the resistivity values associated with chert layers. The density and velocity continuously increase downhole following the gradient of logging Subunit 1c. Logging Subunit 1d correlates with lithostratigraphic Subunit IIC, containing Paleocene to lower Eocene nannofossil ooze and foraminifer-bearing nannofossil ooze (see **"Subunit IIC,"** p. 8, in "Unit II" in "Description of Lithostratigraphic Units" in "Lithostratigraphy").

Discussion

Comparison between continuous in situ logs and the whole-core MST records (NGR and bulk density) and discrete sample measurements of physical properties (density, porosity, and sonic velocity) provides the basis for depth matching the core-derived mcd scale to the logging depth, thus creating a logging equivalent depth scale—a necessary step to correct for the expansion of the cores and obtain correct sedimentation and mass accumulation rates (see **"Age Model and Mass Accumulation Rates,"** p. 33, in the "Explanatory Notes" chapter). To account for slightly different compression ratios observed for the different subunits of Site 1265, features recognized both in the whole-core NGR data (vs. mcd) and in the equivalent downhole logging data (vs. logging depth) were carefully mapped using 41 tie points picked between 71.45 and 292 mbsf logging depth (Table **T15**; Fig. **F40**). Above (pipe) and below (poor core recovery) this interval, no correlation was possible because data were lacking; a linear extrapolation was used. The extrapolation was based on the mean mapping ratio of 1.15, which is in very good agreement with the core-derived composite depth growth rate (see **"Composite Depth,"** p. 4). The lower parts of logging Subunits 1a and 1b (mean density = 1.9 g/cm^3; almost constant within this interval) are characterized by a lower core expansion rate.

T15. Mcd and equivalent logging depth, p. 103.

F40. Composite section to equivalent logging depth, p. 77.

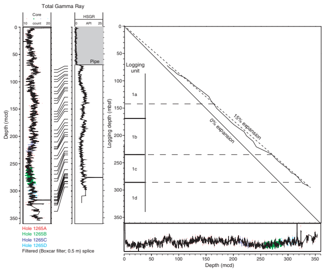

Downhole and core logging data as well as the graphic lithostratigraphy are presented at the equivalent logging depth scale in Figure **F41.** On this scale, with the exception of porosity and sonic velocity, all core and logging data are in good agreement with regard to depth and magnitude. As previously mentioned, the APS malfunctioned in the upper part of the hole. Discrepancy between porosity measured on cores and downhole in the intermediate and lower intervals is without doubt due to a calibration problem, as the neutron log is plotted on a standardized

F41. Core-log integration, p. 78.

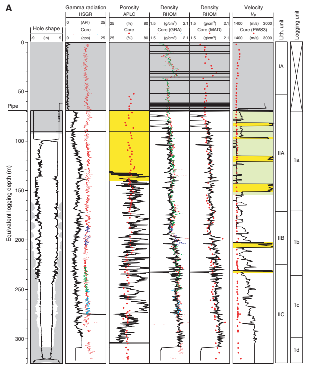

arithmetic scale of neutron (or limestone) porosity units. This value represents real porosity only under standard conditions in clean limestones, and to find the real porosity in other lithologies, the neutron log value must be converted by using tables or empirical calibrations. Even if absolute values are biased, the relative variations in this record are still indicative of lithologic changes in the formation. Discrepancy between *P*-wave velocity measured on the core and downhole is discussed below.

Given the data, only the microresistivity (FMS; vertical resolution ~5 cm) images can theoretically resolve high-frequency cycles seen, for example, in color reflectance data obtained from the cores. In the section logged from 99 to 320 mbsf with the FMS-sonic tool string, the static-normalized microresistivity image confirms the increase in resistivity downhole as seen in the standard resistivity logs. Because of the enlargement in the upper part of the hole, only the intermediate and lower parts of the section can be used for cyclostratigraphic studies. In spite of the washouts in the middle segment (195–255 mbsf) of the hole and the low resistivity values of the formation, numerous submeter (<0.25 m) cycles can be resolved in the dynamically normalized FMS images (Fig. **F42**).

Microresistivity FMS images also allow mapping of chert layers that were poorly recovered in cores. Two resistive intervals associated with cherts at ~287 and 300 mbsf are marked by light color in the static image (Fig. **F43**). Dynamic normalization of the previous image (Fig. **F43B**) and zoom (Fig. **F44**) reveals that these layers are not massive but are associated with gradual and cyclic changes in lithologic composition. Resistive values still are extremely low.

As a preliminary step in the comparison between downhole logging and core properties, Figure **F45** shows the relationship between (1) core density vs. in situ densities, (2) sonic velocity in cores vs. in situ, velocity and density measured (3) on core and (4) in situ, (5) *P*-wave velocity in cores vs. in situ density, and (6) in situ velocity vs. core density; all data are referenced to the equivalent logging depth. For the 90 samples available over the logged interval, all the previous relationships show, as expected, a linear increase in density and velocity with depth. This trend in velocity is corroborated by the sonic log and the checkshot survey (Fig. **F46**).

Assuming that the velocity in seawater is equal to 1525 m/s, the mean velocity of the formation is 1650 m/s, according to the lowermost checkshot. This is a typical value for soft sediment. The P/E boundary recovered in Hole 1265A at 275 m equivalent logging depth is associated with a reflector identified on the seismic line GeoB 01-048 (CDP = 3850) at ~4385 ms TWT (2192.5 ms one-way traveltime) (see **"Introduction,"** p. 1). This is in excellent agreement with the traveltime from checkshots 3 and 4 at 265 and 285 mbsf, respectively (Table **T16**). In the lower part of the borehole (170–320 mbsf), where checkshot measurements are available every 15–25 m, interval velocities are between 1980 and 2300 m/s. These values are consistent with the in situ velocity measured by the DSI in that section, except for a few short intervals where the *P*-wave velocity labeling algorithm in the Schlumberger software had difficulty in identifying the *P*-wave velocity of the formation (Fig. **F47**). The mean interval velocity of the lower 145 m of the borehole (~2100 m/s) from the checkshots exceeds the velocity values measured on cores by >30%. Low velocity values of the core can be explained by their decompression and/or fabric modification before they are measured on board.

F42. FMS images and conductive layers, p. 80.

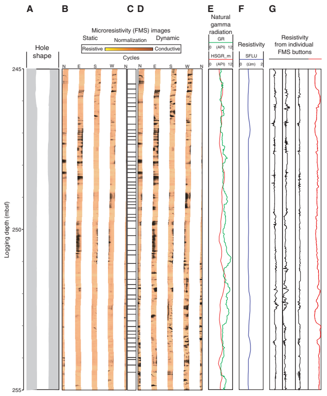

F43. FMS images and chert layers, p. 81.

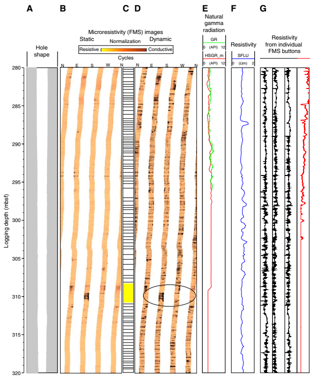

F44. FMS images of diffuse chert layers, p. 82.

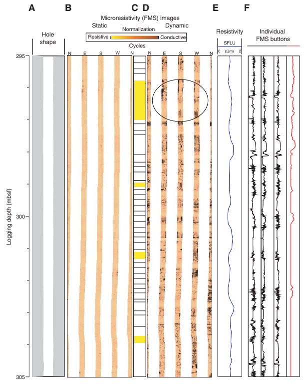

Interval velocities deduced from the checkshot survey result from a clear picking of arrival times of the *P*-wave at the WST-3 geophones, and high confidence can be attributed to these measurements. Indeed, they are in agreement with (1) the seafloor time and (2) the P/E reflector identified on the GeoB 01-048 seismic line. However, having a mean formation velocity equal to ~1650 m/s and a high velocity of ~2100 m/s in the lower part of the formation implies that the upper part (0–170 mbsf) has an interval velocity of <1400 m/s. This value is lower than that for wave propagation in seawater (~1520 m/s) and is therefore not realistic. Such inconsistent results have been reported by other acousticians working in poorly consolidated sediments.

AGE MODEL AND MASS ACCUMULATION RATES

A 359.5-mcd-thick (312.4 mbsf) upper Paleocene (~56 Ma) to Pleistocene pelagic sediment sequence was recovered at Site 1265. A total of 90 biostratigraphic and 24 magnetostratigraphic datums (Table **T17**) were used to construct an age-depth model for this site (Table **T18;** Fig. **F48**). Linear sedimentation rates (LSRs), total mass accumulation rates (MARs), and carbonate MARs were calculated at 1-m.y. intervals (see **"Age Model and Mass Accumulation Rates,"** p. 33, in the "Explanatory Notes" chapter).

Age-Depth Model

The main objective of Site 1265 was to recover a complete and well-resolved upper Paleocene to lower Eocene section, and the site was chosen to yield this critical stratigraphic interval at a relatively shallow burial depth. The sediment section at Site 1265 therefore includes condensed intervals and unconformities, particularly in the middle Eocene (49–40 Ma; 227–221 mcd) and in the upper Miocene (8.9–5.3 Ma; 37–33 mcd). Biostratigraphic and magnetic reversal datums are generally in good agreement, although some planktonic foraminiferal datums are offset by as much as 2 m.y. from the ages provided by nannofossil and paleomagnetic datums. The age-depth model relies primarily on paleomagnetic and nannofossil data.

Linear Sedimentation and Mass Accumulation Rates

LSRs range between <1 and 23 m/m.y., and total MARs range from <0.1 to 3.1 g/cm²/k.y. Total MAR fluctuations essentially represent variations in carbonate MAR. LSRs and carbonate MARs show the highest values (>1.2 g/cm²/k.y.) in the upper Paleocene to lower Eocene. LSRs and MARs in the middle Eocene to Pleistocene record are low to moderate (<1.2 g/cm²/k.y.) and are punctuated by condensed intervals and unconformities.

Noncarbonate MARs are generally low (<0.2 g/cm²/k.y.), and the small fluctuations reported here are probably representative of the analytical uncertainty rather than environmental changes. The moderately high values (0.55 g/cm²/k.y.) in the P/E boundary interval (55 to 54 Ma) are an exception and are related to the carbonate-poor intervals of a few centimeters to several decimeters in thickness (see **"Lithostratigraphy,"** p. 5, and **"Geochemistry,"** p. 22). These short-term carbonate dissolution events are smoothed out in the MAR record as a result of our 1-m.y. sampling of the age-depth model, dictated by the limited res-

F45. Seismic modeling inputs, p. 83.

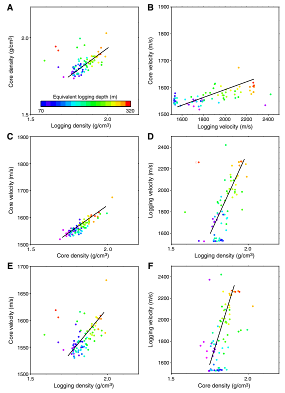

F46. Sonic data, p. 84.

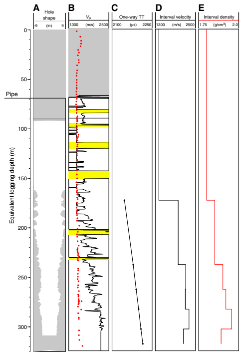

T16. Checkshot survey, p. 104.

F47. Stacked sonic waveforms, p. 85.

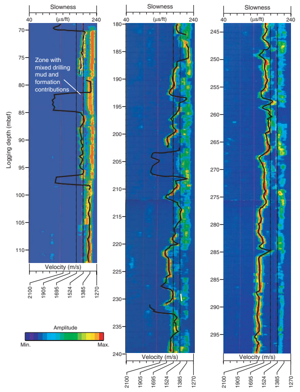

T17. Datum levels, p. 105.

T18. Age-depth model, LSRs, and MARs, p. 107.

olution of the shipboard age-depth control points and density and carbonate data.

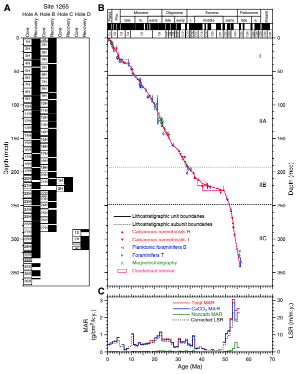

F48. Age-depth model, p. 86.

REFERENCES

Baker, P.A., Gieskes, J.M., and Elderfield, H., 1982. Diagenesis of carbonates in deep-sea sediments—evidence from Sr^{2+}/Ca^{2+} ratios and interstitial dissolved Sr^{2+} data. *J. Sediment. Petrol.,* 52:71–82.

Cande, S.C., and Kent, D.V., 1995. Revised calibration of the geomagnetic polarity timescale for the Late Cretaceous and Cenozoic. *J. Geophys. Res.,* 100:6093–6095.

Clark, M.W., and Wright, R.C., 1984. Paleogene abyssal foraminifers from the Cape and Angola basins, South Atlantic Ocean: DSDP 73. *In* Hsü, K.J., LaBrecque, J.L., et al., *Init. Repts. DSDP,* 73: Washington (U.S. Govt. Printing Office), 459–480.

Deyhle, A., and Kopf, A., 2002. Strong B-enrichment and anomalous boron isotope geochemistry in the Japan forearc. *Mar. Geol.,* 183:1–15.

Gieskes, J.M., 1981. Deep-sea drilling interstitial water studies: implications for chemical alteration of the oceanic crust, layers I and II. *In* Warme, J.E., Douglas, R.G., and Winterer, E.L. (Eds.), *The Deep Sea Drilling Project: A Decade of Progress.* Spec. Publ.—Soc. Econ. Paleontol. Mineral., 32:149–167.

Gieskes, J.M., Johnston, K., and Boehm, M., 1984. Interstitial water studies, Leg 74. *In* Moore, T.C., Rabinowitz, P.D., et al., *Init. Repts. DSDP,* 74: Washington (U.S. Govt. Printing Office), 701–711.

Hayward, B.W., 2002. Late Pliocene to middle Pleistocene extinctions of deep-sea benthic foraminifera ("*Stilostomella* extinction") in the southwest Pacific. *J. Foraminiferal Res.,* 32:274–307.

Hesse, R., 1990. Origin of chert: diagenesis of biogenic siliceous sediments. *In* McIlreath, I.A., and Morrow, D.W. (Eds.), *Diagenesis.* Geosci. Can. Repr. Ser., 4:227–251.

James, R.H., Allen, D.E., and Seyfried, W.E., Jr., 2003. An experimental study of alteration of oceanic crust and terrigenous sediments at moderate temperatures (51 to 350°C): insights as to chemical processes in near-shore ridge-flank hydrothermal systems. *Geochim. Cosmochim. Acta,* 67:681–691.

Lourens, L.J., Hilgen, F.J., Laskar, J., Shackleton, N.J., and Wilson, D., in press. The Neogene period. *In* Gradstein, F.M., Ogg, J., and Smith, A.G. (Eds.), *A Geological Time Scale 2004:* Cambridge (Cambridge Univ. Press).

Moore, T.C., Jr., Rabinowitz, P.D., et al., 1984. *Init. Repts. DSDP,* 74: Washington (U.S. Govt. Printing Office).

Müller-Merz, E., and Oberhänsli, H., 1991. Eocene bathyal and abyssal benthic foraminifera from a South Atlantic transect at 20–30° S. *Palaeogeogr., Palaeoclimatol., Palaeoecol.,* 83:117–171.

Schmiedl, G., Mackensen, A., and Müller, P.J., 1997. Recent benthic foraminifera from the eastern South Atlantic Ocean: dependence on food supply and water masses. *Mar. Micropaleontol.,* 32:249–287.

Smart, C.W., and Murray, J.W., 1994. An early Miocene Atlantic-wide foraminiferal/palaeoceanographic event. *Palaeogeogr., Palaeoclimatol., Palaeoecol.,* 108:139–148.

Smart, C.W., and Ramsay, A.T.S., 1995. Benthic foraminiferal evidence for the existence of an early Miocene oxygen-depleted oceanic water mass? *J. Geol. Soc. (London, UK),* 152:735–738.

Thomas, E., 1986. Changes in composition of Neogene benthic foraminiferal faunas in equatorial Pacific and North Atlantic. *Palaeogeogr., Palaeoclimatol., Palaeoecol.,* 53:47–61.

Thomas, E., and Shackleton, N., 1996. The Palaeocene–Eocene benthic foraminiferal extinction and stable isotope anomalies. *In* Knox, R.W.O'B., Corfield, R.M., and Dunay, R.E. (Eds.), *Correlation of the Early Paleogene in Northwest Europe.* Geol. Soc. Spec. Publ., 101:401–441.

Tjalsma, R.C., 1983. Eocene to Miocene benthic foraminifers from DSDP Site 516, Rio Grande Rise, South Atlantic. *In* Barker, P.F., Carlson, R.L., Johnson, D.A., et al., *Init. Repts. DSDP,* 72: Washington (U.S. Govt. Printing Office), 731–756.

Figure F1. *Meteor* Cruise M49/1 track chart showing the locations of Leg 208 sites, including Site1265 (proposed Site WALV-9B) and alternate Site WALV-9A along seismic line GeoB 01-048.

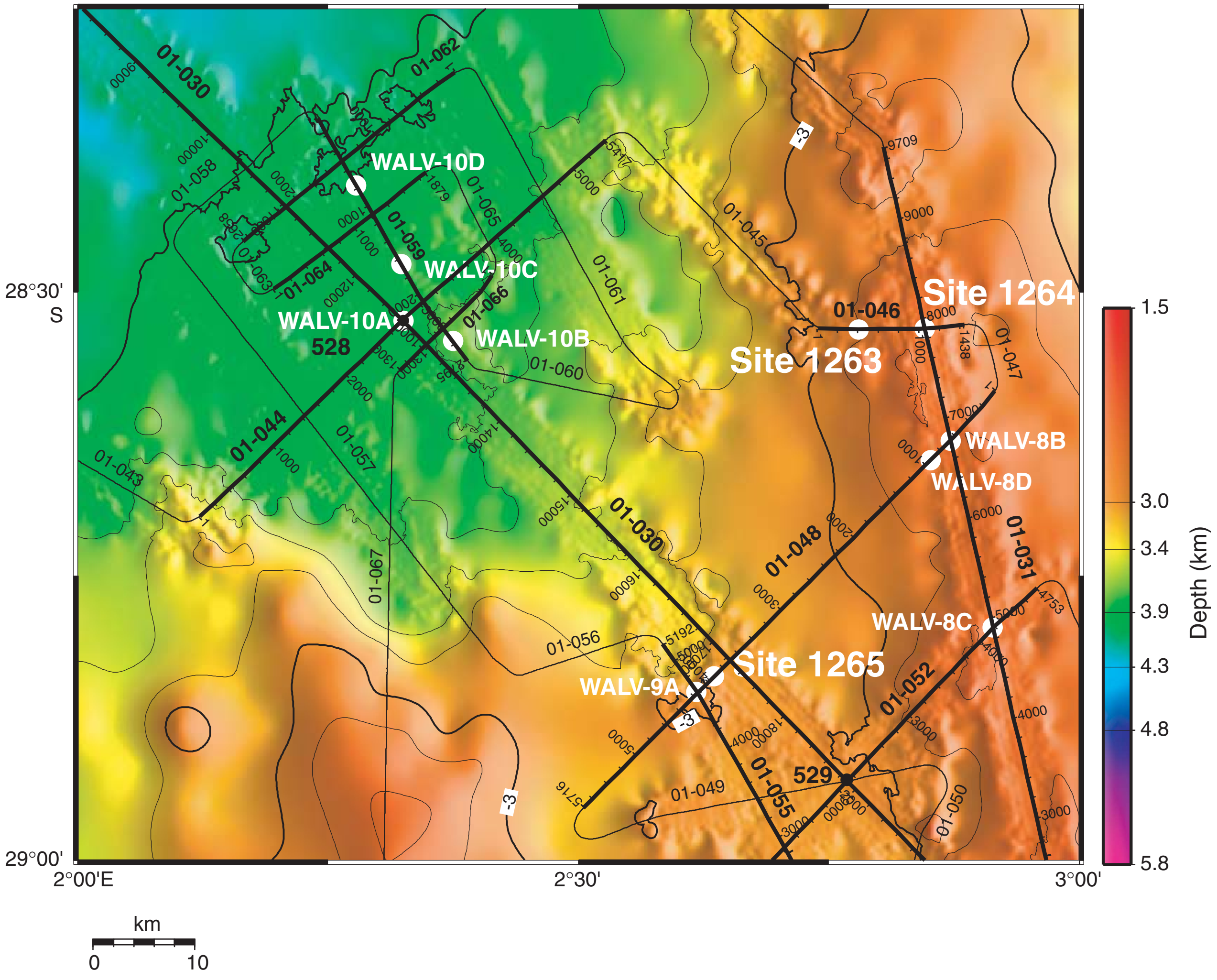

Figure F2. Site 1265 and proposed Site WALV-9A on seismic line GeoB 01-048 (Part 1) with the location of crossing lines GeoB 01-030 and GeoB 01-055. Reflector $R_{O/M}$ is near the Oligocene/Miocene (O/M) boundary, and $R_{P/E}$ and $R_{K/P}$ represent the Paleocene/Eocene (P/E) and Cretaceous/Paleogene (K/P) boundaries, respectively. CDP = common depth point. V.E. = vertical exaggeration. GI = generated injection.

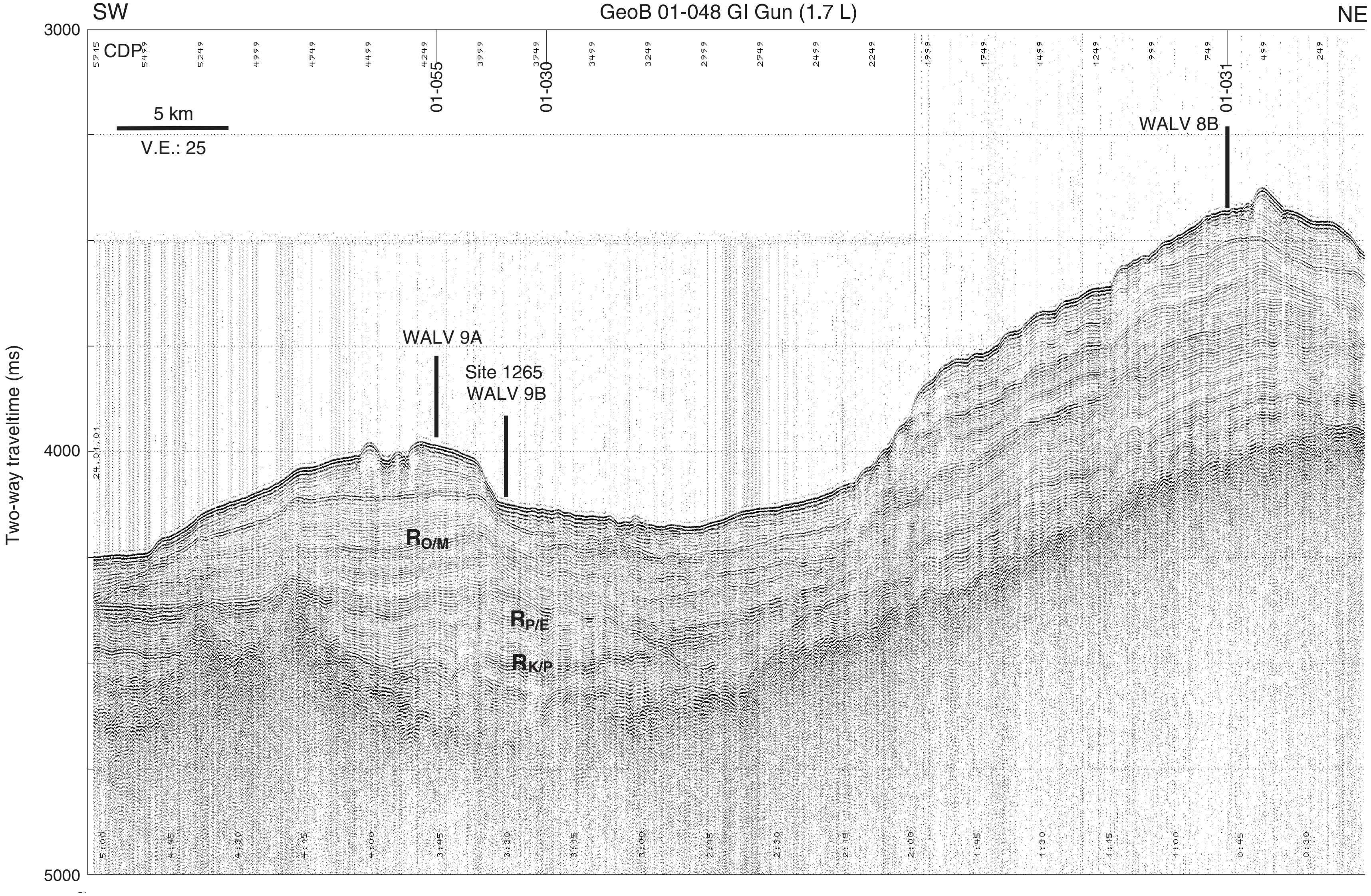

Figure F3. Line GeoB 01-046 and Site 1265 plotted with prominent reflectors. $R_{O/M}$ is just below the Oligocene/Miocene (O/M) boundary at ~112 mbsf. The Paleocene/Eocene boundary reflector ($R_{P/E}$) is estimated to be at 270 mbsf, and the Cretaceous/Paleogene boundary reflector ($R_{K/P}$) is estimated to be at 330 mbsf. CDP = common depth point. V.E. = vertical exaggeration.

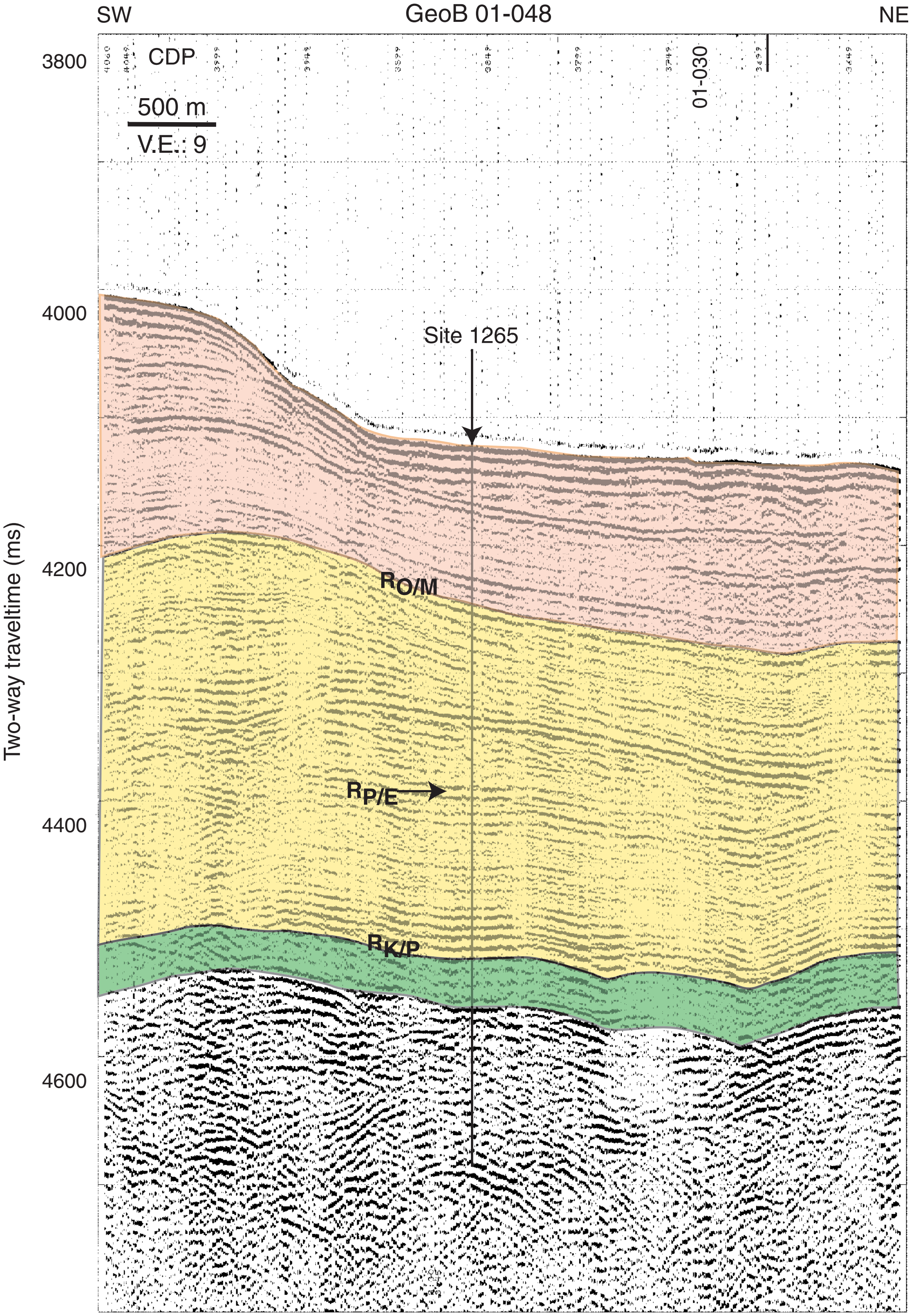

Figure F4. Magnetic susceptibility data from 0 to 350 mcd of Site 1265. Data from Holes 1265A and 1265B are offset from the spliced record by 10 and 100 times their values, respectively. Magnetic susceptibility values less than –1 instrument unit were cut off at –1, and all values lower than 2 were multiplied by 0.5 and incremented by 1. Numbers near the tops of the individual core records refer to the core numbers. * = data from the top of the core is missing or removed because of coring disturbance.

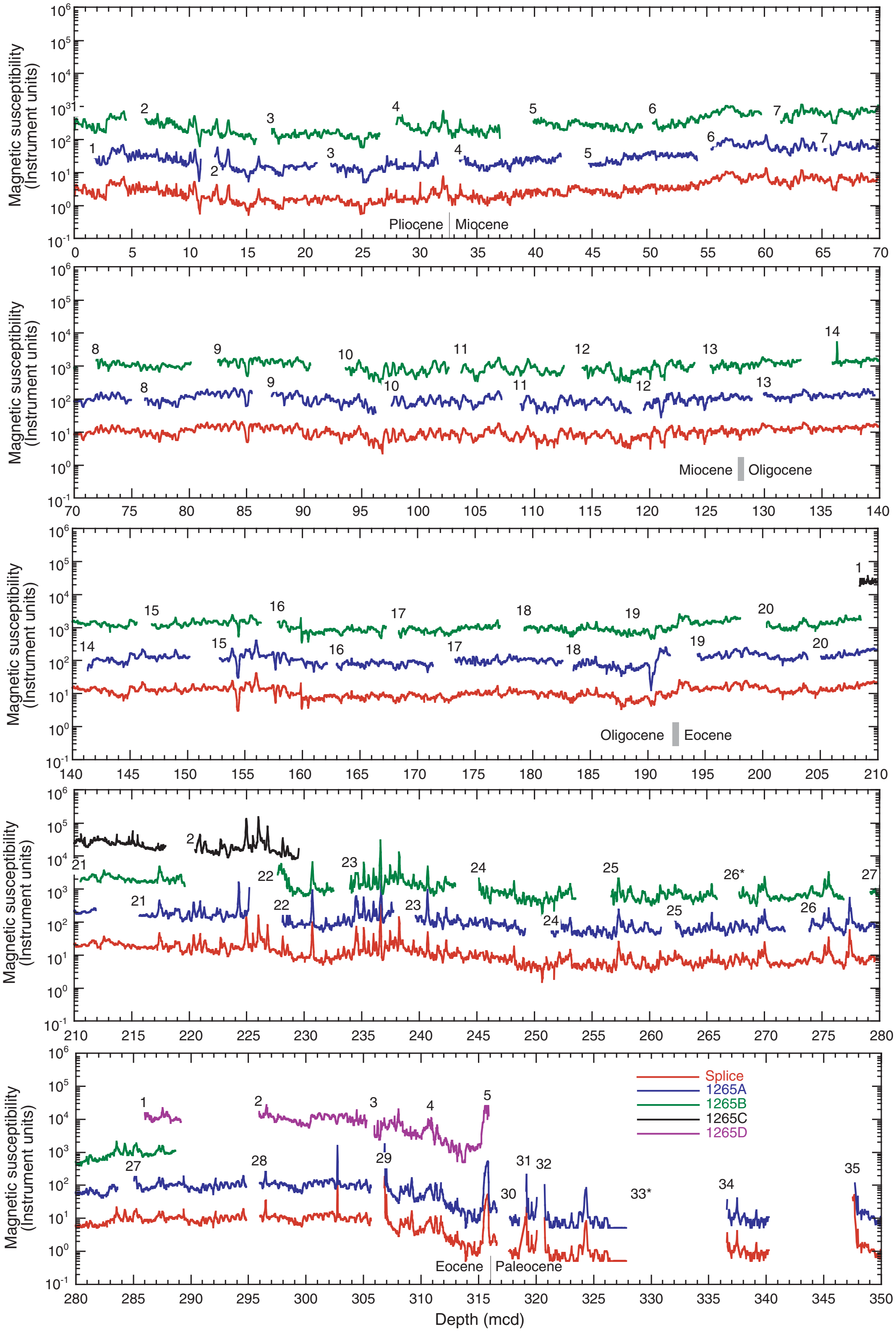

Figure F5. Orange (600 nm) to blue (450 nm) ratio from 0 to 350 mcd of Site 1265. Data from Holes 1265A and 1265B are offset from spliced record by 0.3 and 0.6, respectively. Numbers near the tops of the individual core records refer to the core numbers. * = data from the top of the core is missing or removed because of coring disturbance.

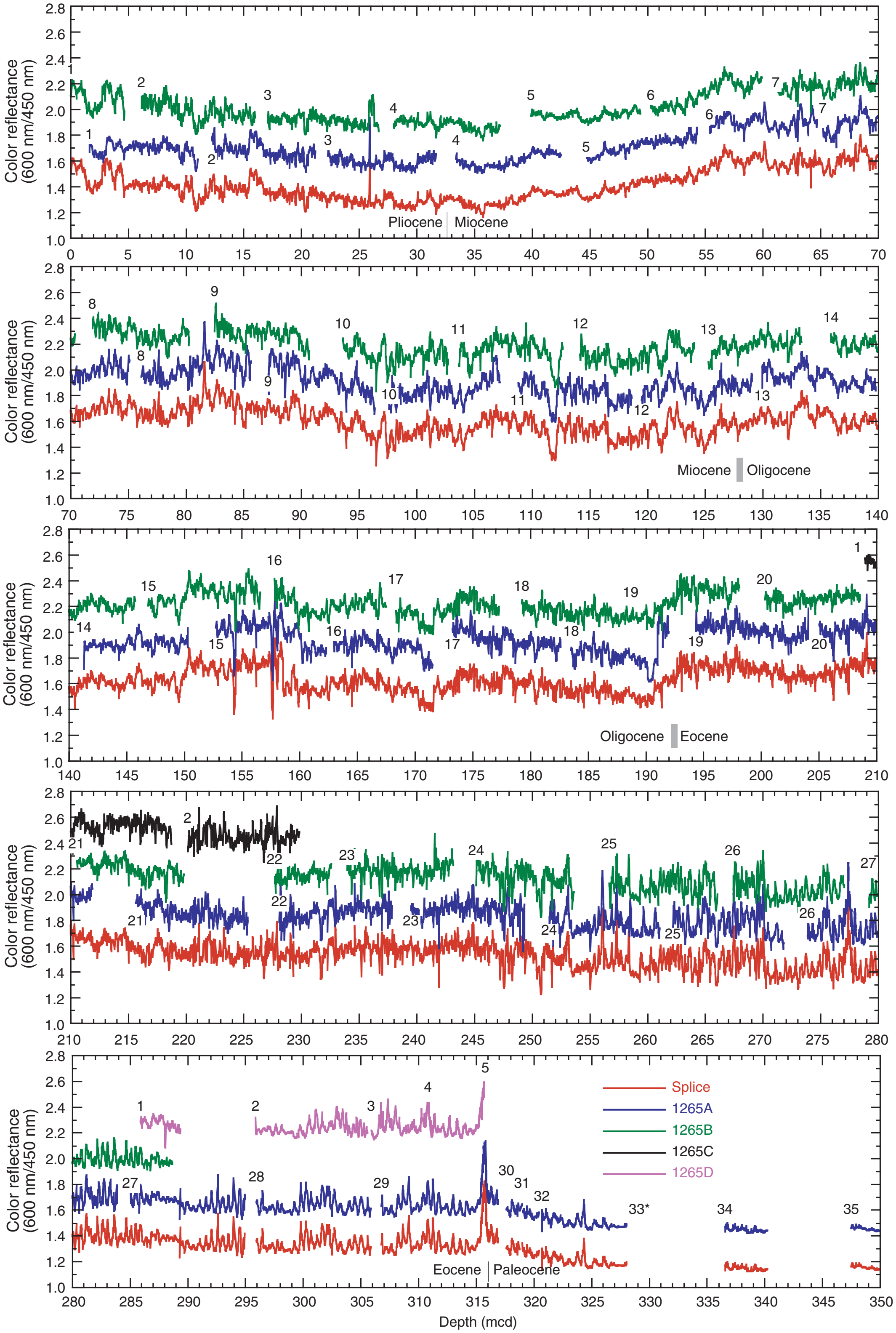

Figure F6. Mcd growth rates for Holes 1265A and 1265B.

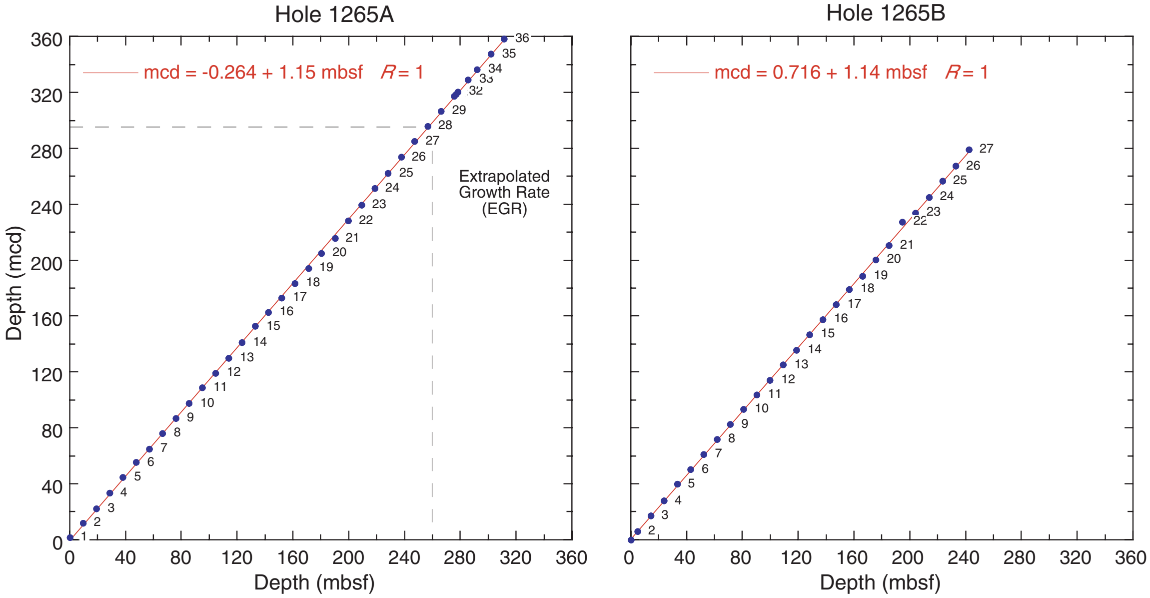

Figure F7. Site 1265 lithostratigraphic composite illustrating stratigraphic variation in parameters used to define lithostratigraphic units, including magnetic susceptibility (MS) (Site 1265 splice; 21-point moving average), sediment lightness (L*) (Site 1265 splice; 21-point moving average), and smear slide foraminifer percentage (open triangles = Hole 1265A, solid triangles = Hole 1265B; solid line is a combined 3-point moving average). Occurrence of turbidite (T), volcanic ash (A), chert (C), and chalky layers (Ch) are also shown. See **"Biostratigraphy,"** p. 10, for derivation of ages.

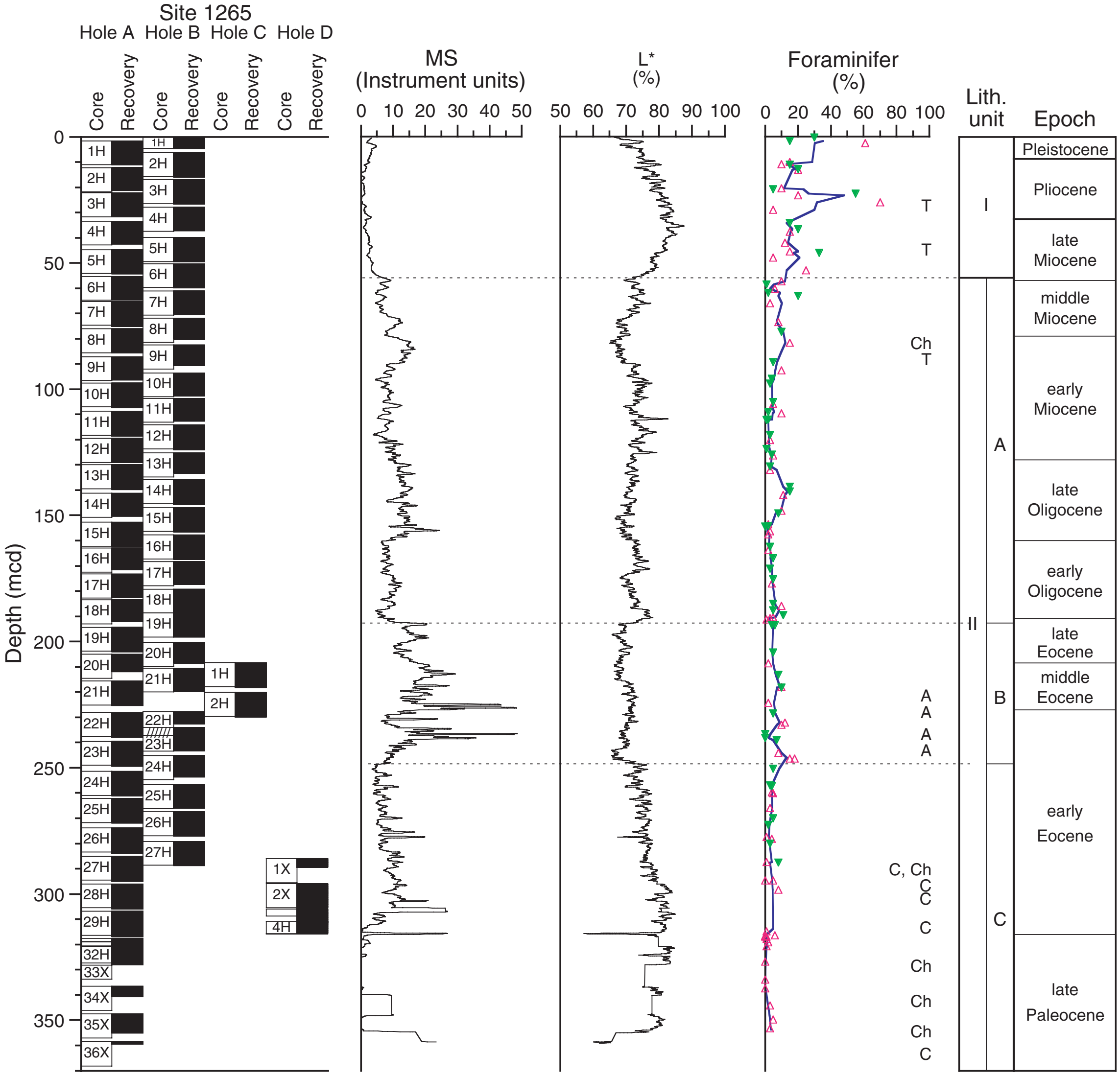

Figure F8. Site 1265 lithostratigraphic composite illustrating stratigraphic variation in whole-core multisensor track measurements of magnetic susceptibility (MS), natural gamma radiation (NGR), and gamma ray attenuation (GRA) bulk density. GRA data from Hole 1265D are smoothed with a 10-point moving average; all other data are from the splice and are smoothed with a 5-point moving average.

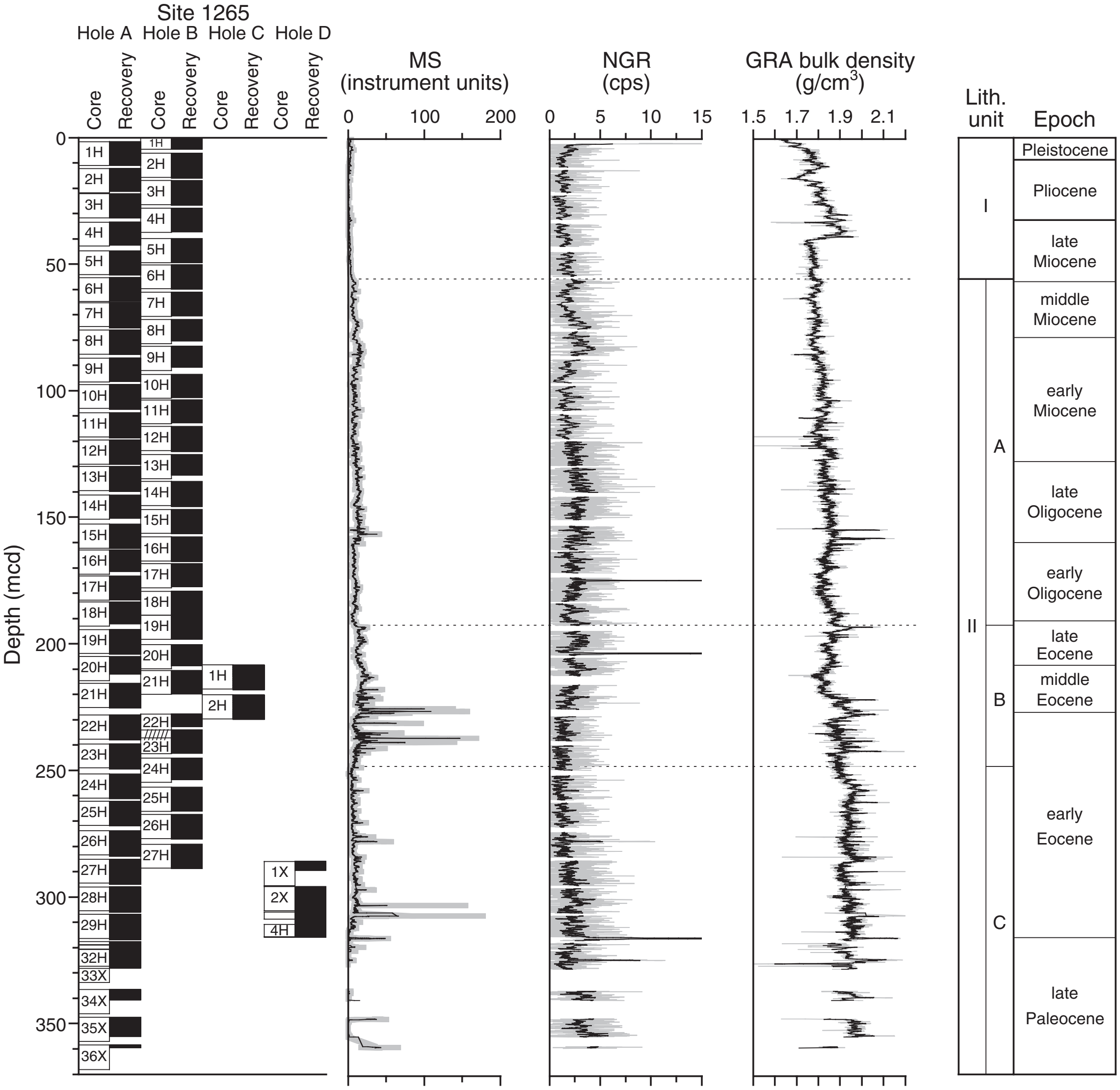

Figure F9. Site 1265 lithostratigraphic composite illustrating stratigraphic variation in sediment lightness (L*), carbonate content, and chromaticity (a* and b*). All data except carbonate content are smoothed with a 5-point moving average.

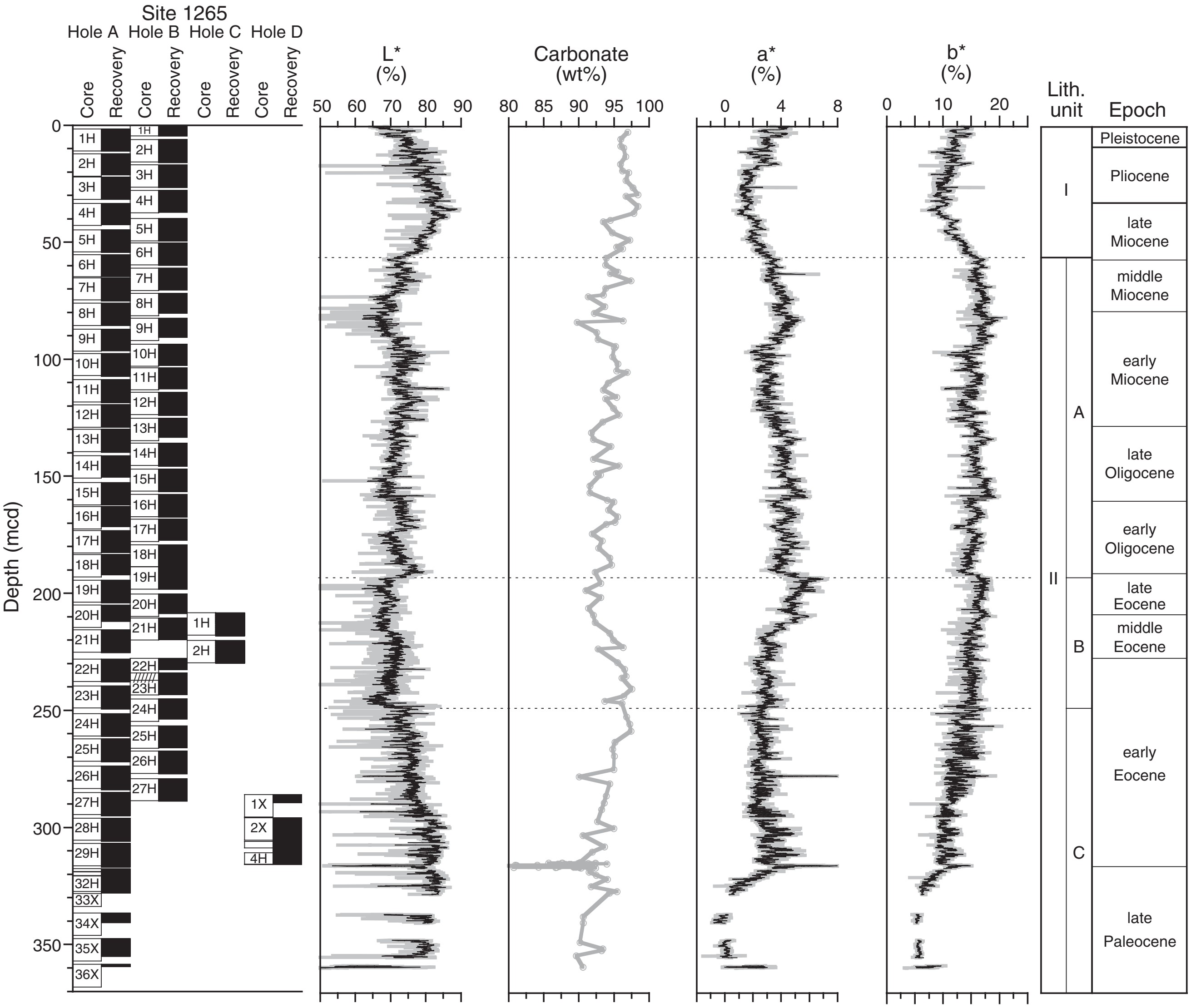

Figure F10. Smear slide–based variation in the percentage of nannofossil, foraminifer, and clay abundances for dominant and minor lithologies at Site 1265 (single points) and smoothed with a 3-point moving average (solid lines).

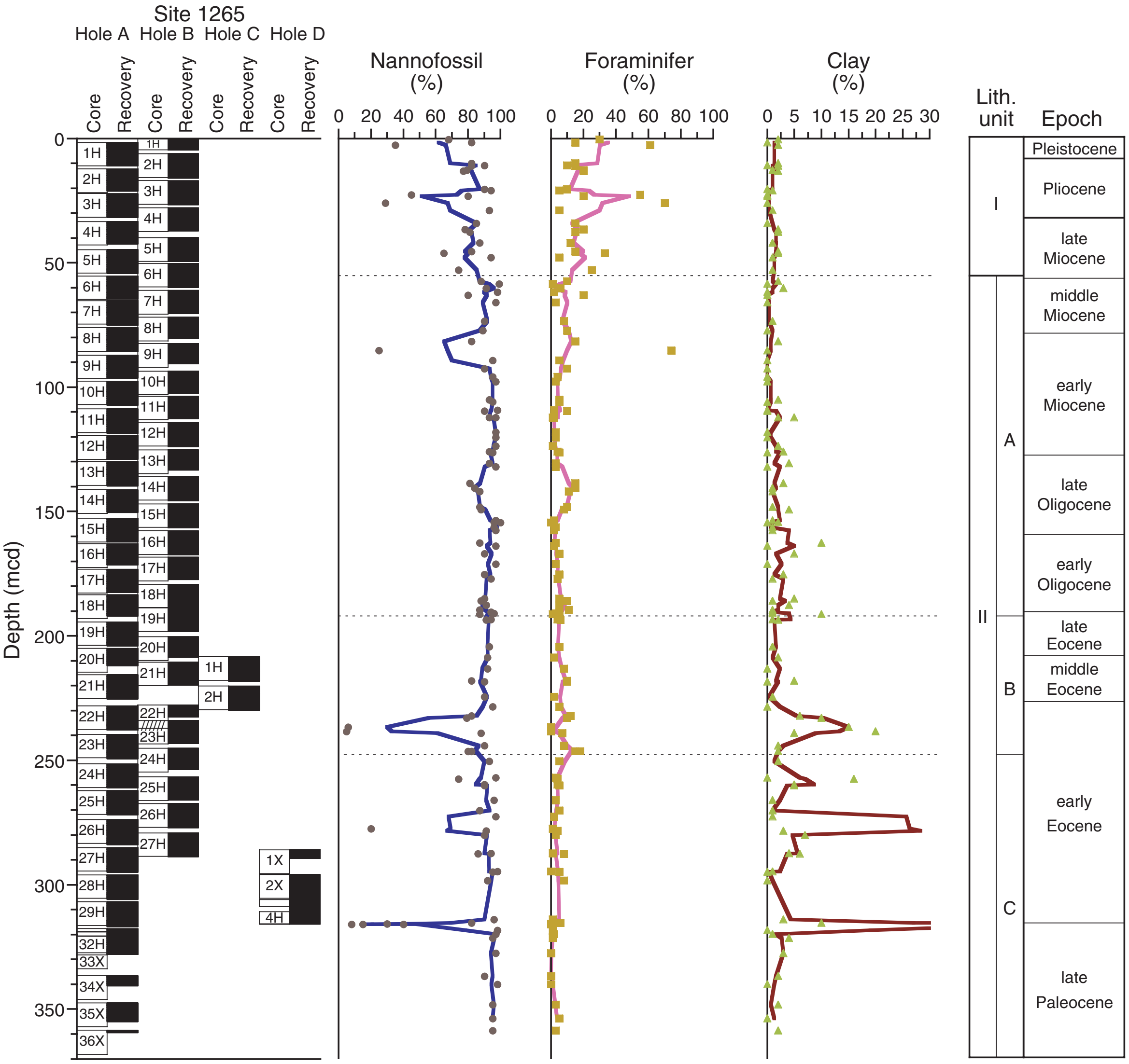

Figure F11. Site 1265 lithostratigraphic composite illustrating stratigraphic variation in grain density (GD), bulk density (BD; MAD method), porosity, and *P*-wave velocity sensor (PWS3) measurements.

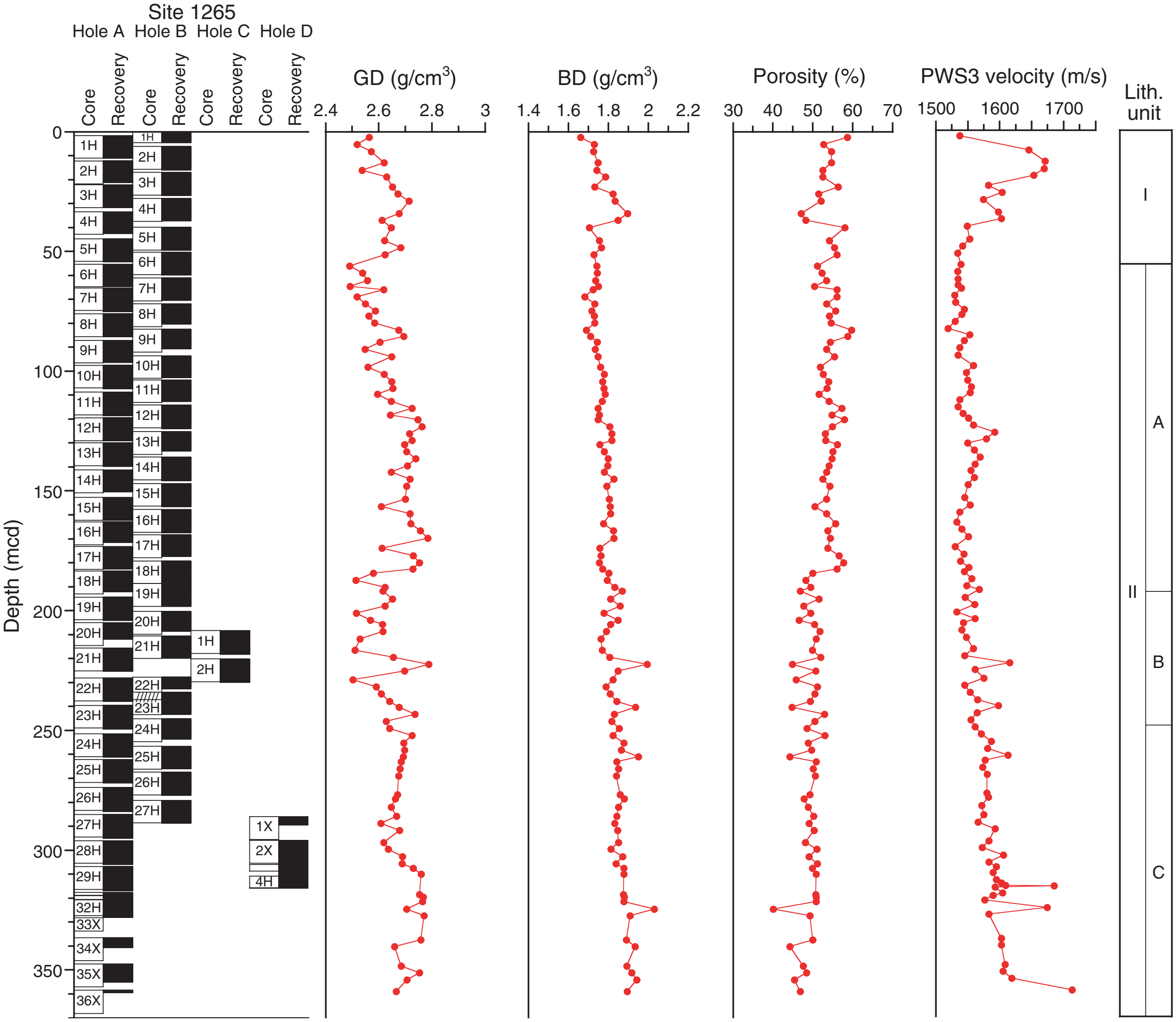

Figure F12. **A, B.** Comparison between bulk density measured by gamma ray attenuation (GRA) and the moisture and density (MAD) methods. **C.** Correlation of grain density (GD) vs. bulk density (BD; MAD method). **D.** Correlation of porosity vs. BD (MAD method). **E.** Correlation of *P*-wave velocity sensor (PWS3) and BD (MAD method) measurements.

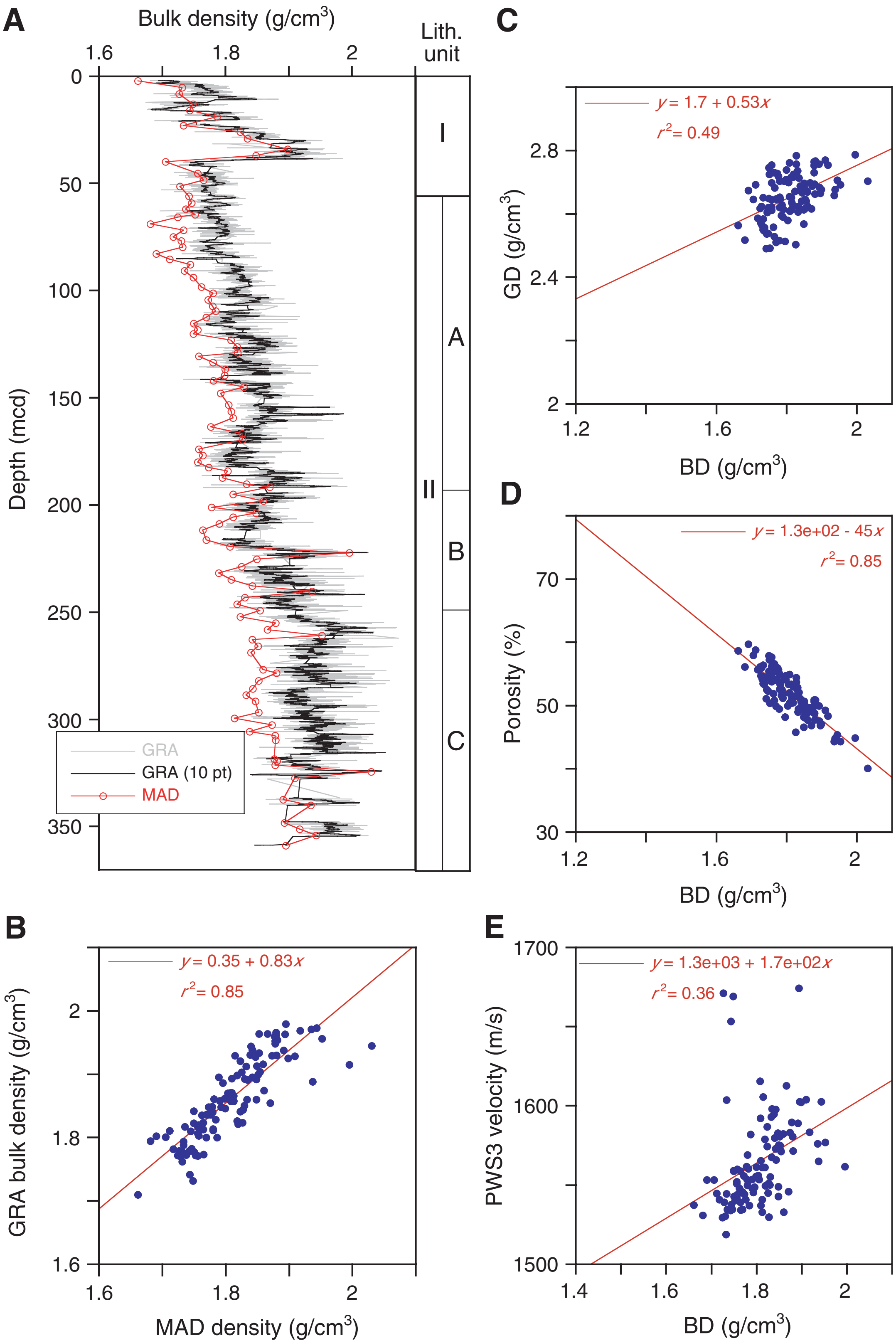

Figure F13. XRD diffractogram of a bleb containing opaque minerals from 294.5 mcd (Sample 208-1265A-27H-7, 47 cm; 256.47 mbsf) illustrating predominance of calcite and presence of lithiophorite ($[Al,Li]MnO_2[OH]_2$), a manganese oxide.

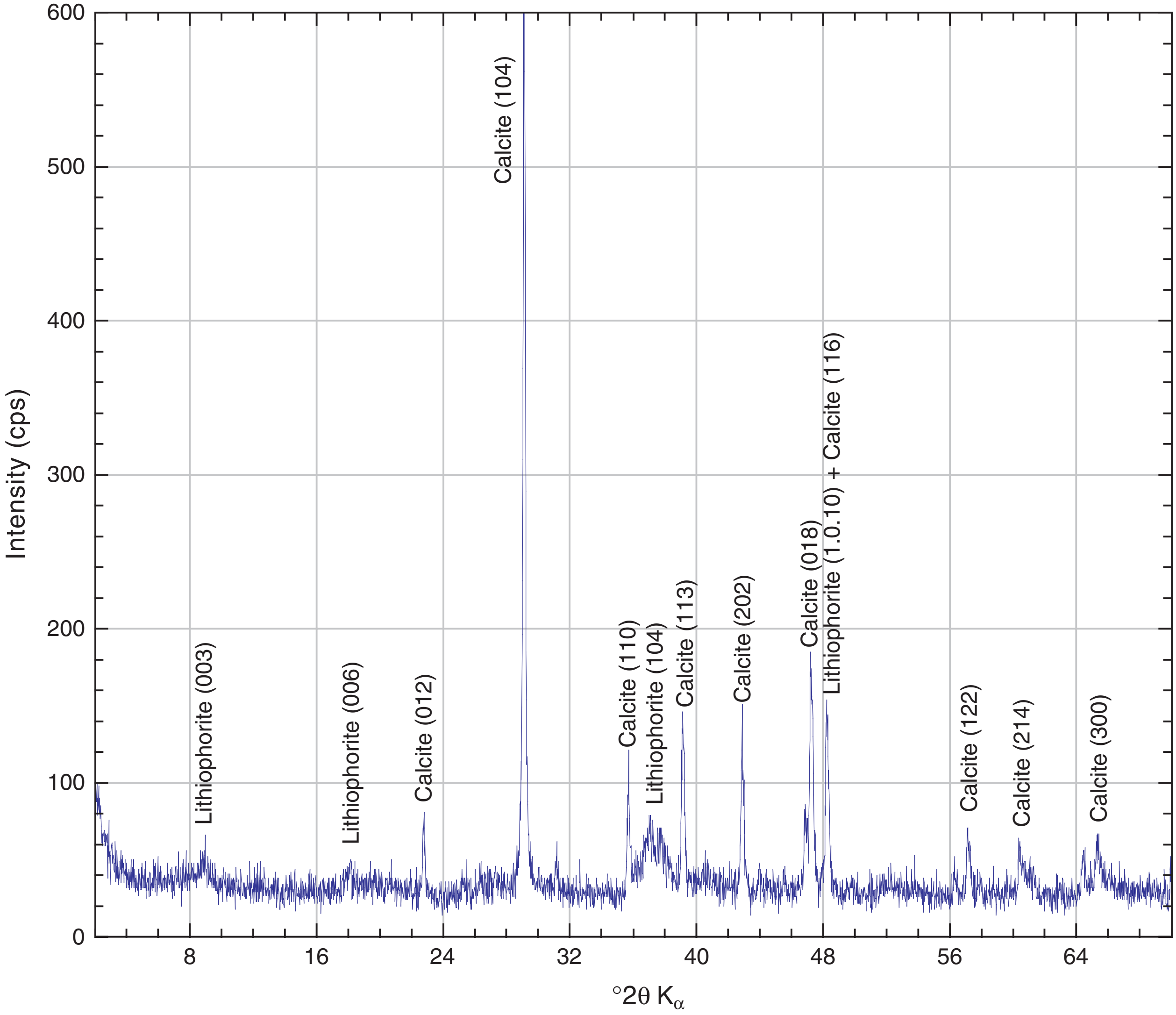

Figure F14. Close-up photograph of sharp contacts of nannofossil-bearing foraminifer ooze enclosing nannofossil ooze in Unit I interpreted as a turbidite or gravity flow deposit (~41.5 mcd; interval 208-1265A-4H-6, 64–79 cm).

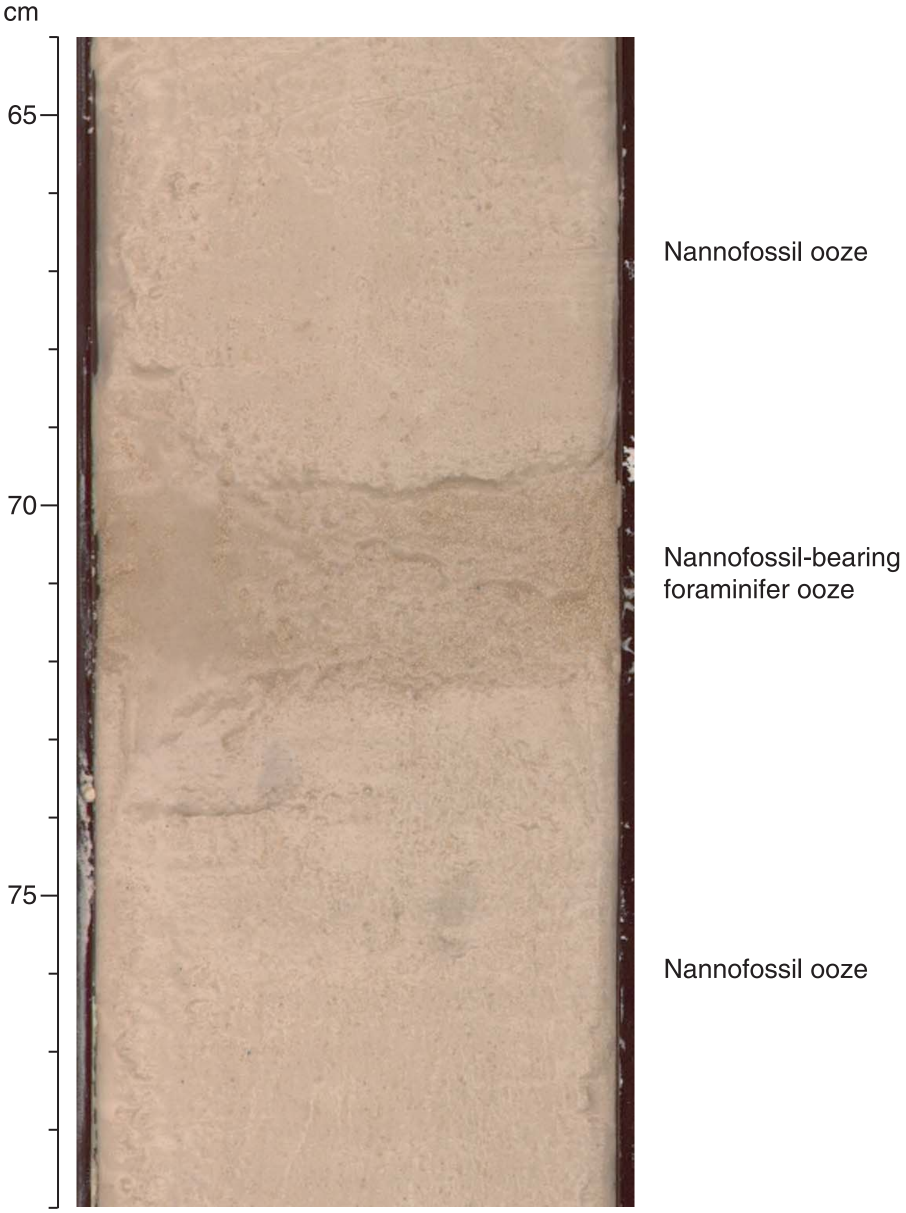

Figure F15. Sediment lightness (L*), magnetic susceptibility, and composite digital image of Core 208-1265A-3H highlighting oscillatory patterns within Unit I.

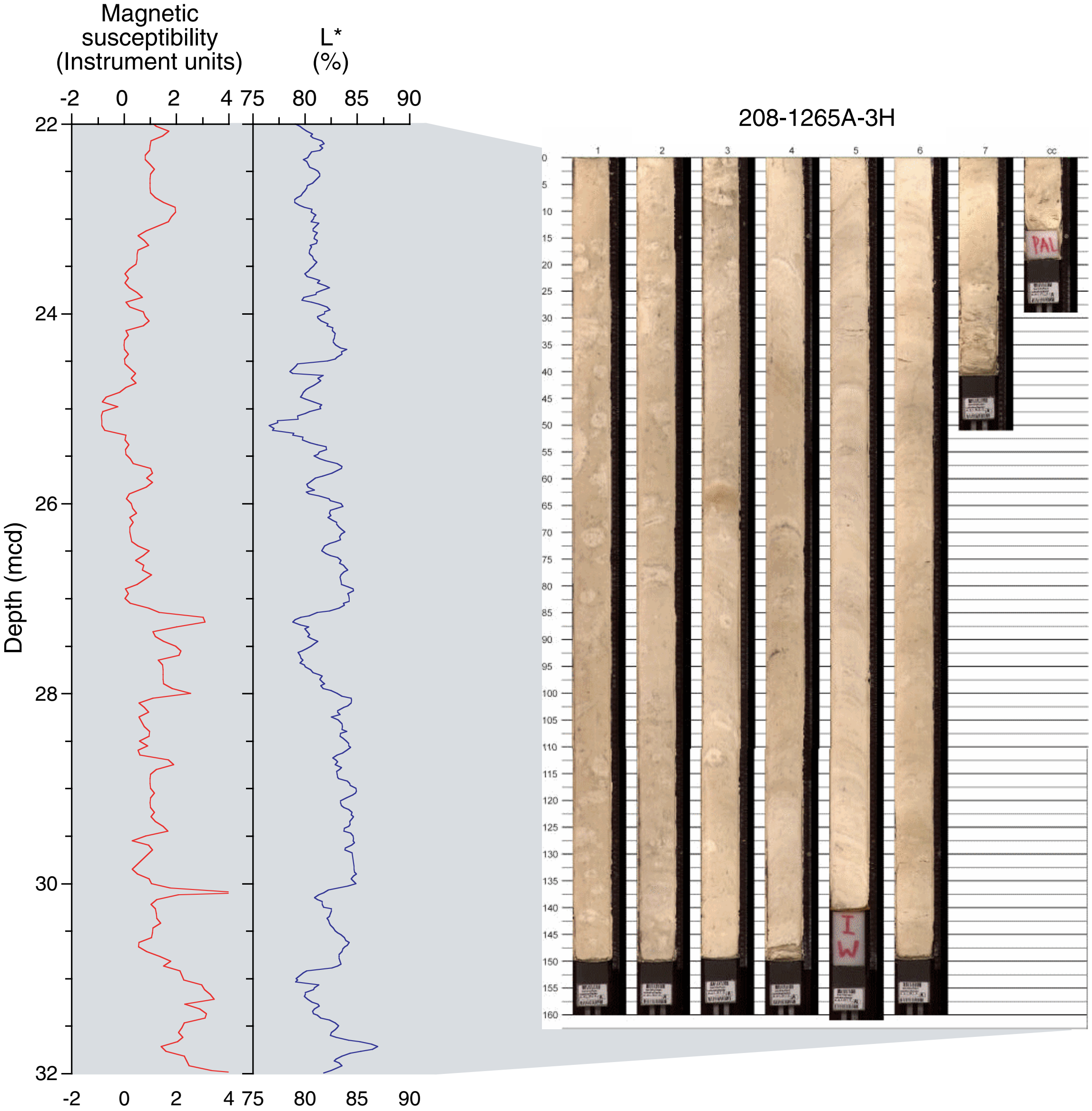

Figure F16. Typical cycles in magnetic susceptibility (red) and sediment lightness (L* [blue]) in (**A**) Subunit IIA, (**B**) Subunit IIB, and (**C**) Subunit IIC. Magnetic susceptibility record is unsmoothed; L* record is smoothed with a 5-point moving average.

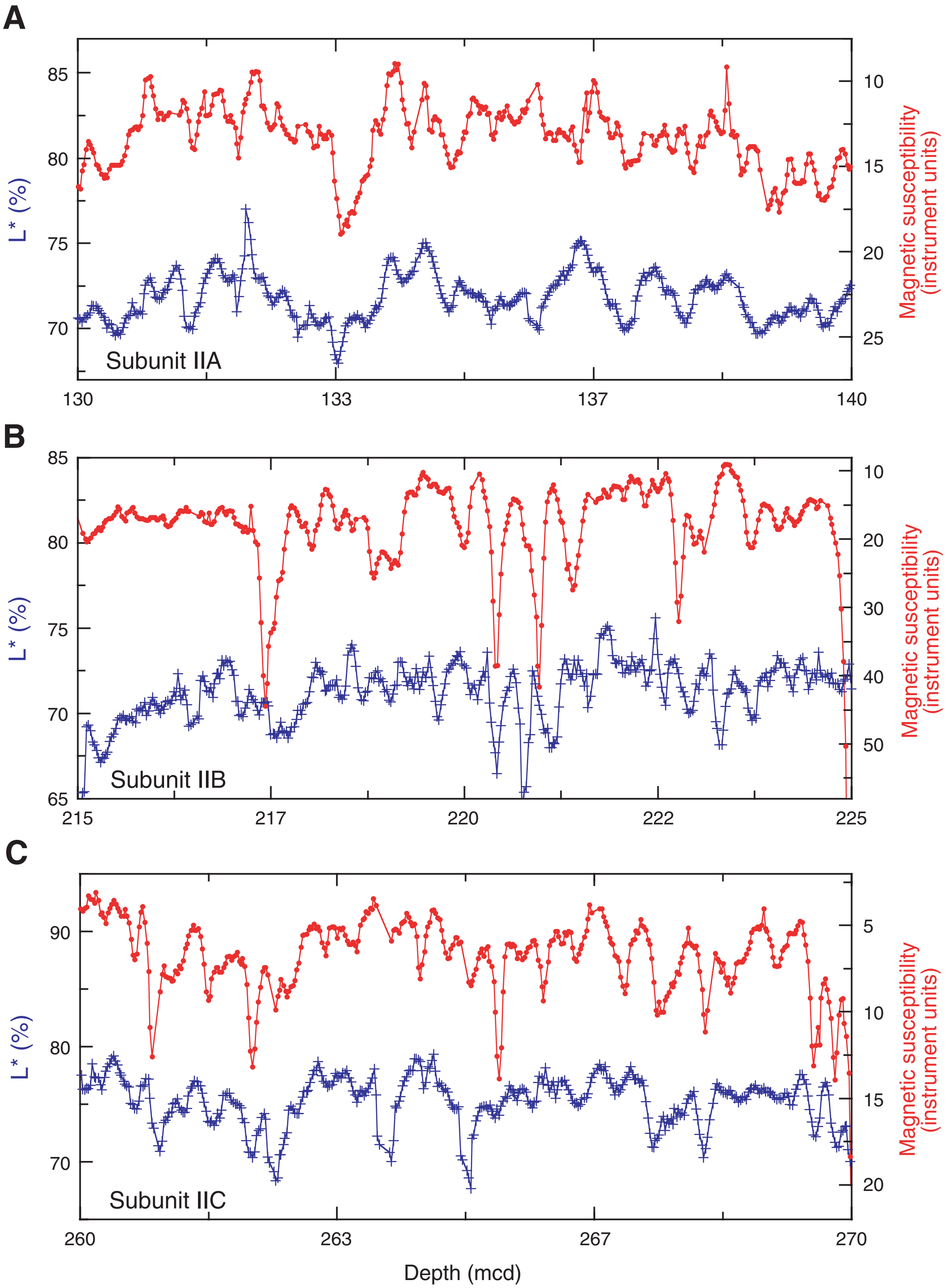

Figure F17. Composite digital image, red-green-blue (RGB) color variation, sediment lightness (L*), and magnetic susceptibility across the Eocene–Oligocene transition interval from ~189 to ~196 mcd (Sections 208-1265B-19H-1, 0 cm, to 19H-5, 140 cm; 166.21–163.60 mbsf). The lithostratigraphic boundary between Subunits IIA/IIB (~192.7 mcd; dotted line) is approximately near the Eocene/Oligocene boundary and is reflected by a step increase in magnetic susceptibility and step decrease in RGB color variation and L*.

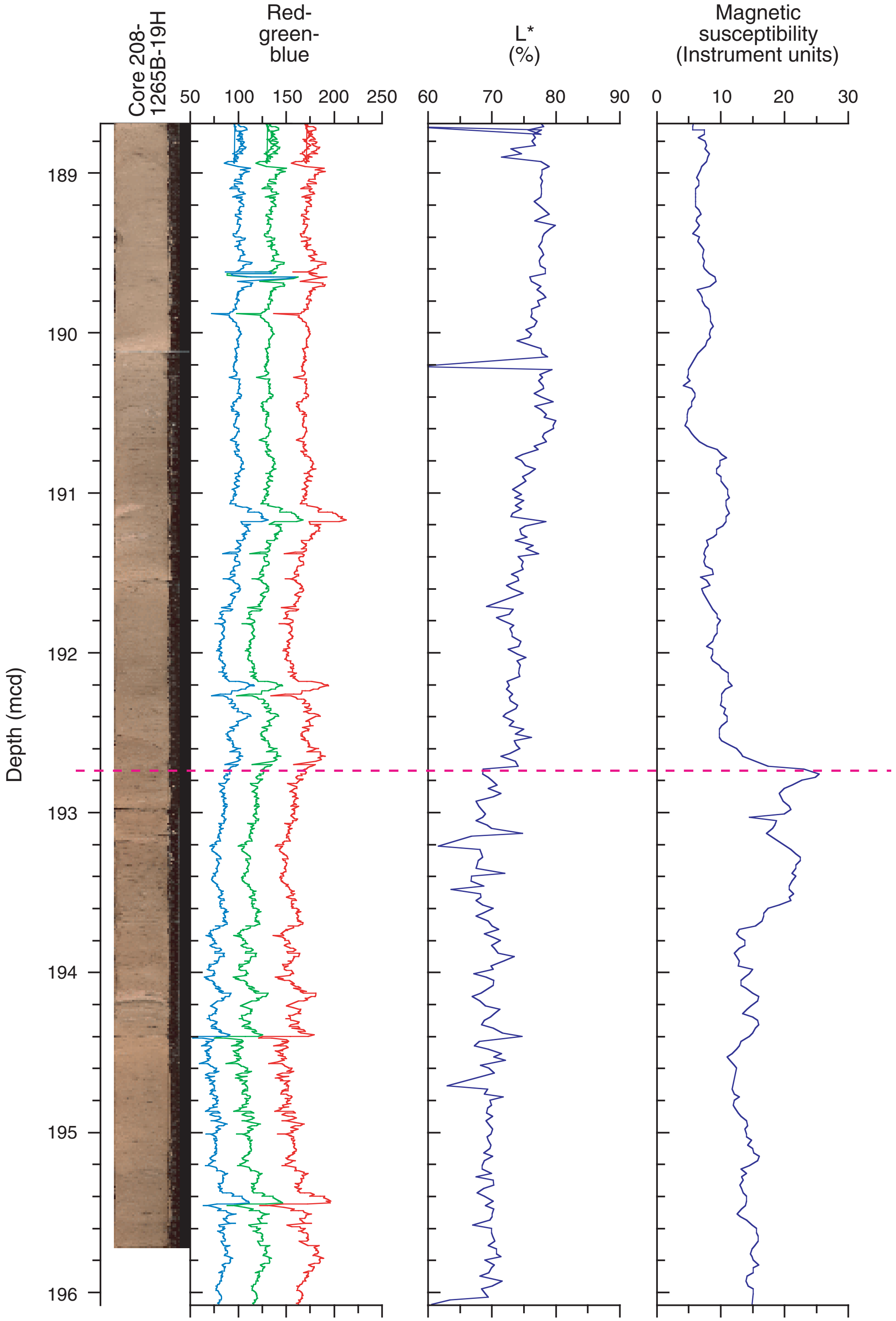

Figure F18. Untreated, heated, and glycolated clay-separation XRD diffractograms of a Subunit IIB sample taken at 191.60 mcd (Sample 208-1265A-18H-7, 62 cm; 169.60 mbsf) illustrating a clay mineral assemblage comprising kaolinite, illite, and smectite.

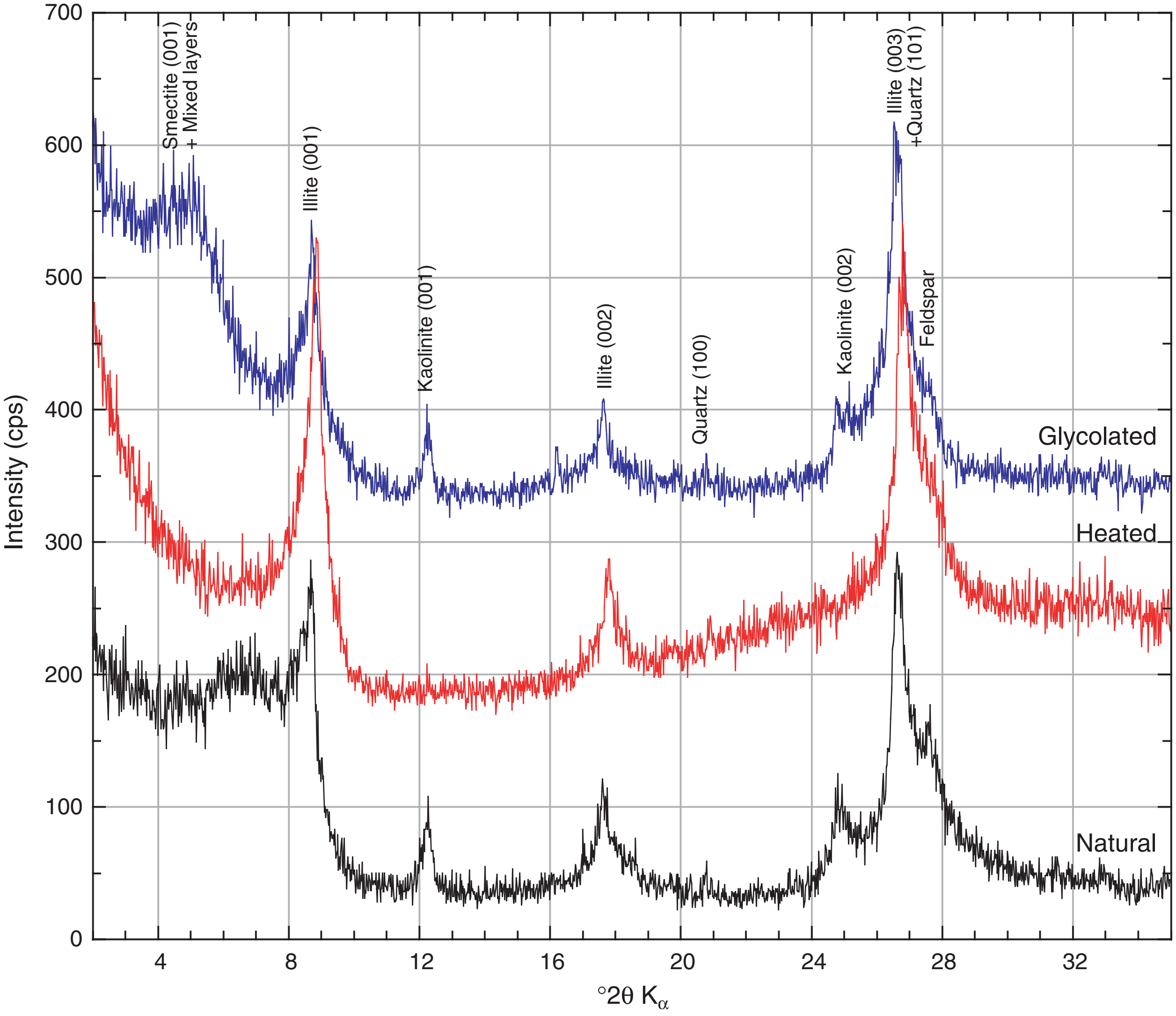

Figure F19. Three volcanic ash intervals in Subunit IIB from 225 to 227 mcd (intervals 208-1265C-2H-4, 35–150 cm, to 2H-5, 0–80 cm; 199.30–201.30 mbsf). Darker brown centimeter-scale layers are characterized by higher magnetic susceptibility and lower L*.

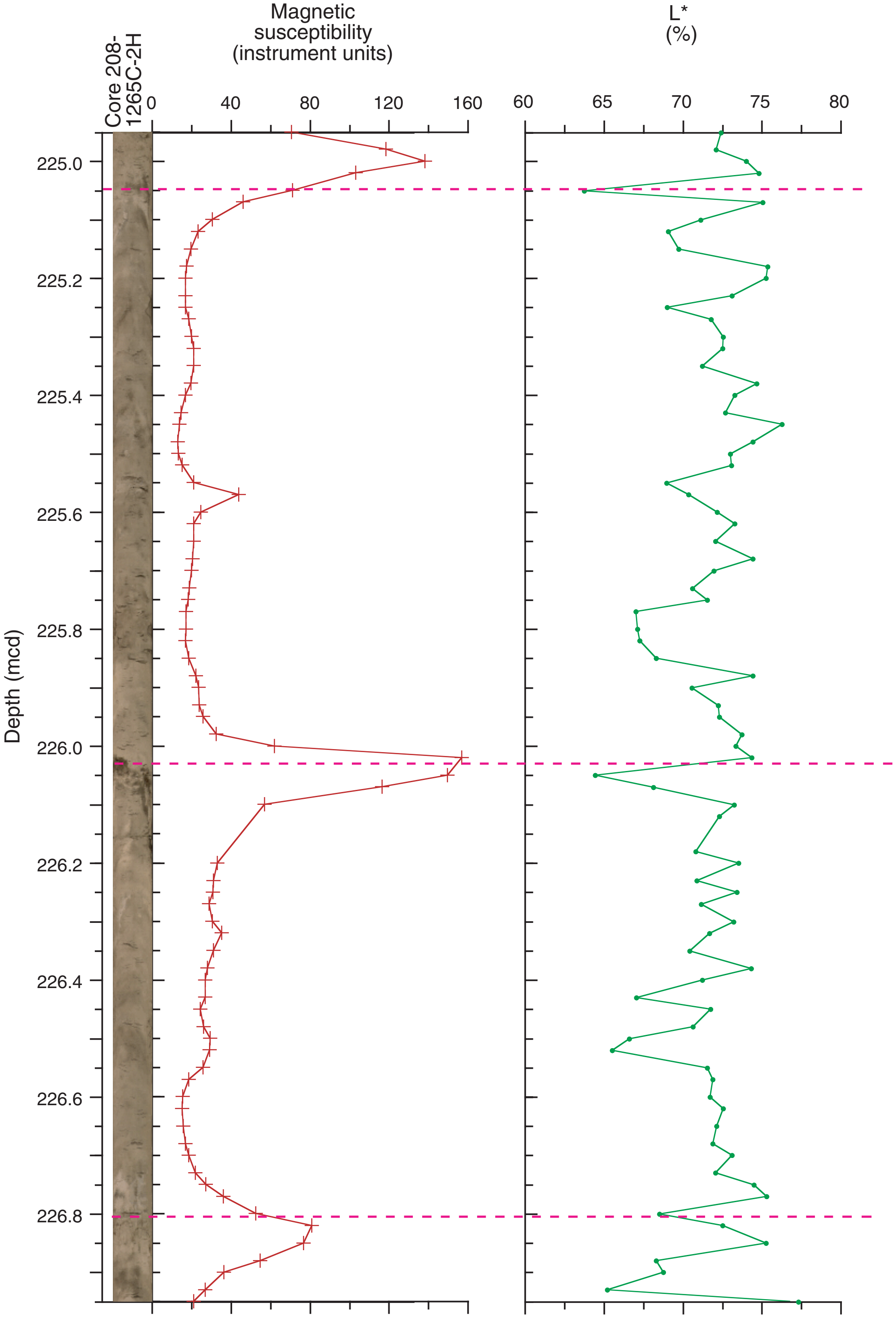

Figure F20. Site 1265 lithostratigraphic composite illustrating chromaticity (a*), manganese and iron concentrations in the interstitial waters, and grain density.

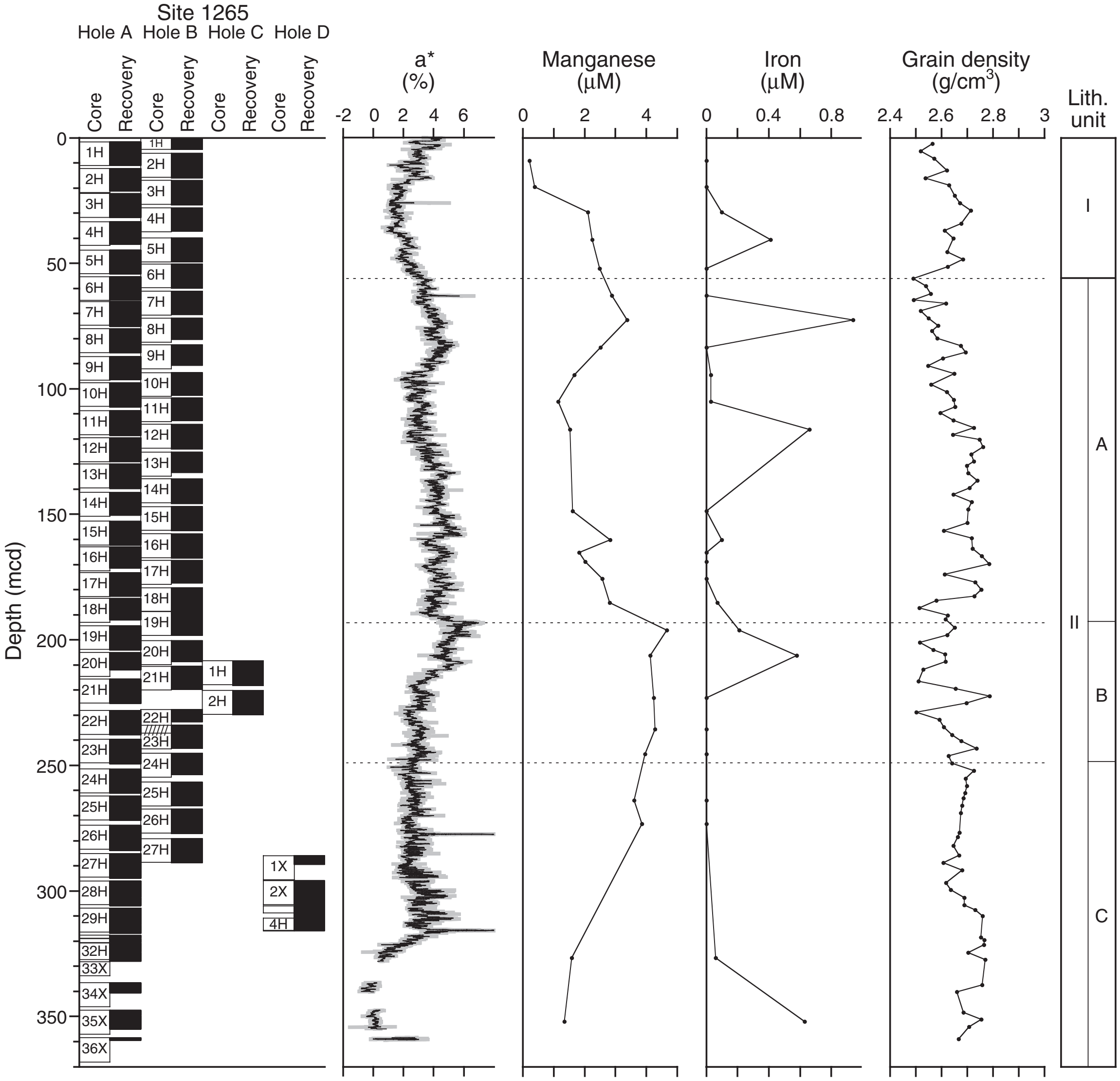

Figure F21. XRD diffractogram and digital image of a "proto-chert" nodule from ~292.7 mcd (Sample 208-1265A-27H-6, 12 cm; 254.62 mbsf). The presence of opal-CT suggests the onset of silica diagenesis within the sequence.

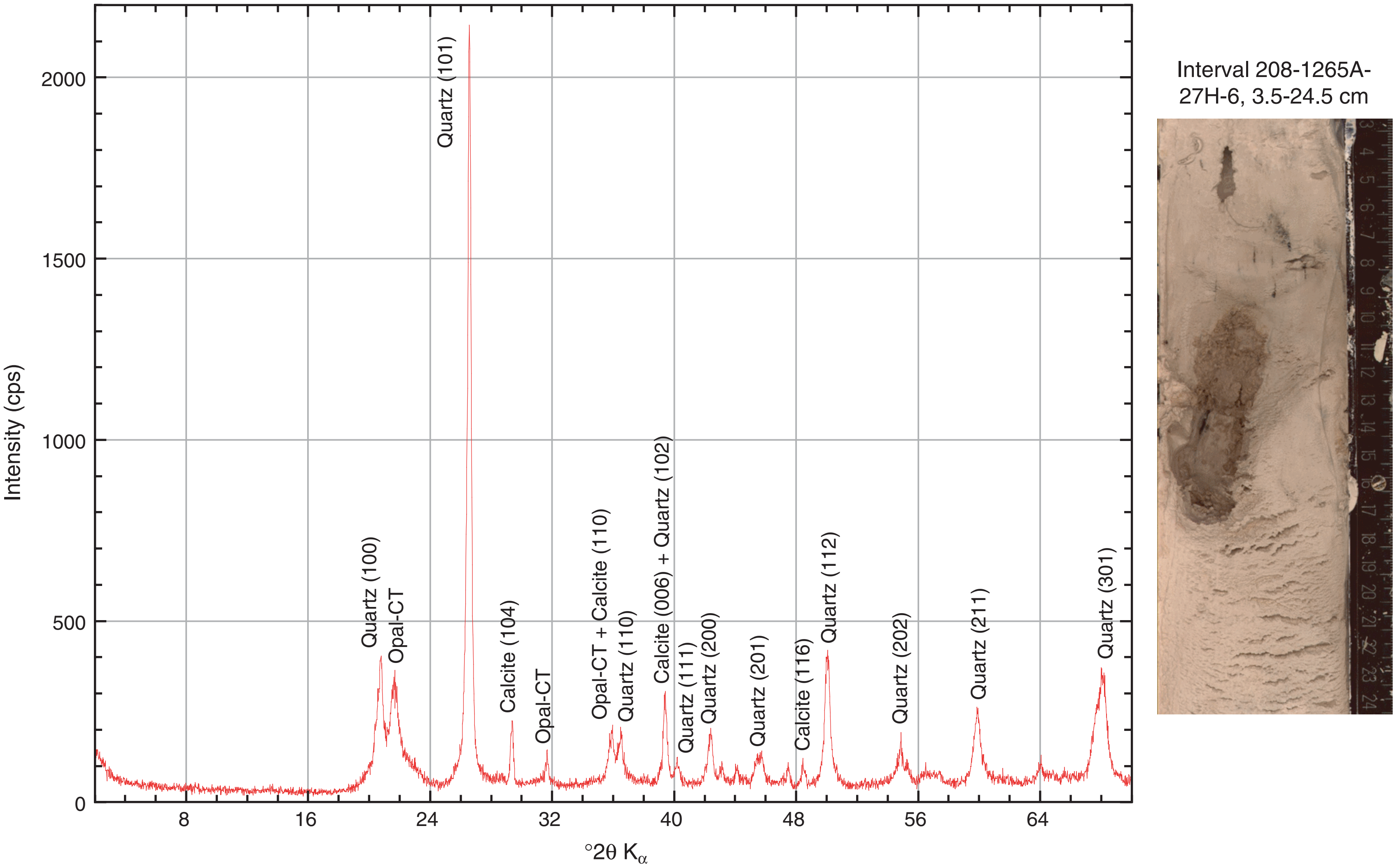

Figure F22. Digital image, magnetic susceptibility (black), and chromaticity (a*; red) of the Chron C24n clay-enriched horizon in Subunit IIC (Section 208-1265A-26H-3; 276.9–278.3 mcd).

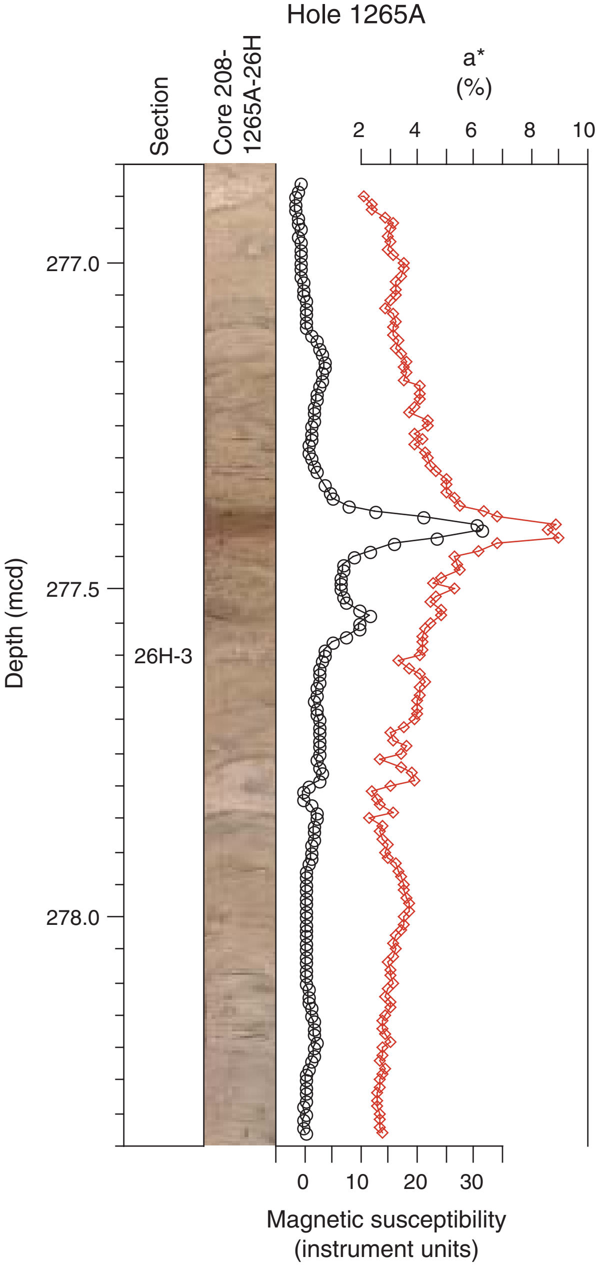

Figure F23. Composite digital image, carbonate content (blue), magnetic susceptibility (black), and chromaticity (a*; red) across the Paleocene/Eocene boundary from ~313.7 to ~316.6 mcd (Sections 208-1265A-29H-6 through 29H-7 and 208-1265D-4H-4 through 5H-CC).

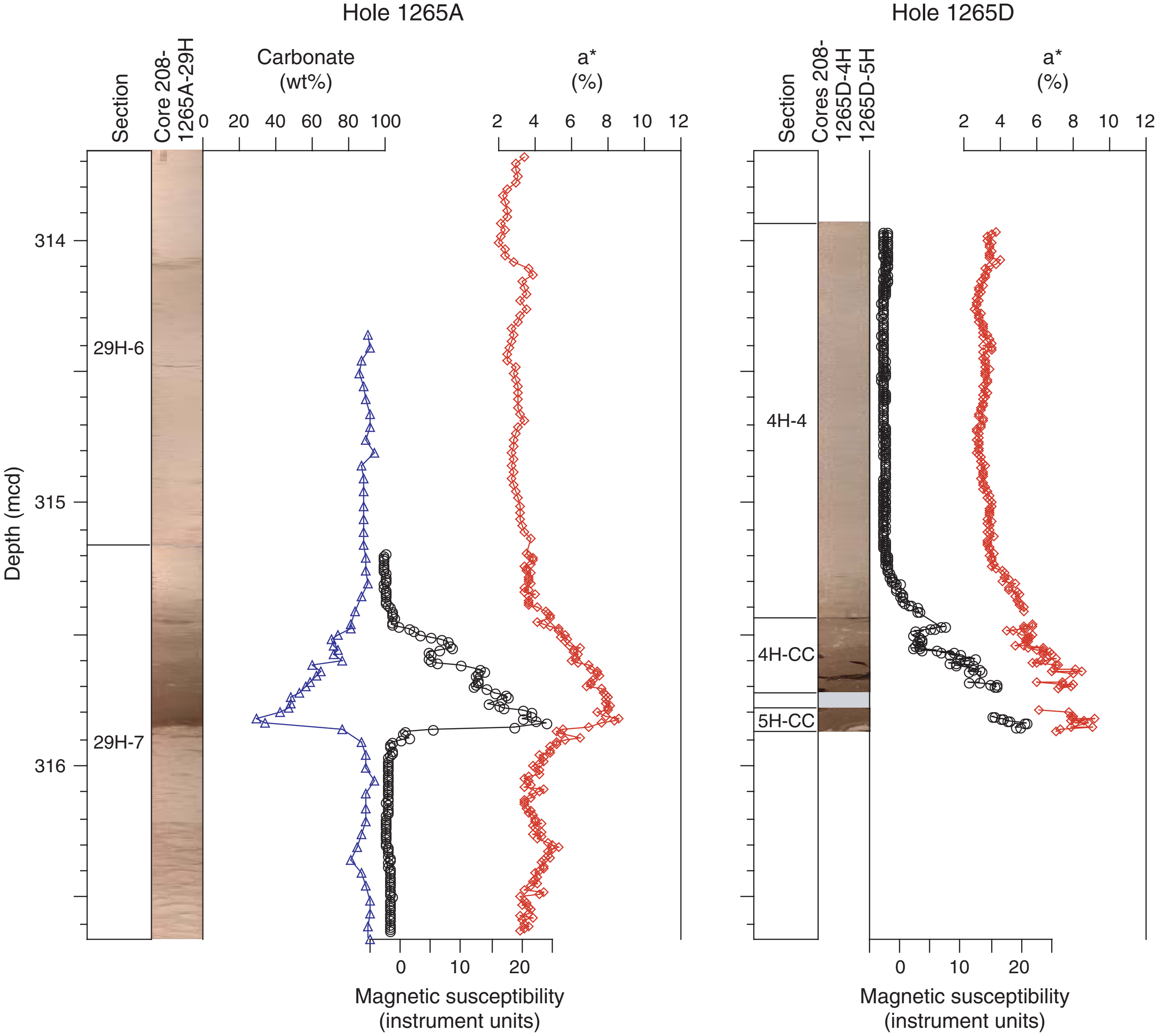

Figure F24. Summary of composite planktonic foraminiferal and calcareous nannofossil biozonation constructed for Site 1265. Paleobathymetric history of Site 1265 is inferred from benthic foraminifers shown on right. Shading indicates reworking and downslope transport. Nanno = nannofossils. B = bottom. P/E = Paleocene/Eocene boundary.

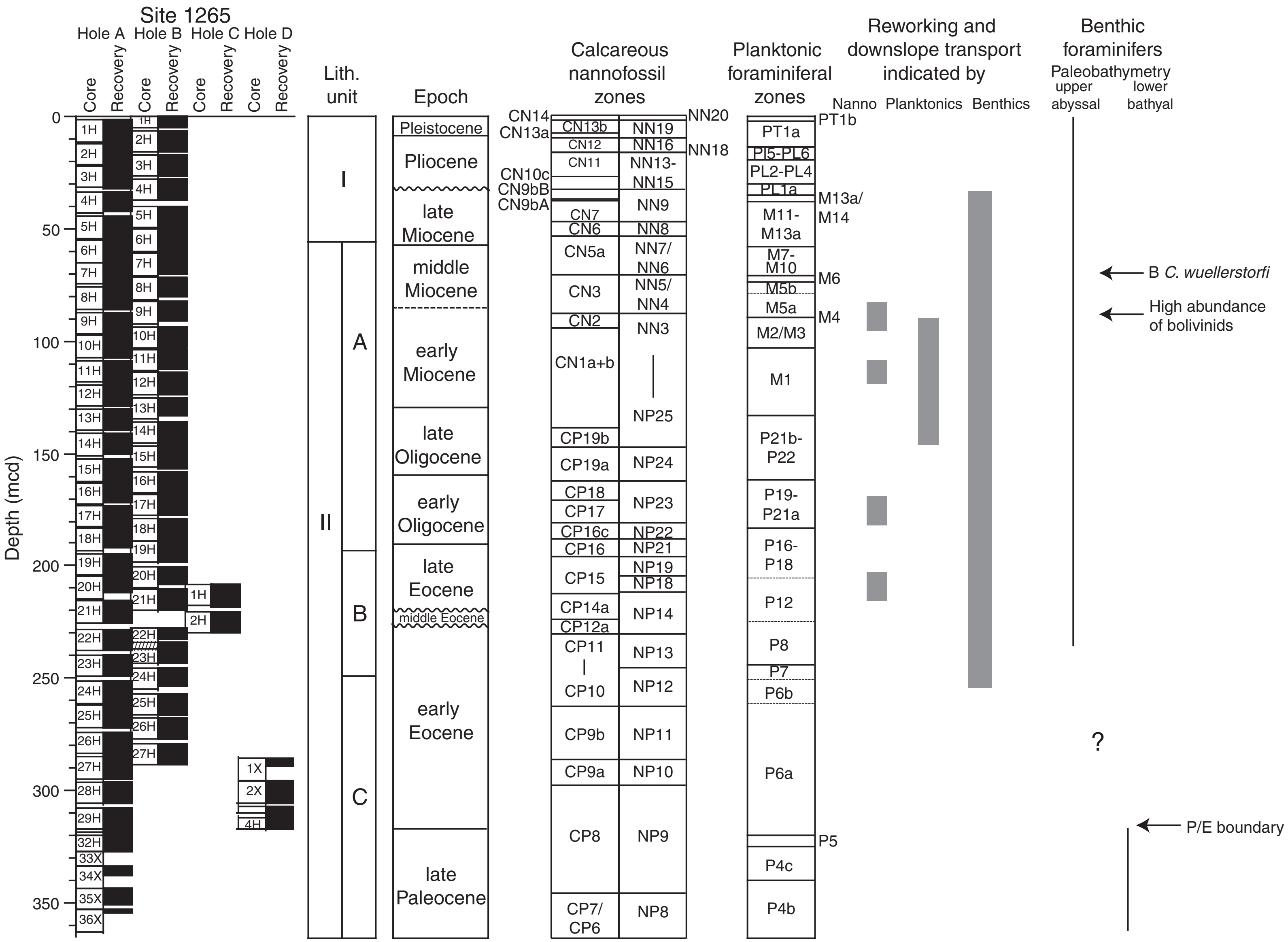

Figure F25. Summary of sedimentation rates at Site 1265 constructed using datum levels of calcareous nannofossils and planktonic and benthic foraminifers.

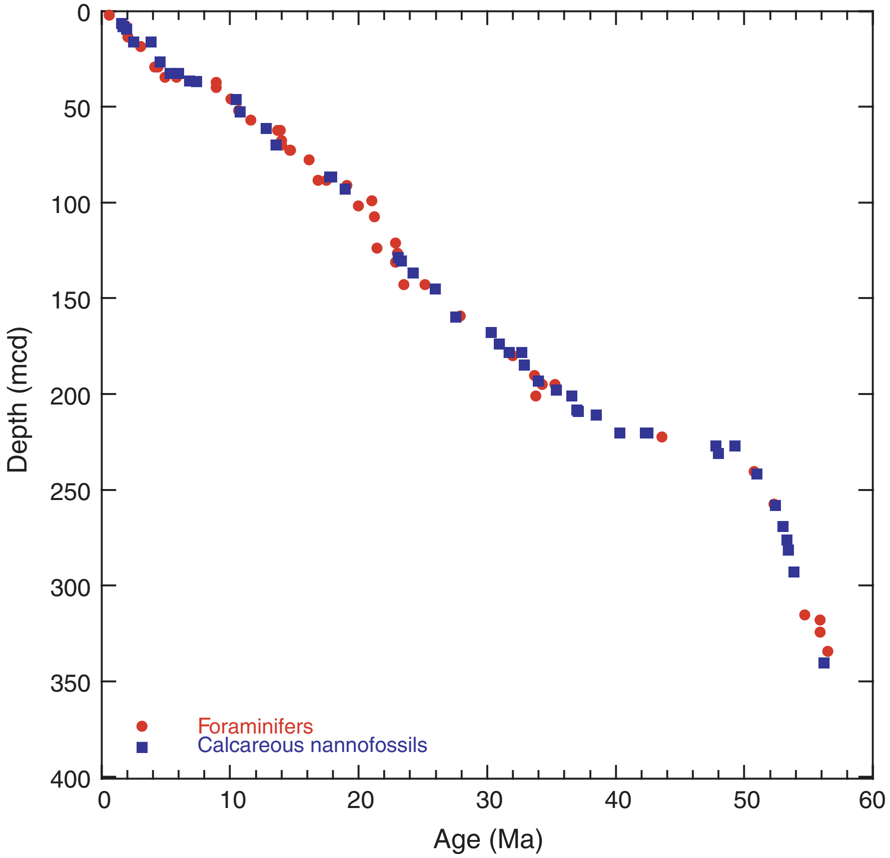

Figure F26. Results of a test to determine the effects of core scraping (see text) on the magnetization of soft-sediment archive halves. **A, B.** Inclination and intensity of Sections 208-1265B-7H-5 and 7H-6 after demagnetization at 15 mT and before scraping (circles), after scraping without further demagnetization (squares), and after scraping followed by redemagnetization to 15 mT (triangles). Note the large increase in intensity following scraping that is mostly removed by redemagnetization to 15 mT. **C.** Inclination of whole-round and archive-half Section 205-1265B-10H-2 before and after scraping. **D.** Inclination of whole-round and working-half Section 205-1265B-10H-2 before and after scraping. All measurements in C and D were made immediately following demagnetization to 15 mT.

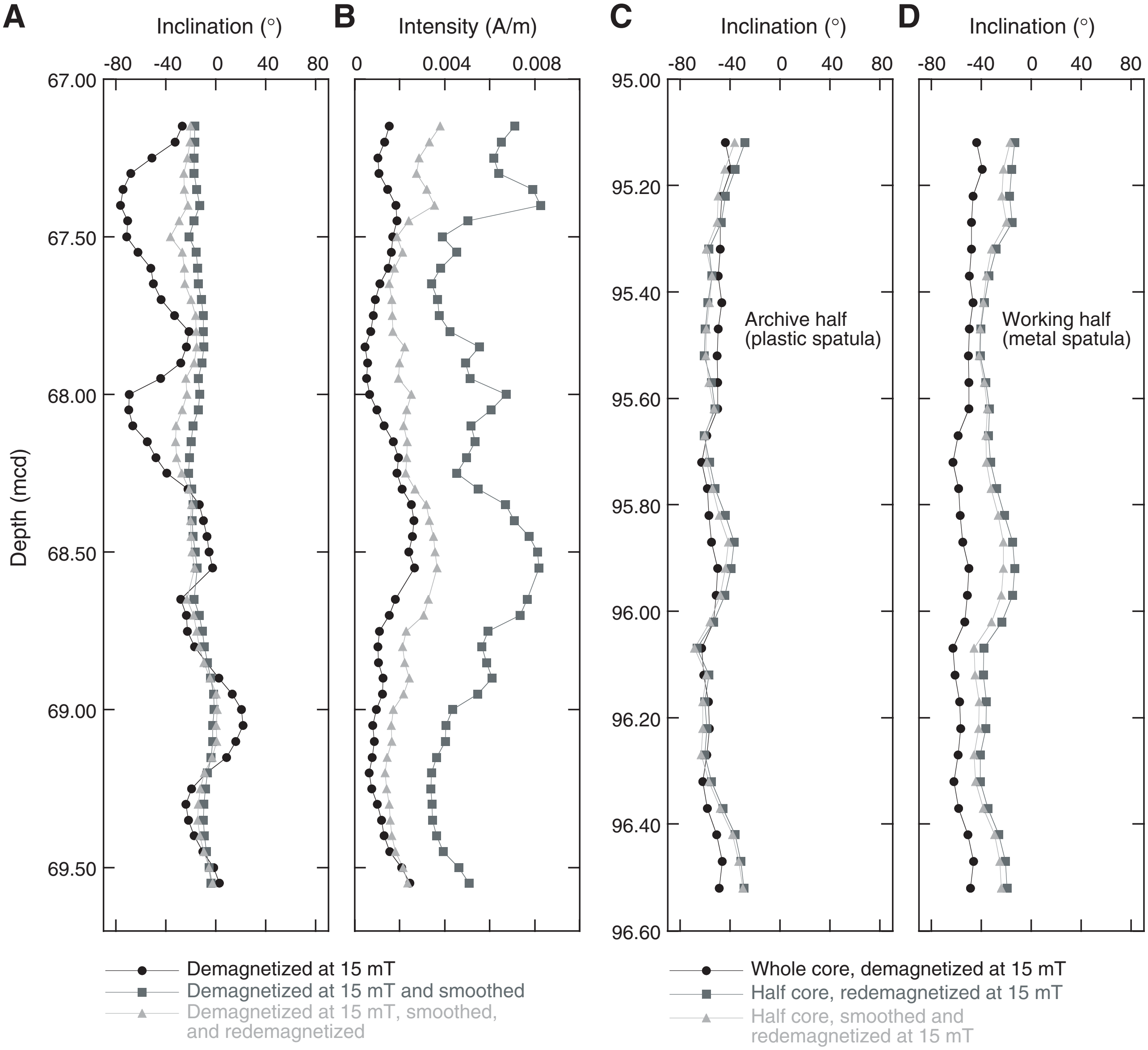

Figure F27. Downhole variation in intensities of remanent magnetization before (gray) and after (black) demagnetization at 15 mT in Holes 1265A, 1265B, 1265C, and 1265D.

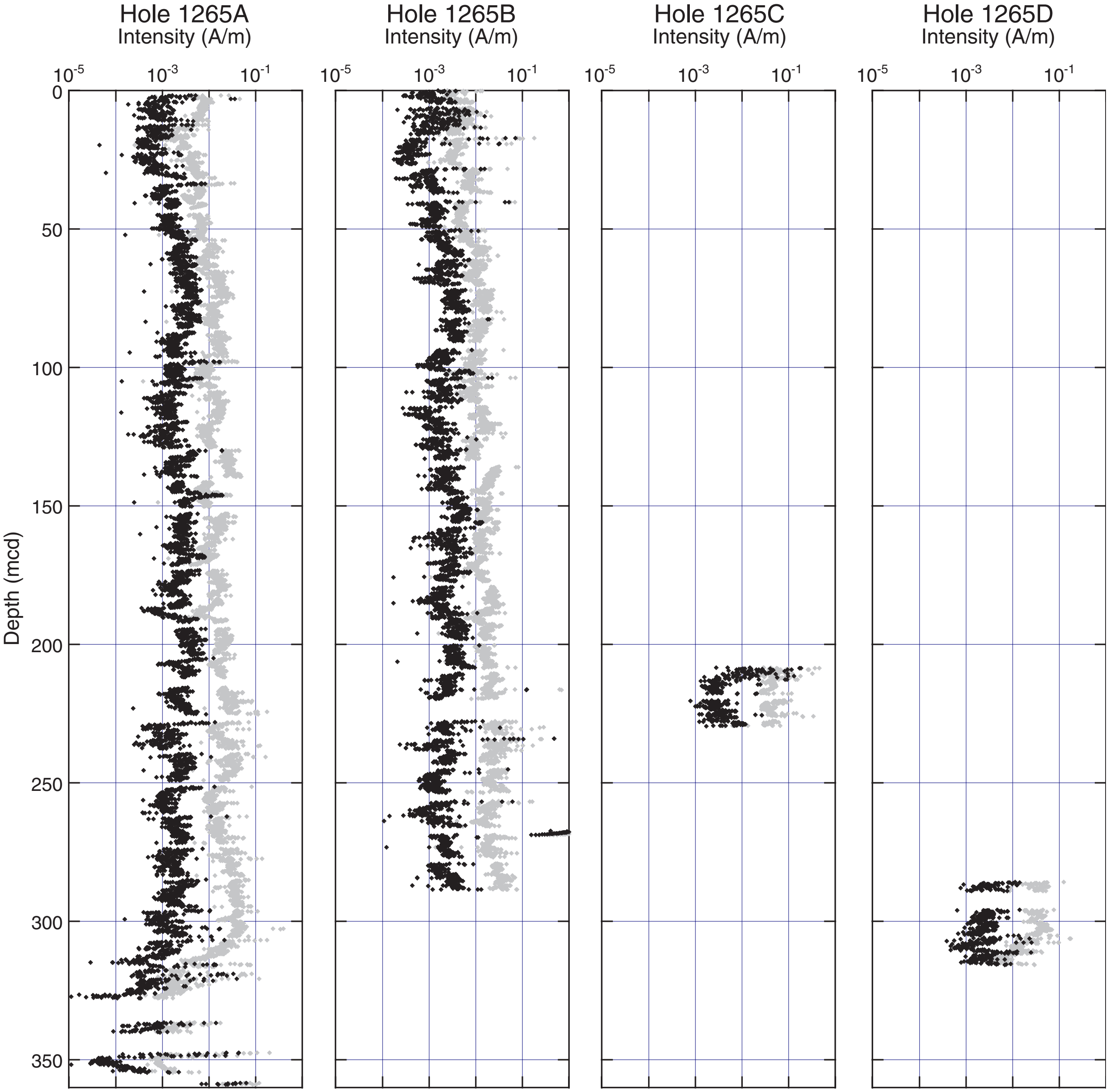

Figure F28. Downhole variation in initial magnetic susceptibility in Holes 1265A, 1265B, 1265C, and 1265D.

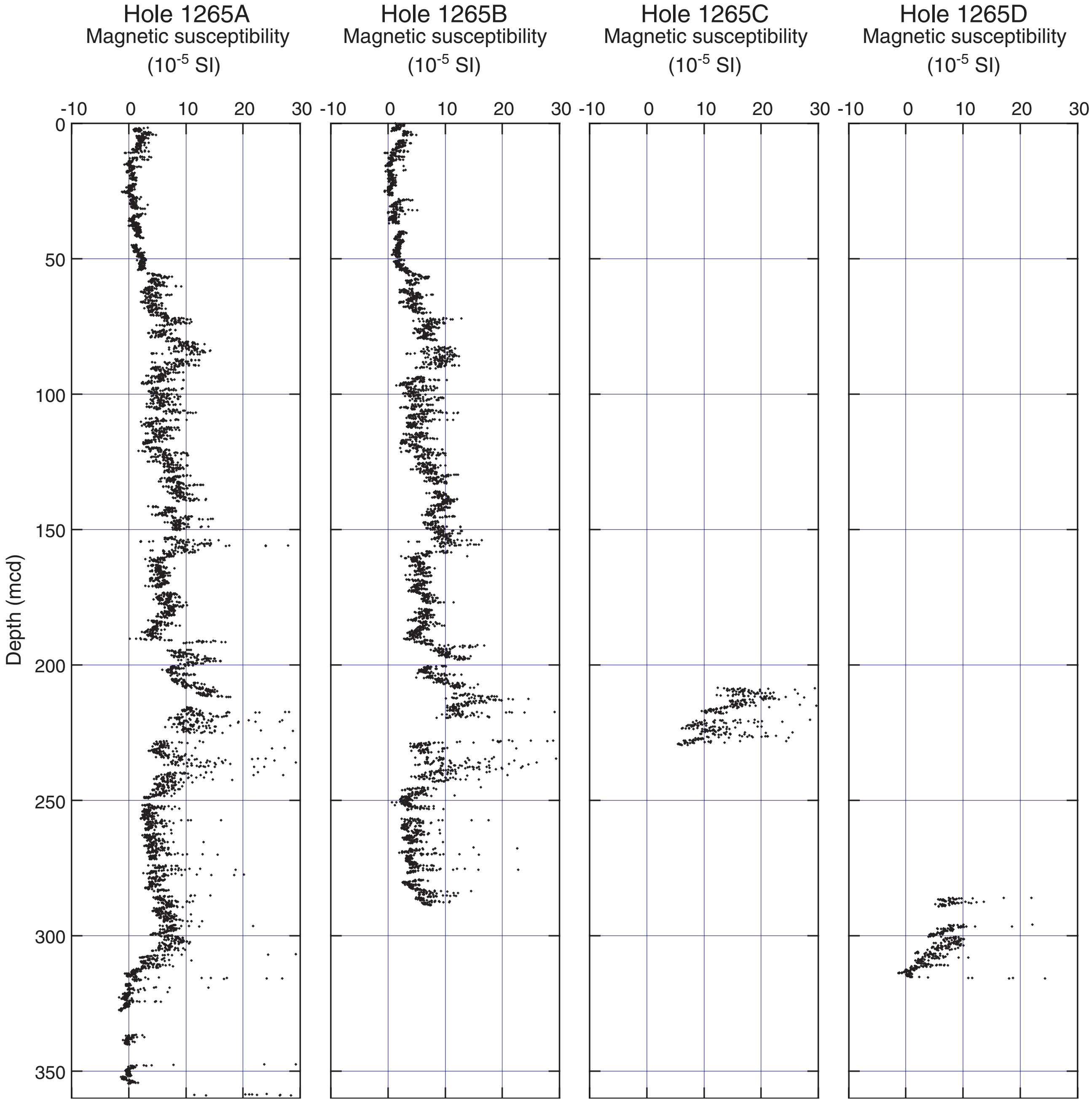

Figure F29. Downhole variation in depositional remanent magnetization after demagnetization to 15 mT and normalized by susceptibility ($nDRM_{15\ mT}$) in Holes 1265A, 1265B, 1265C, and 1265D.

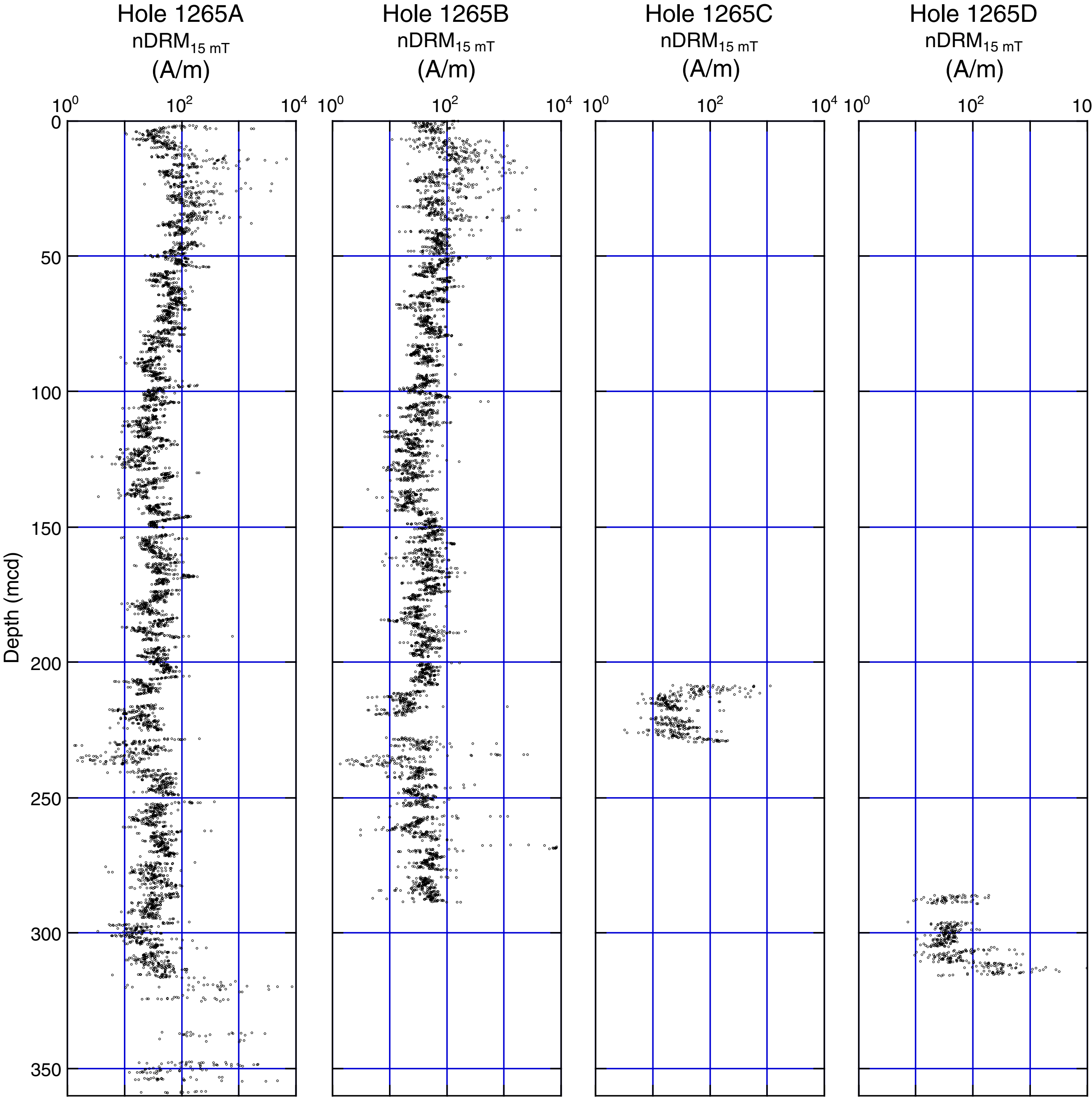

Figure F30. Preliminary magnetostratigraphic interpretation. Inclination data after demagnetization at 15 mT are shown for Holes 1263A, 1263B, and 1263C. Data within 50 cm of a core top and 5 cm of section ends are not shown. Core breaks are denoted by green squares. Black rectangles = normal polarity, white = reversed polarity, and shaded = uncertain polarity. X = intervals with no core recovery. **A.** 0–75 mcd. (Continued on next three pages.)

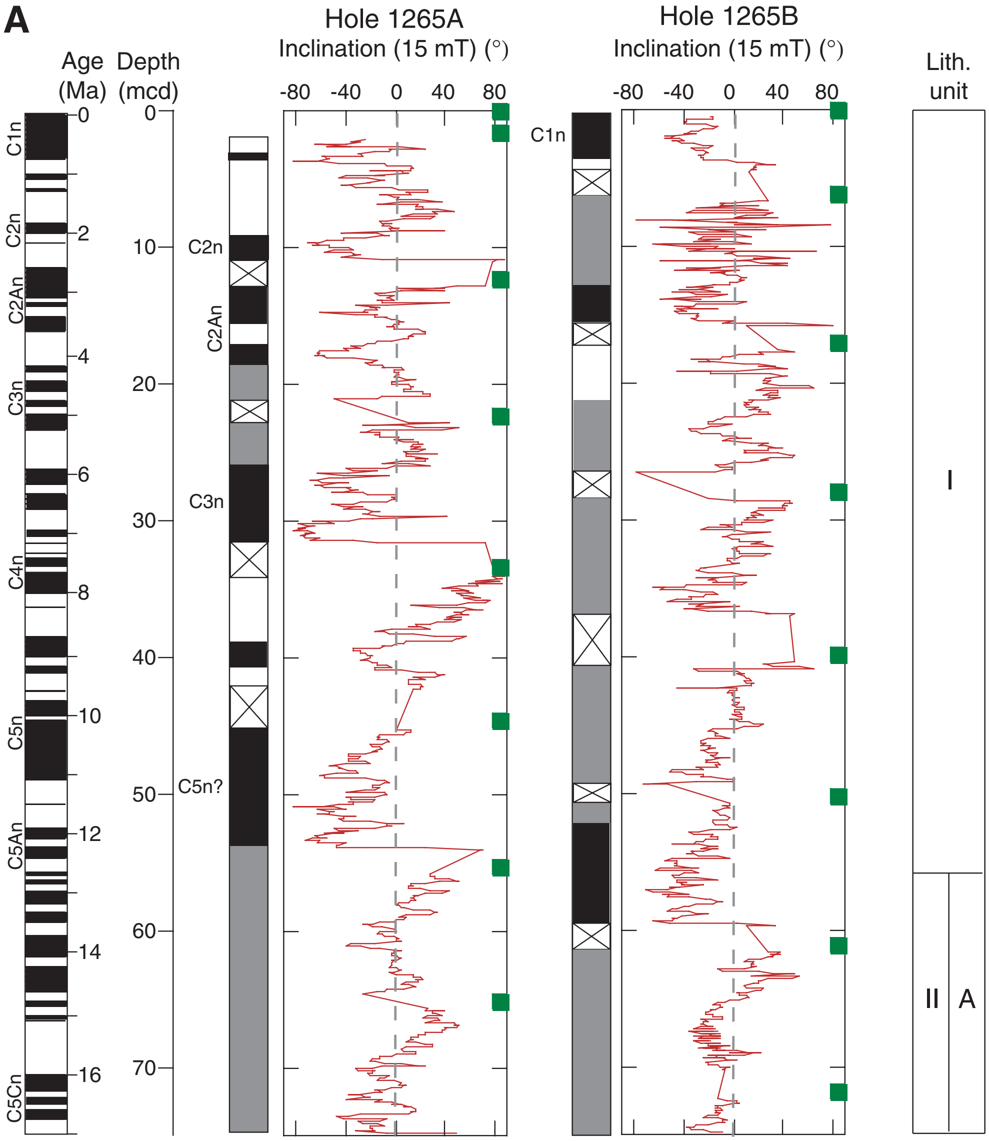

Figure F30 (continued). B. 65–150 mcd. O/M = Oligocene/Miocene boundary.

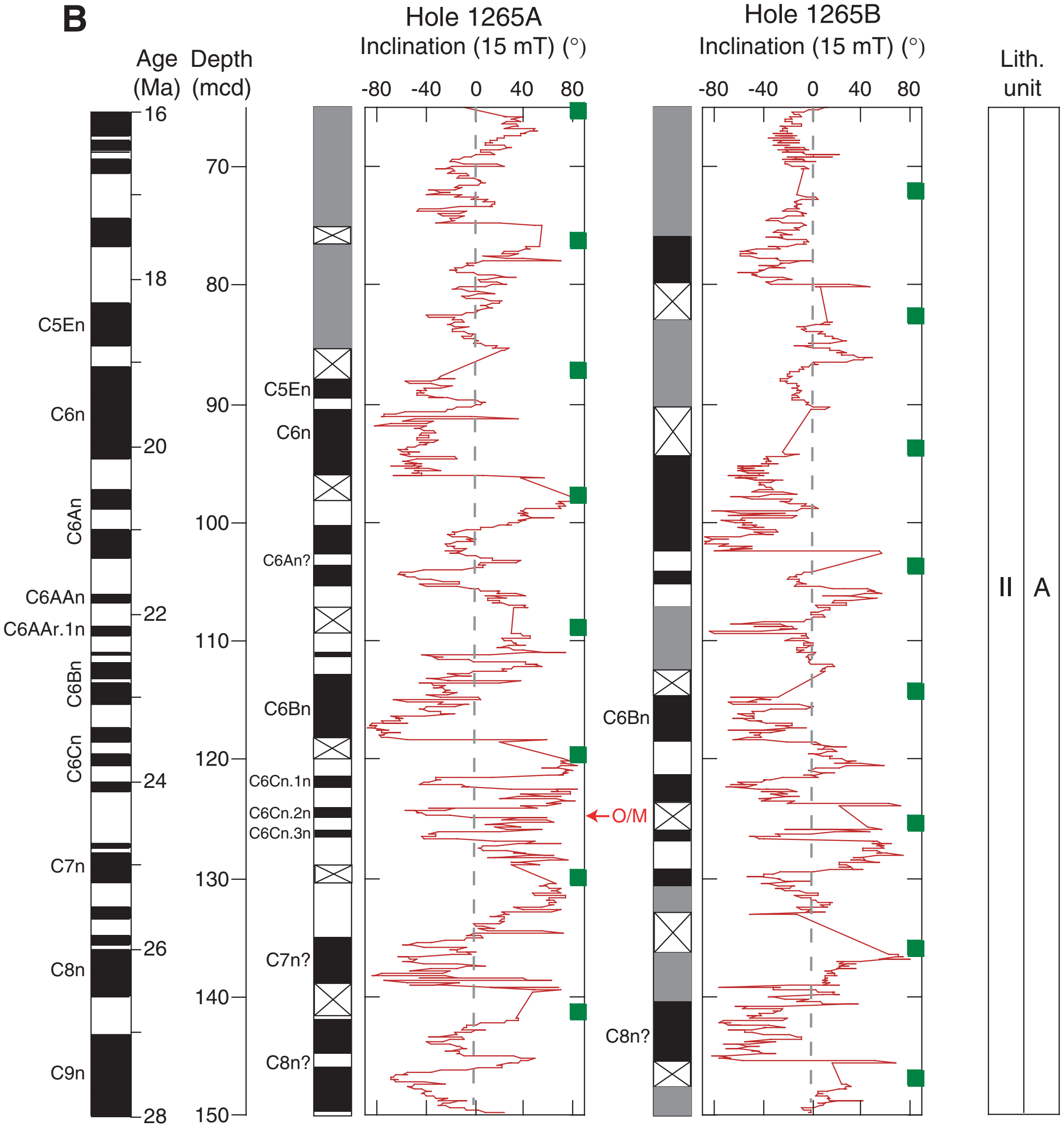

Figure F30 (continued). C. 140–225 mcd.

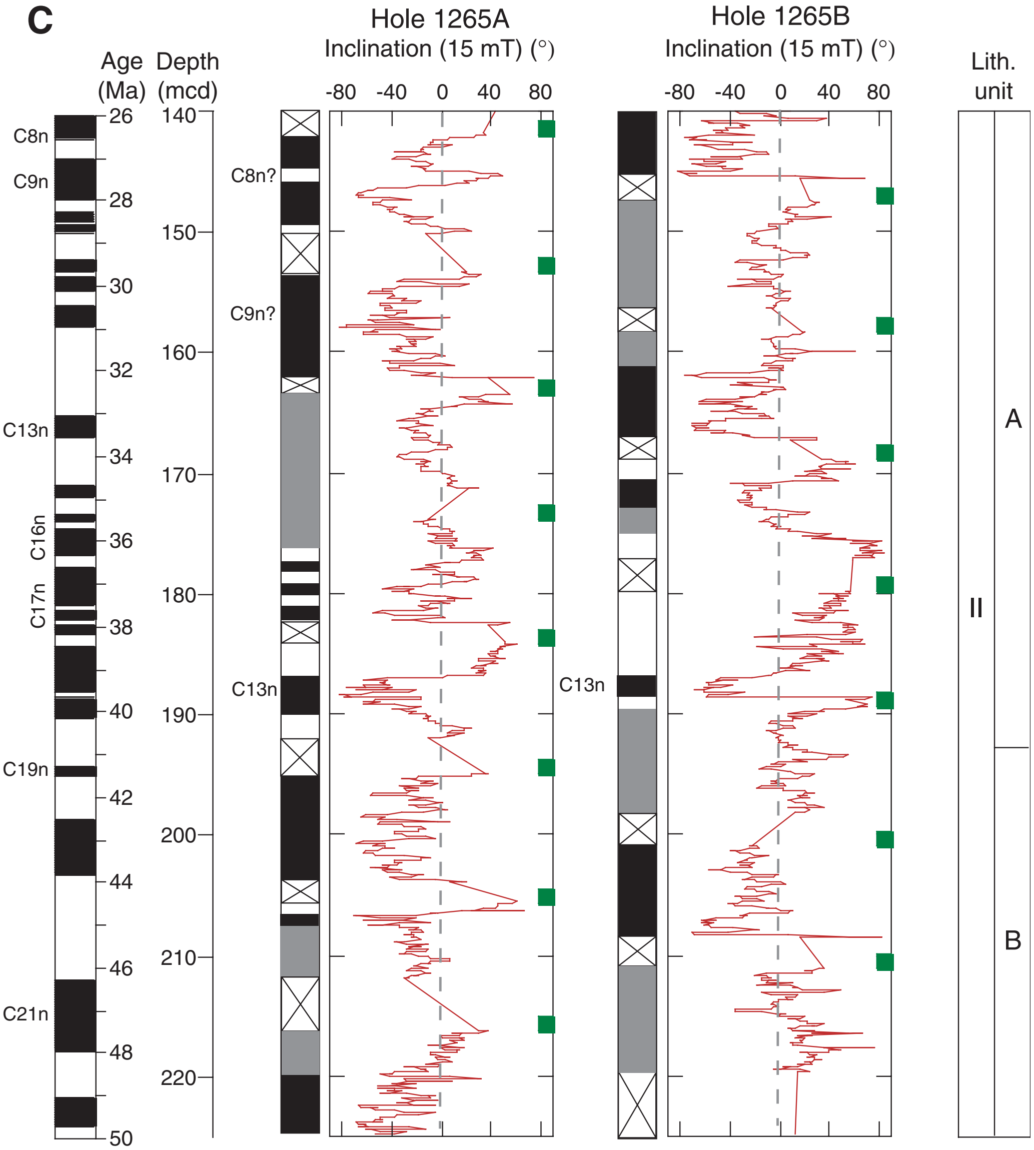

Figure F30 (continued). **D.** 115–320 mcd. P/E = Paleocene/Eocene boundary.

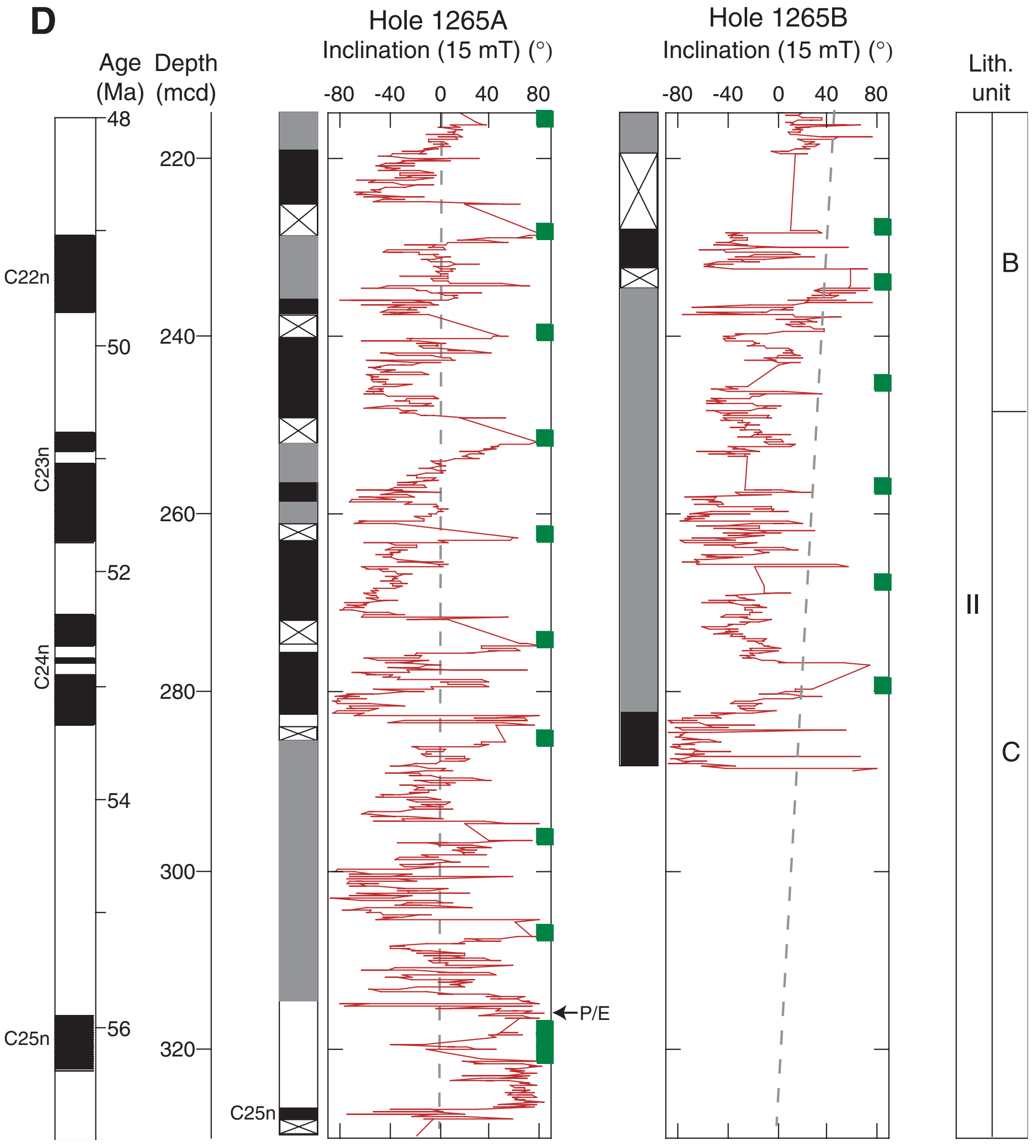

Figure F31. Profiles of chemical constituents in interstitial waters from ODP Site 1265. Error bars (1 σ relative standard deviation as a percentage) are plotted where they are larger than the plot symbols. **A.** Alkalinity. **B.** Chloride. **C.** Sodium. **D.** Potassium. **E.** Calcium. **F.** Magnesium. **G.** Strontium. **H.** Lithium. **I.** Boron. **J.** Barium. **K.** Sulfate. **L.** Manganese. **M.** Iron. **N.** Silica. **O.** Zinc.

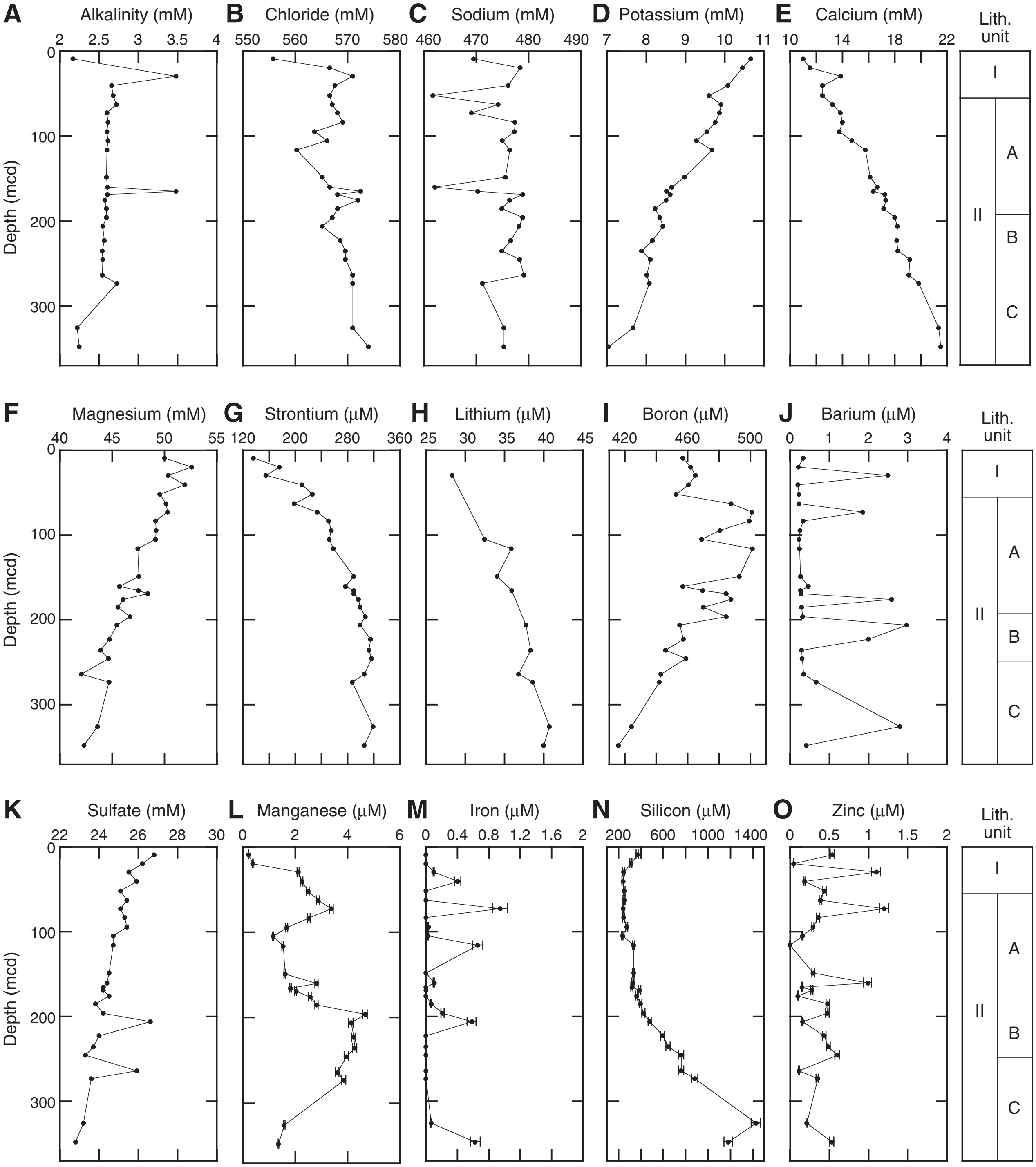

Figure F32. Light microscope images of manganese oxide nodules containing planktonic foraminiferal tests from (**A**, **B**) Sample 208-1265A-18H-CC and (**C**, **D**) Sample 208-1265A-27H-CC. Note the soft nature of the nodules demonstrated in D.

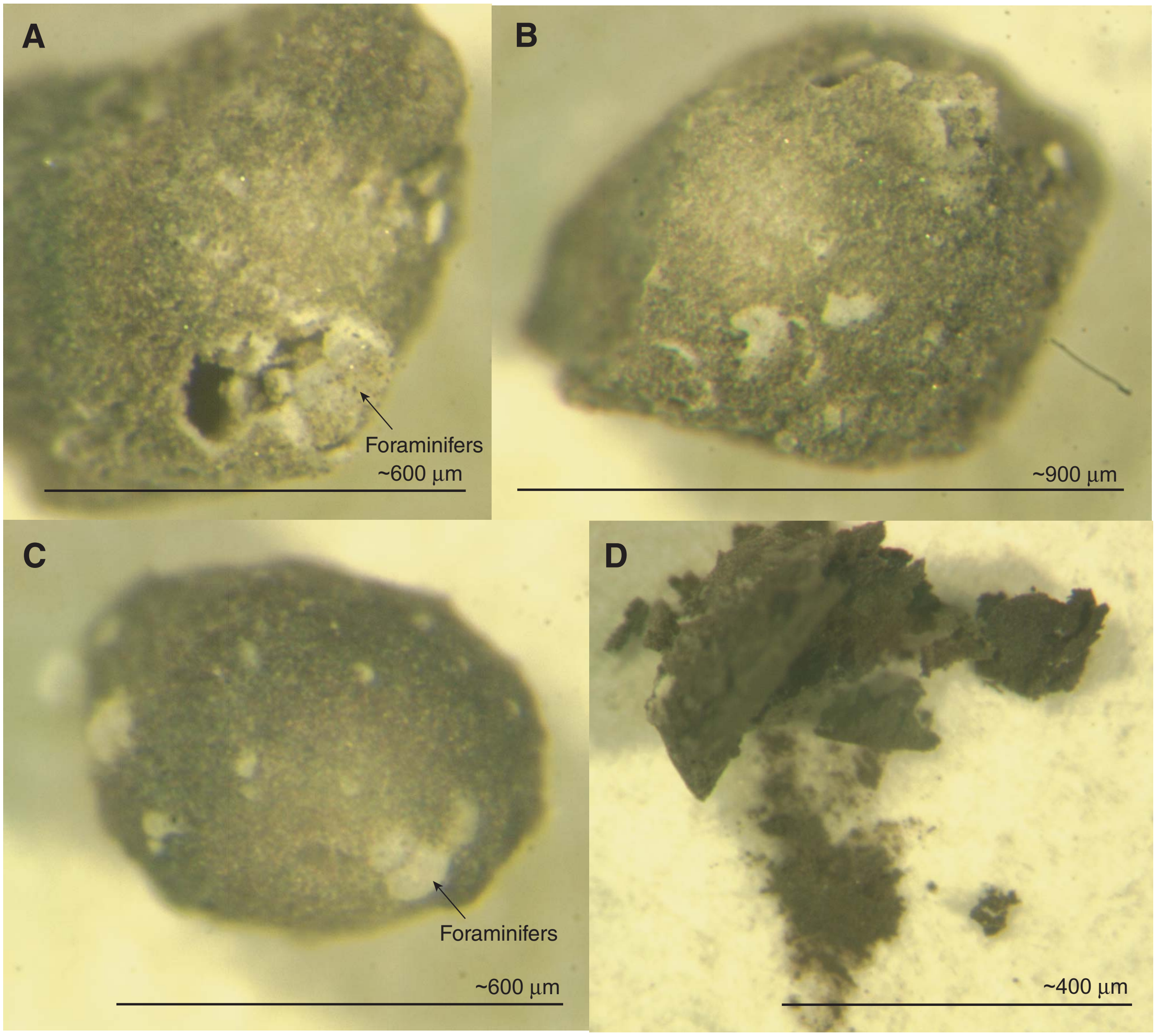

Figure F33. Sedimentary carbonate contents vs. composite depth for (**A**) the entire section and (**B**) the P/E boundary interval at high resolution.

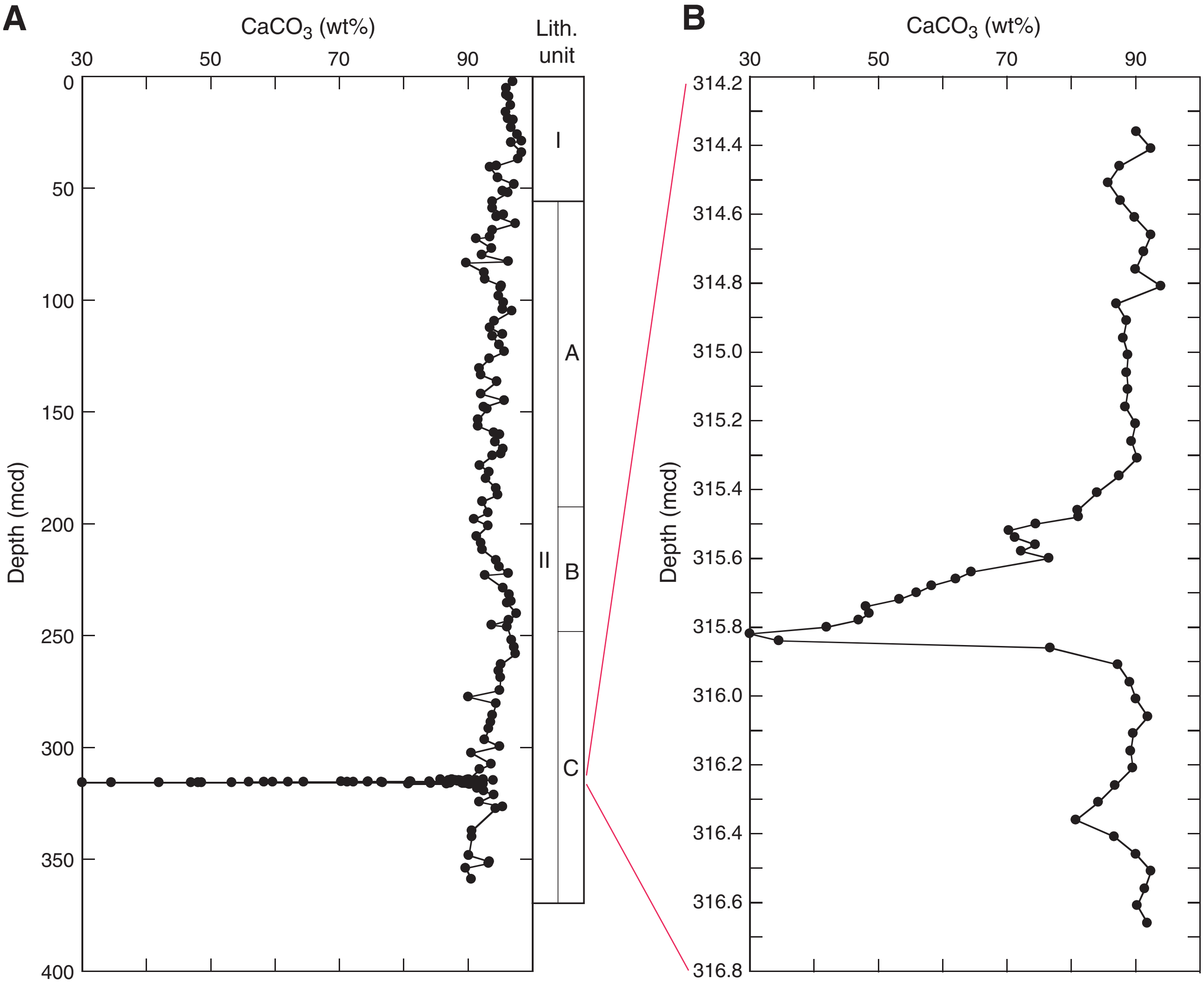

Figure F34. Mass chromatograms at m/z 85 for hexane eluates (aliphatic hydrocarbons) from carbonate samples (see Fig. F35, p. 71, for mass spectra of labeled peaks).

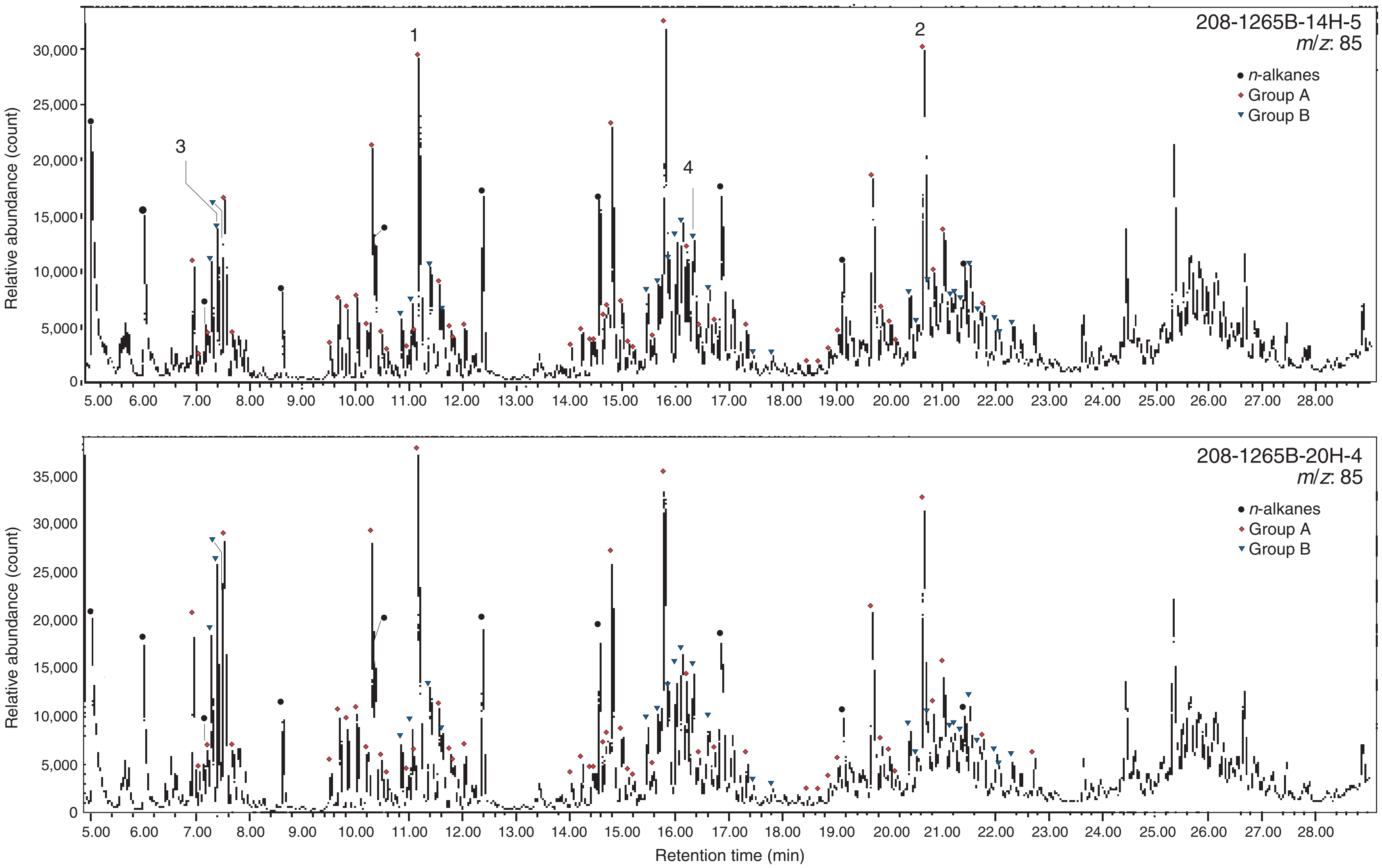

Figure F35. Mass spectra of selected peaks in hexane eluate from Section 208-1265A-14H-5 (see Fig. **F34**, p. 70, for peak assignments). **A.** Mass spectra from peak 1. **B.** Mass spectra from peak 2. **C.** Mass spectra from peak 3. **D.** Mass spectra from peak 4.

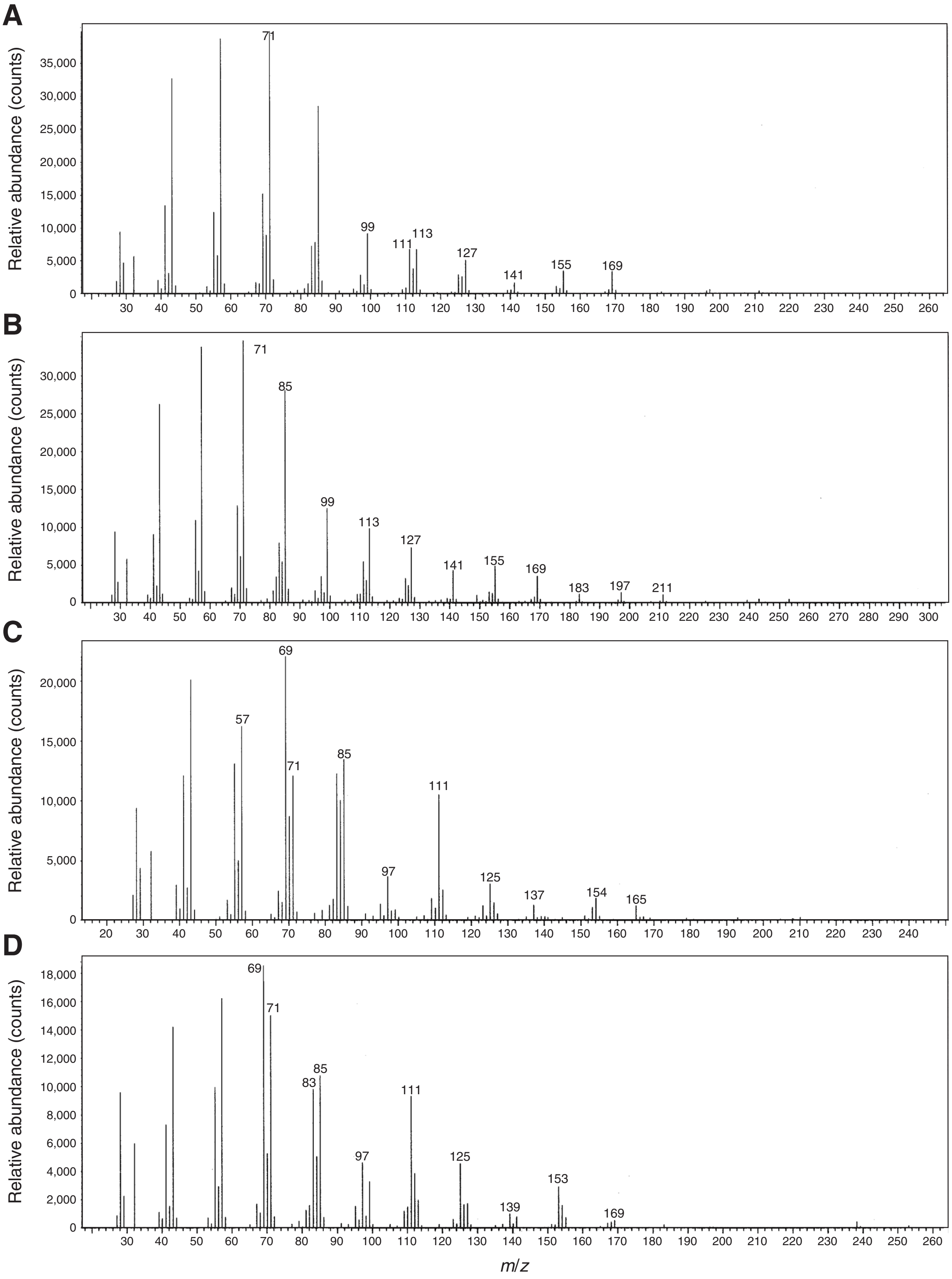

Figure F36. Summary of the logging operations undertaken in Hole 1265A. Triple combo = triple combination tool string, MGT = Multi-Sensor Gamma Ray Tool, FMS-sonic = Formation MicroScanner-sonic tool string, WST-3 = three-component Well Seismic Tool. TD = total depth.

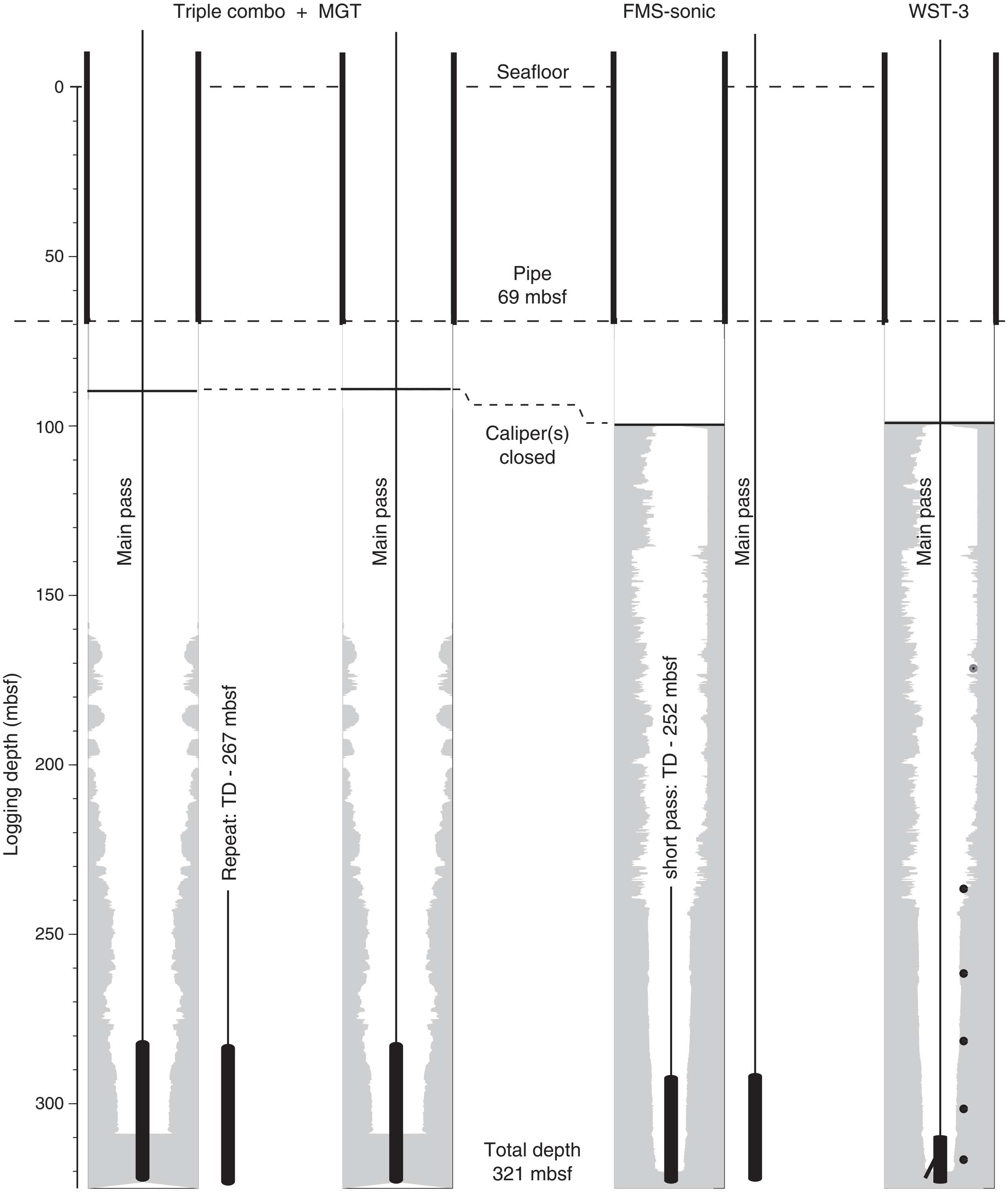

Figure F37. Quality control of the downhole logging runs. Triple combo tool string (red lines): (**A**) caliper, (**B**) normalized vertical tool acceleration (NAz), and (**C**) wavelet transform of NAz between 90 and 250 mbsf. FMS-sonic tool string (blue lines): (**D**) Calipers, (**E**) NAz, and (**F**) wavelet transform of NAz between 100 and 320 mbsf, (**G**) horizontal acceleration (Ah) and (**H**) wavelet transform of Ah, and (**I**) hole azimuth (Hazi) and orientation (p1AZ). Note the discrepancy between the triple combo and the FMS caliper data.

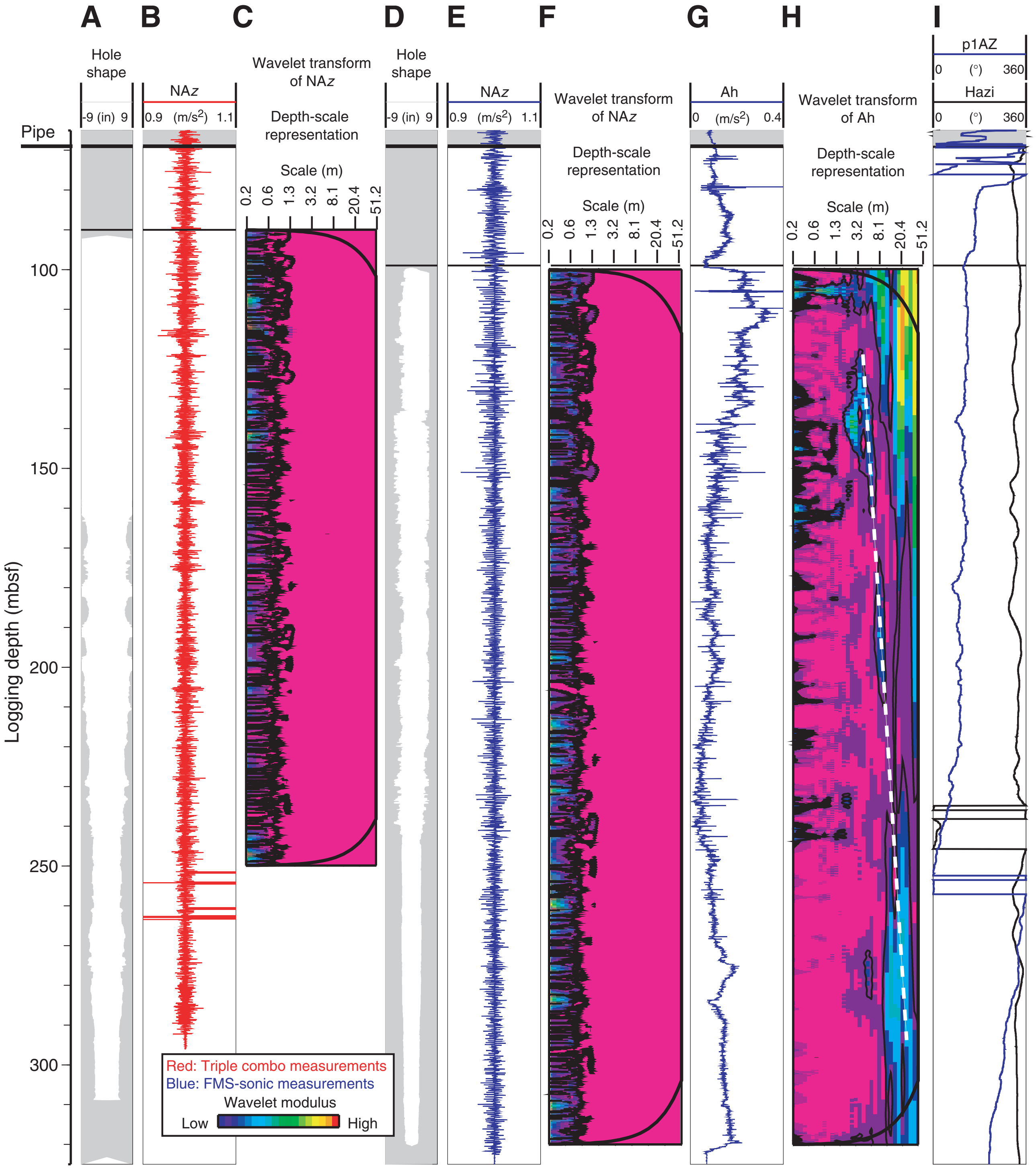

Figure F38. Depth shifting of downhole logging data. **A.** Hole shape. **B.** Total natural gamma radiation HSGR_m from the Hostile Environment Natural Gamma Ray Sonde tool on the main pass of the triple combo tool string and multisensor track (MST) natural gamma radiation (NGR) measured on whole cores. The core data were used as reference for depth shifting. **C.** Total gamma radiation HSGR_r from the repeat log plotted along with HSGR_m. **D.** Total gamma radiation (GR) from the Multi-Sensor Gamma Ray Tool (MGT) log with respect to HSGR_m. **E.** Hole shape measured by the FMS-sonic calipers. **F.** Computed gamma ray (ECGR) from the SGT tool on the FMS-sonic tool string plotted along with the total gamma radiation (HSGR_m) from the HNGS main run on the triple combo. **G, H.** Combined plot of HSGR_m, HSGR_r, GR, and ECGR, including close-up, showing the good depth and pattern matching between the natural gamma ray logs of the different runs. (**Figure shown on next page.**)

Figure F38 (continued). (Caption shown on previous page.)

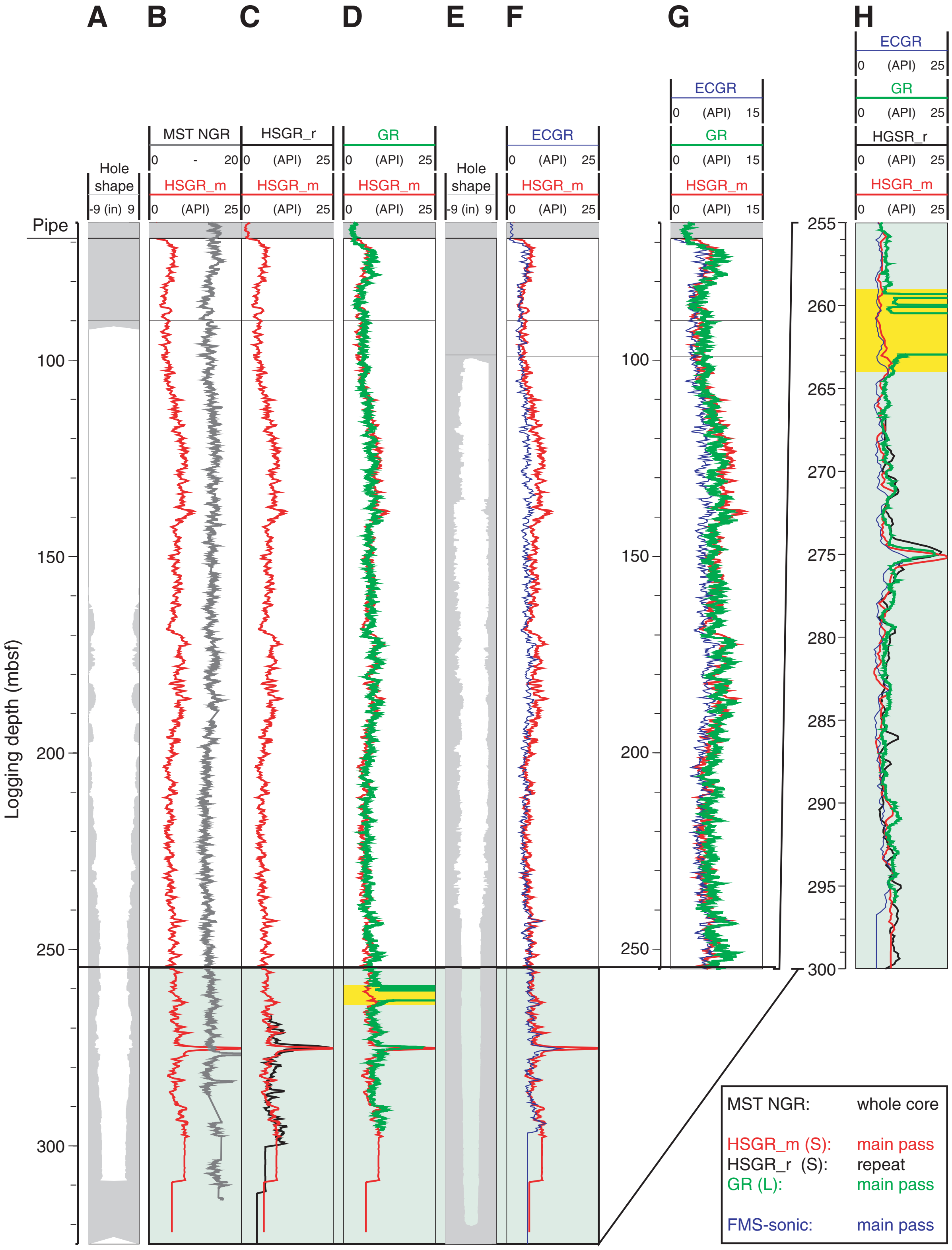

Figure F39. Logging stratigraphy. **A.** Hole shape and total gamma ray (HSGR). **B.** Computed gamma ray (HCGR) and uranium contribution (HURA). **C.** Potassium (HFK) and thorium (HTHO) contributions to natural radioactivity. **D.** Deep (IDPH), intermediate (IMPH), and shallow (SFLU) resistivities. **E.** Porosity (APLC) and capture cross section (Σf). **F.** Formation density (RHOM) and photoelectric factor (PEF). **G.** Downhole compressional velocity (V_P). **H.** Logging subunits. **I.** Lithostratigraphic subunits.

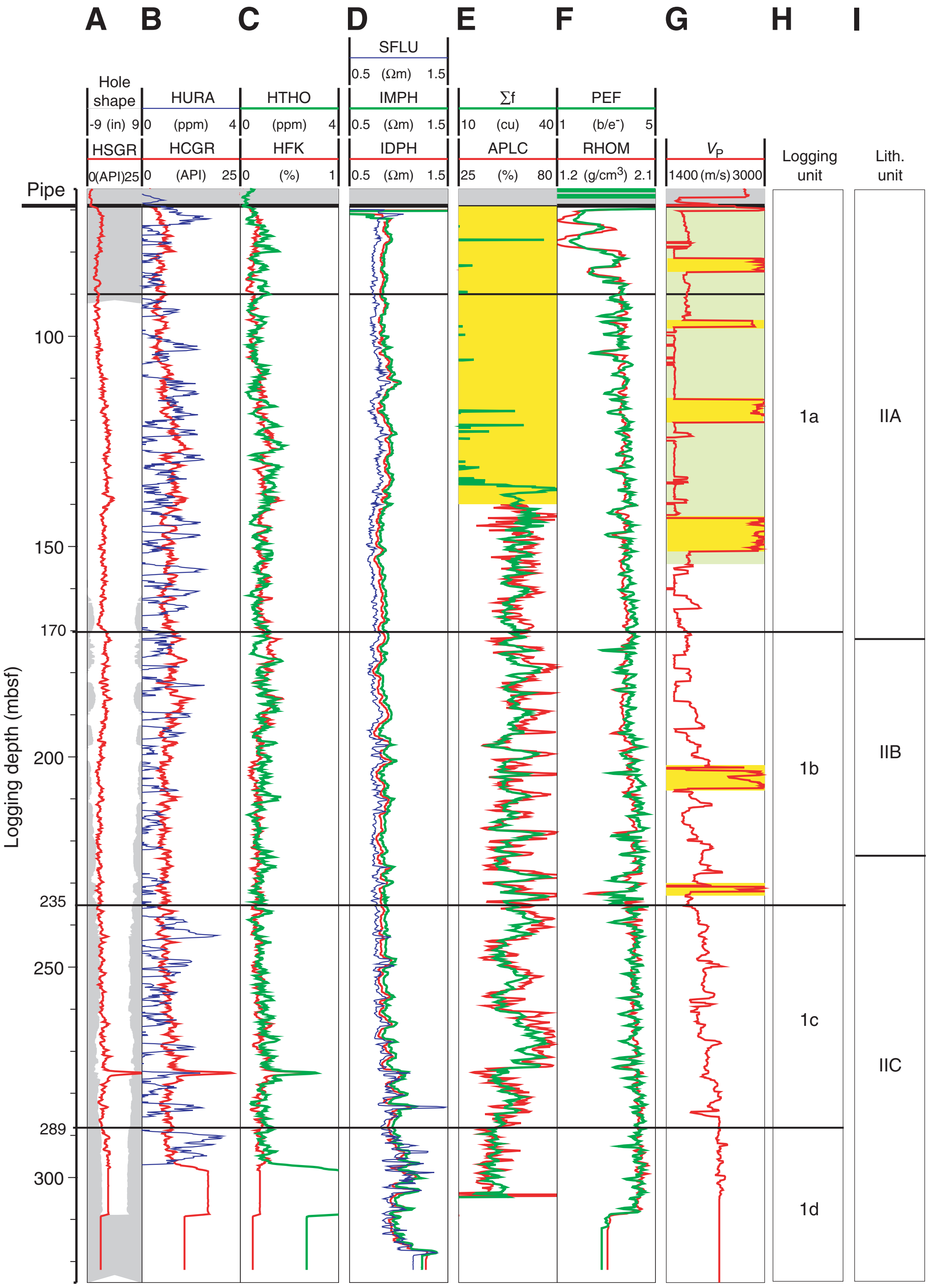

Figure F40. Equivalent logging depth construction based on mapping the core-based composite section to the downhole logging section using natural gamma radiation data (MST-NGR and HNGS-HSGR, respectively). HSGR = total gamma radiation.

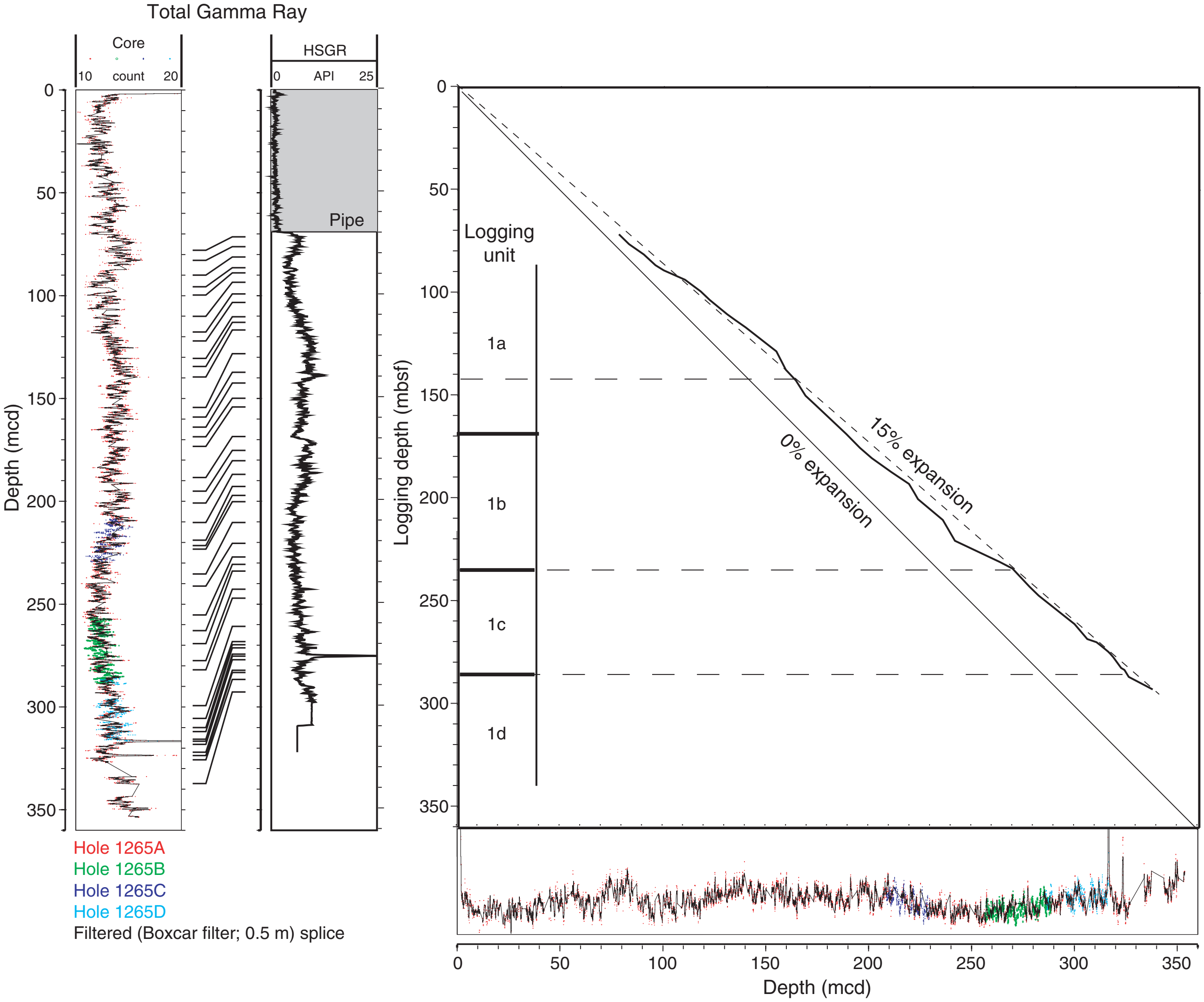

Figure F41. Core-log integration. **A.** Hole shape and total gamma radiation (HSGR), porosity (APLC), density (RHOM), *P*-wave velocity (V_P), plotted along with the equivalent data from cores, lithostratigraphy, and logging subunits. (Continued on next page.)

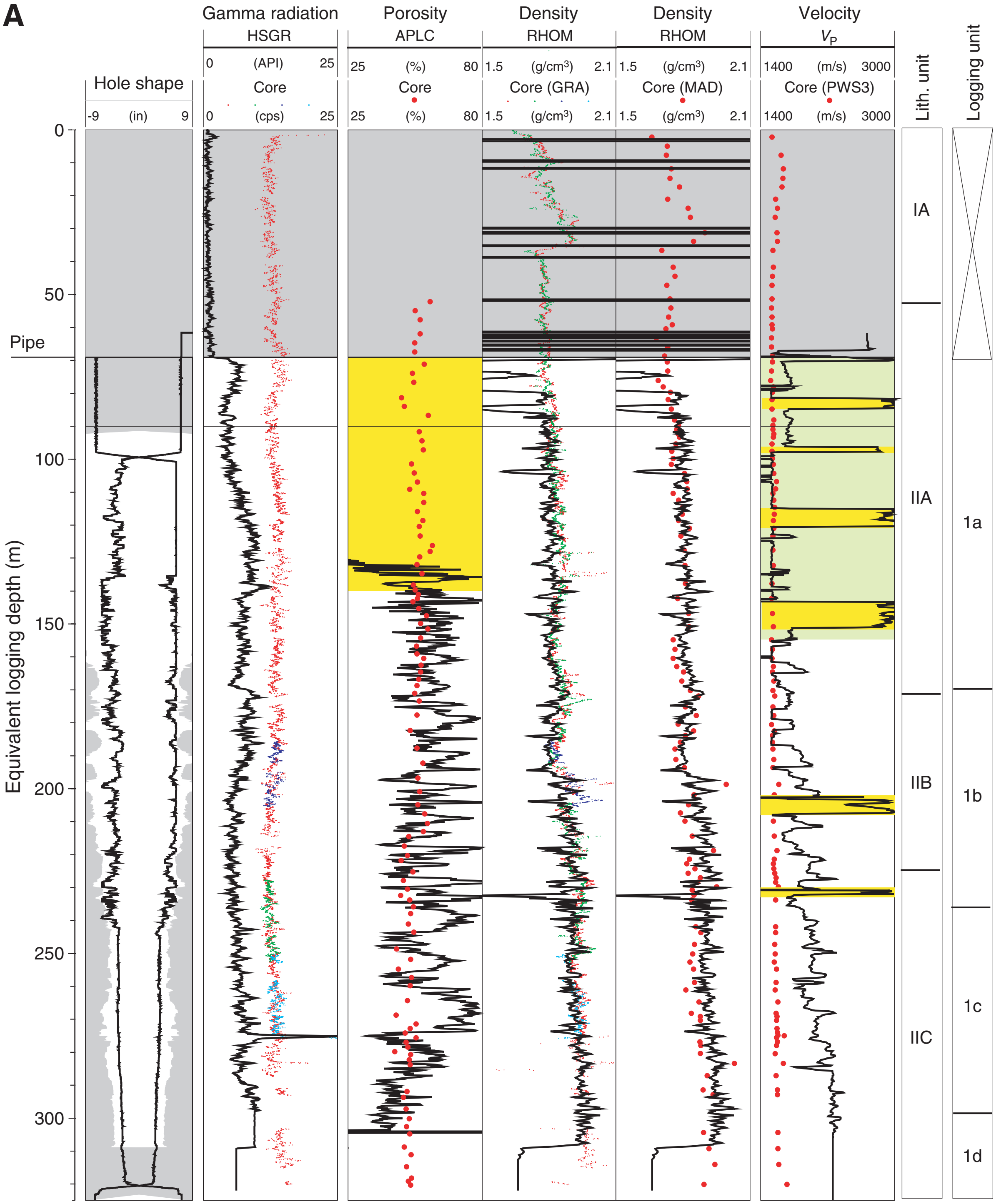

Figure F41 (continued). B. Lithology, magnetic susceptibility, and color reflectance data (L*, a*, and b*) from cores and lithostratigraphic and logging units vs. equivalent logging depth.

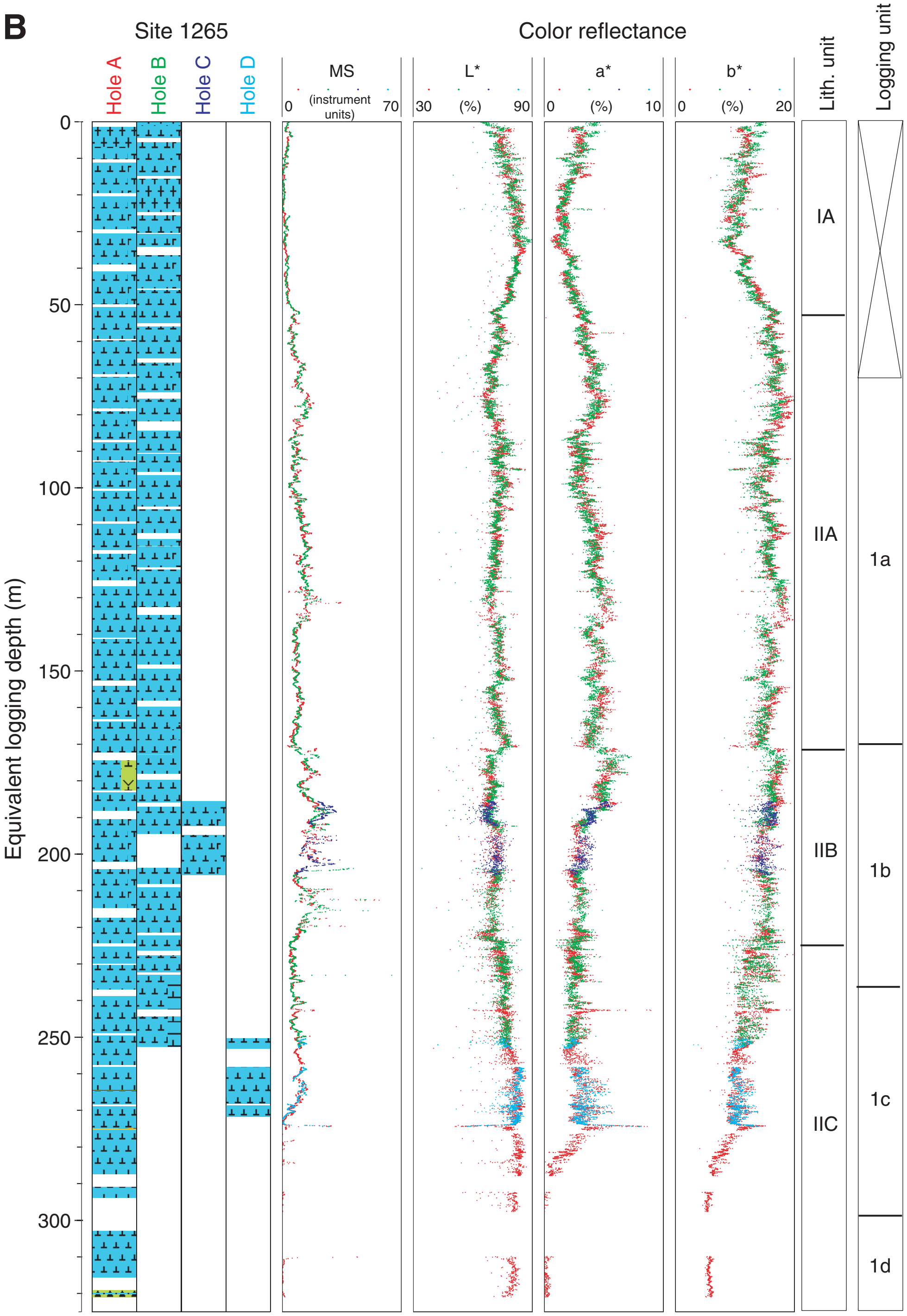

Figure F42. Formation MicroScanner (FMS) images and conductive layers between 245 and 255 mbsf showing (**A**) hole shape, (**B**) static and (**D**) dynamic (window height = 0.5 m) normalization of the microresistivity images, (**C**) conspicuous conductive layers, (**E**) total gamma radiation (HSGR from HNGS and gamma radiation [GR] from MGT) and (**F**) shallow resistivity (SFLU) logs, and (**G**) extracted FMS button records showing the poor pad/formation contact (red).

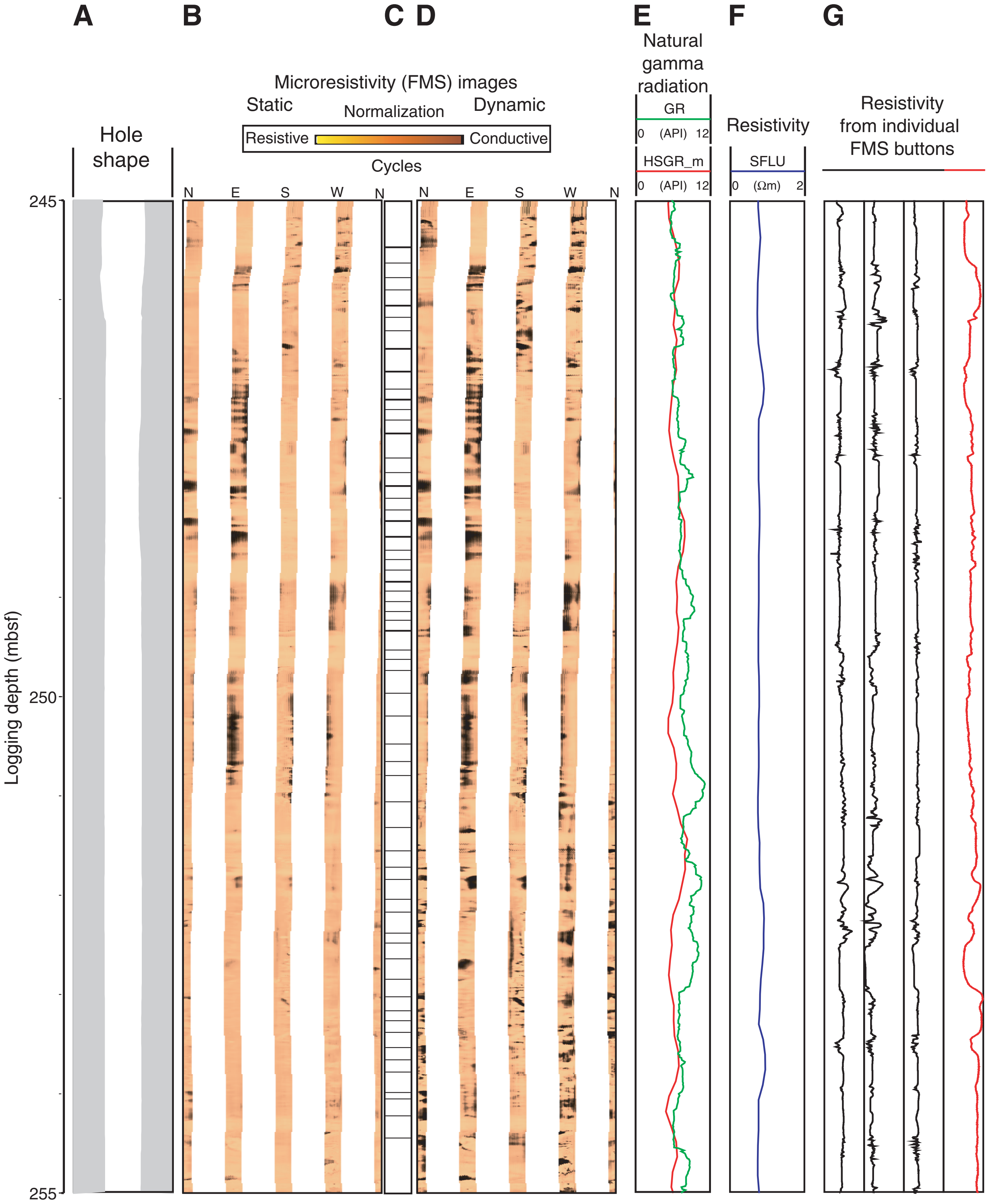

Figure F43. Formation MicroScanner (FMS) images and chert layers between 280 and 320 mbsf showing (**A**) hole shape, (**B**) static and (**D**) dynamic (window height = 0.5 m) normalization of the microresistivity images, (**C**) conductive (chert) layers, (**E**) total spectral gamma radiation (HSGR from HNGS and gamma radiation [GR] from the MGT) and (**F**) shallow resistivity (SFLU) logs, and (**G**) extracted FMS button records showing the poor pad–formation contact (red). Yellow rectangles = zone where stick-slip displacements occurred and impaired image quality (circled area).

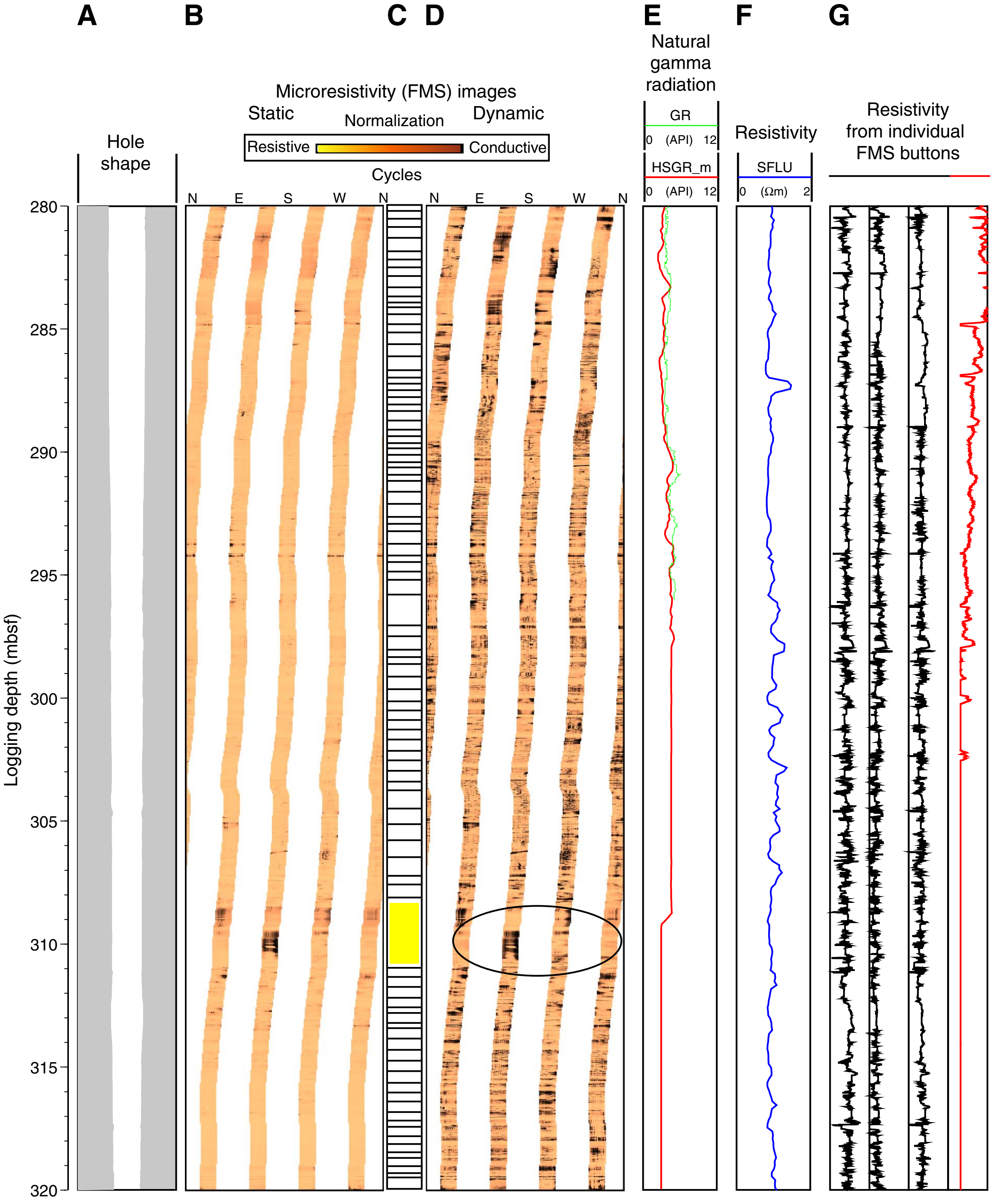

Figure F44. Formation MicroScanner images of chert layers (close-up of Fig. F43, p. 81, between 295 and 305 mbsf) showing (**A**) hole shape, (**B**) static and (**D**) dynamic (window height = 0.5 m) normalization of the microresistivity images, (**C**) interpreted chert layers, (**E**) shallow resistivity (SFLU) logs, and (**F**) extracted FMS button records. Yellow rectangles = zone where stick-slip displacements occurred and impaired image quality (circled area).

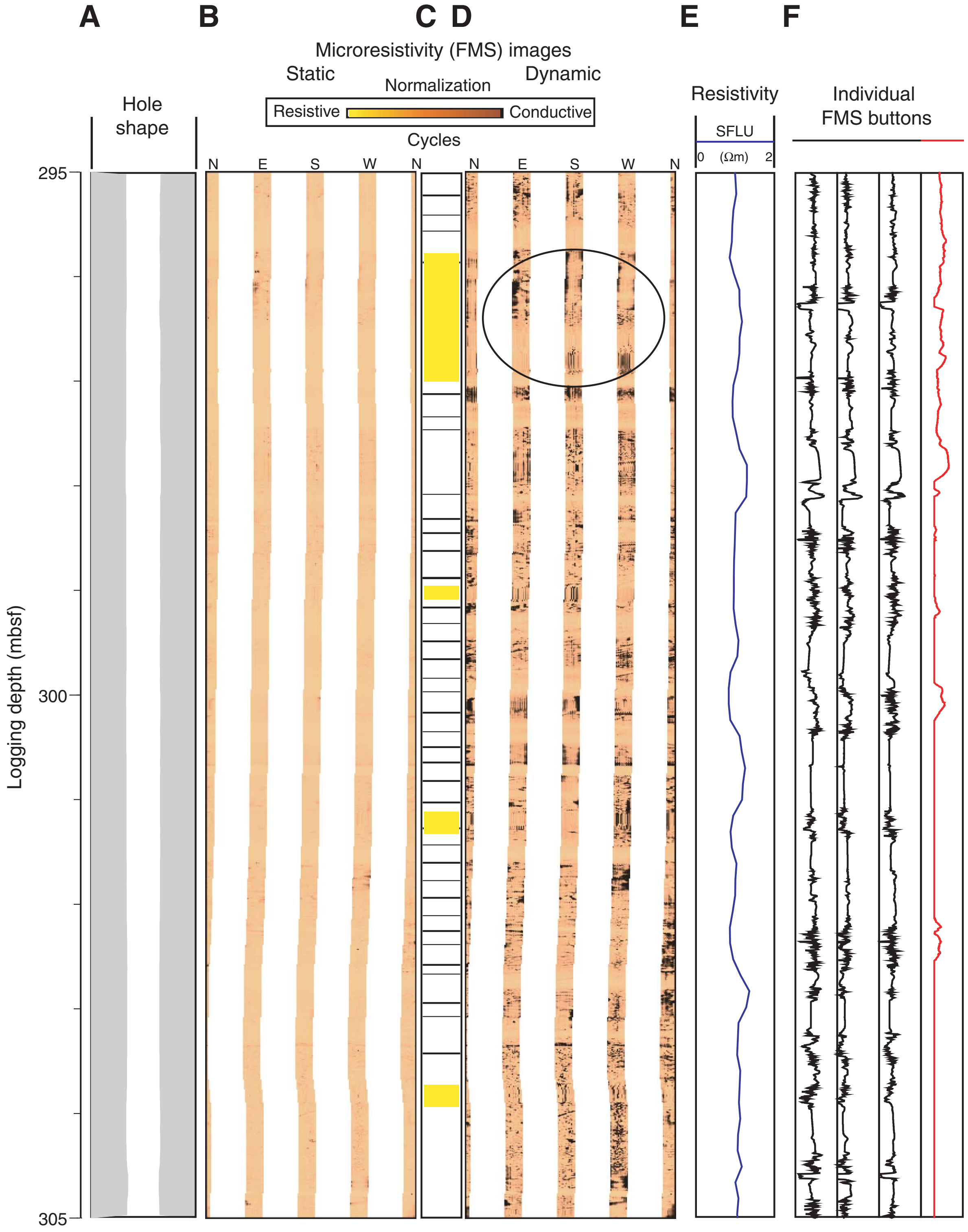

Figure F45. Seismic modeling inputs. **A.** Core bulk density (MAD method) vs. downhole density. **B.** *P*-wave velocity in cores vs. downhole. **C.** *P*-wave velocity in cores vs. core density (MAD method). **D.** *P*-wave velocity downhole vs. downhole density. **E.** *P*-wave velocity from cores vs. downhole density. **F.** *P*-wave velocity downhole vs. core density (MAD method). All data are referenced to the equivalent logging depth scale.

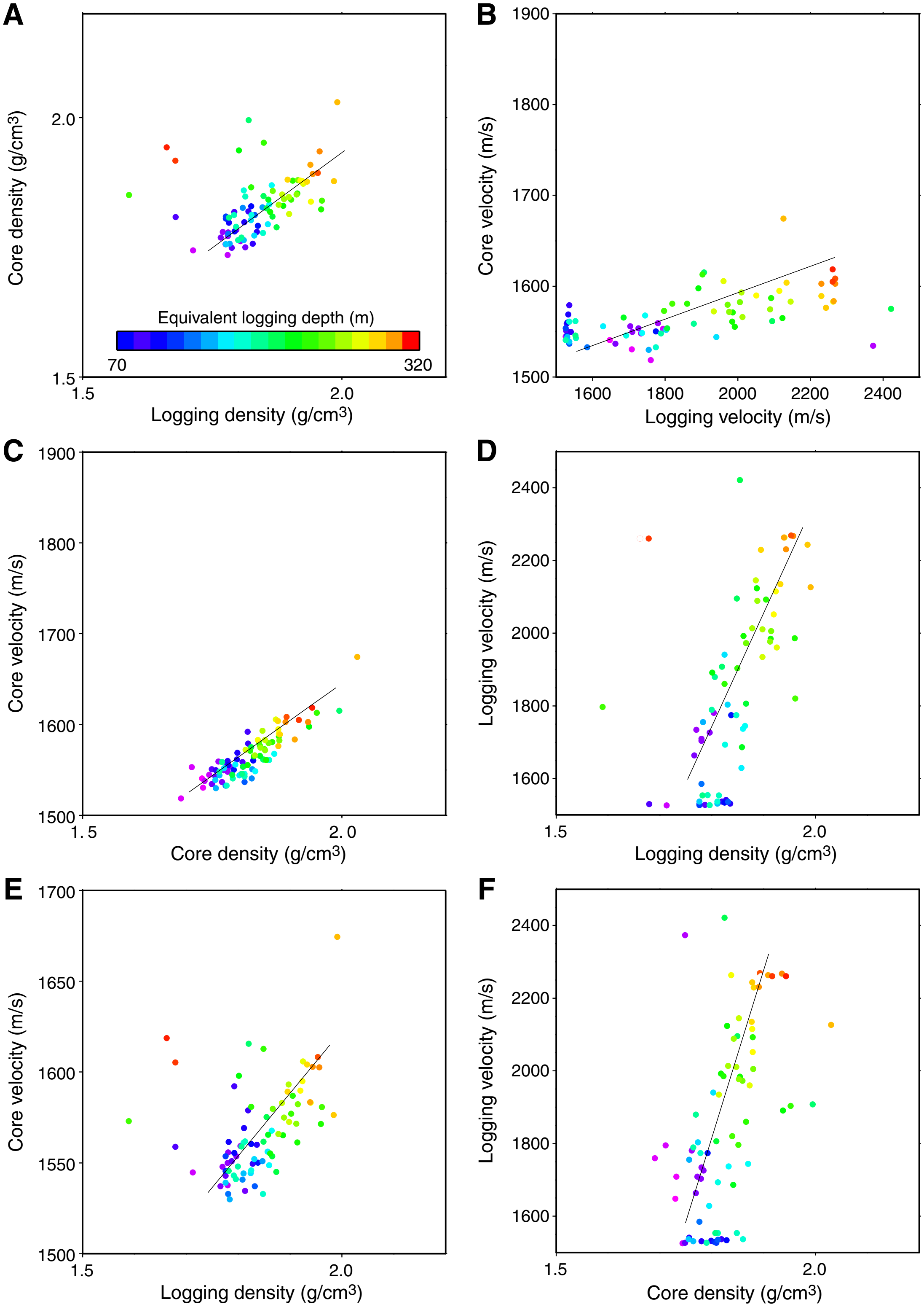

Figure F46. Sonic data showing (**A**) hole shape, (**B**) *P*-wave velocity in cores and downhole (V_P), (**C**) one-way traveltime (TT), (**D**) mean interval velocity, and (**E**) mean interval density.

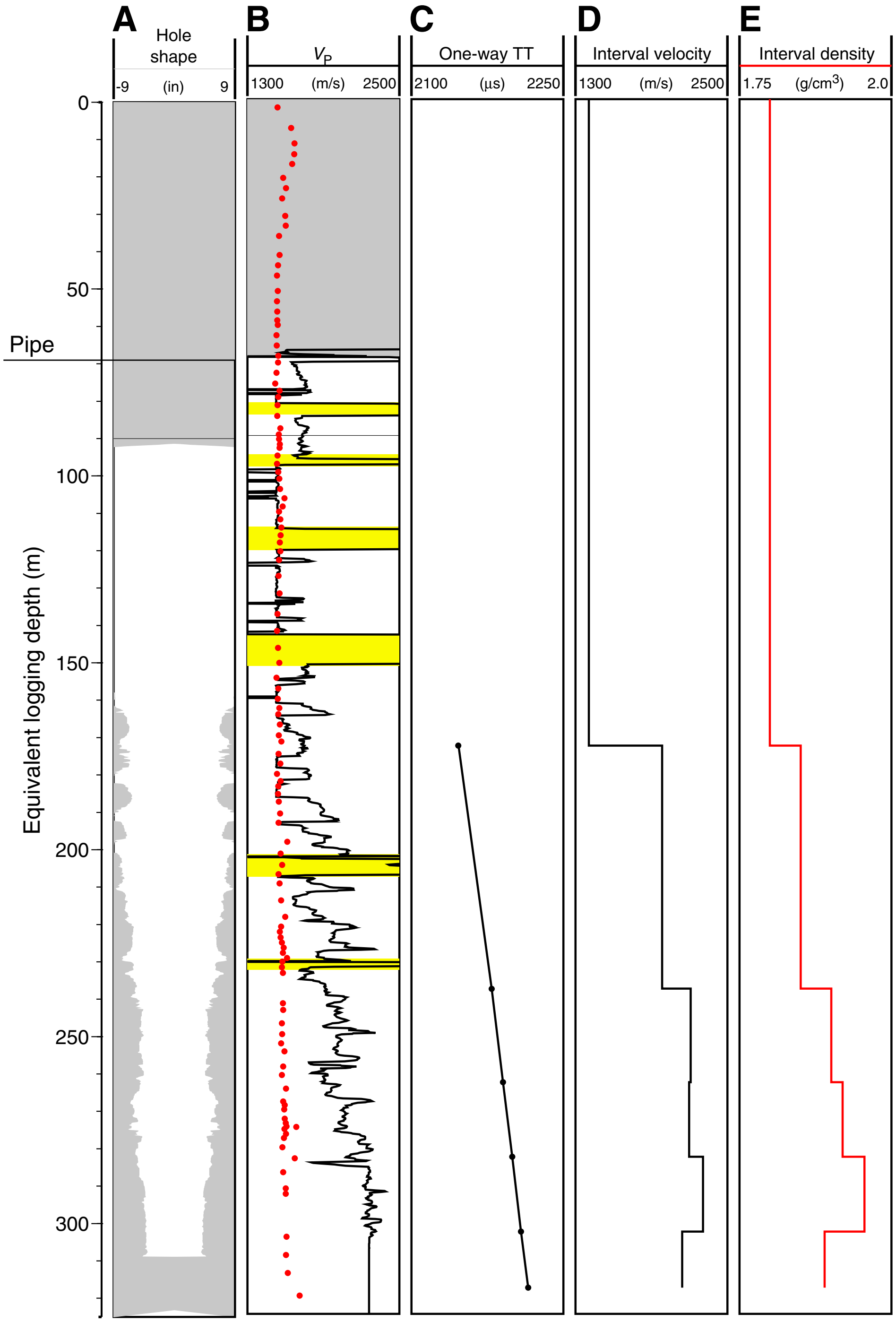

Figure F47. Stacked sonic waveforms. Examples of the problem encountered by the *P*-wave labeling algorithm in "slow" sediments where the formation velocity approaches those of the drilling mud (left and center) and good picking in a more consolidated formation (right). The black solid lines represent the results of the wave labeling algorithm.

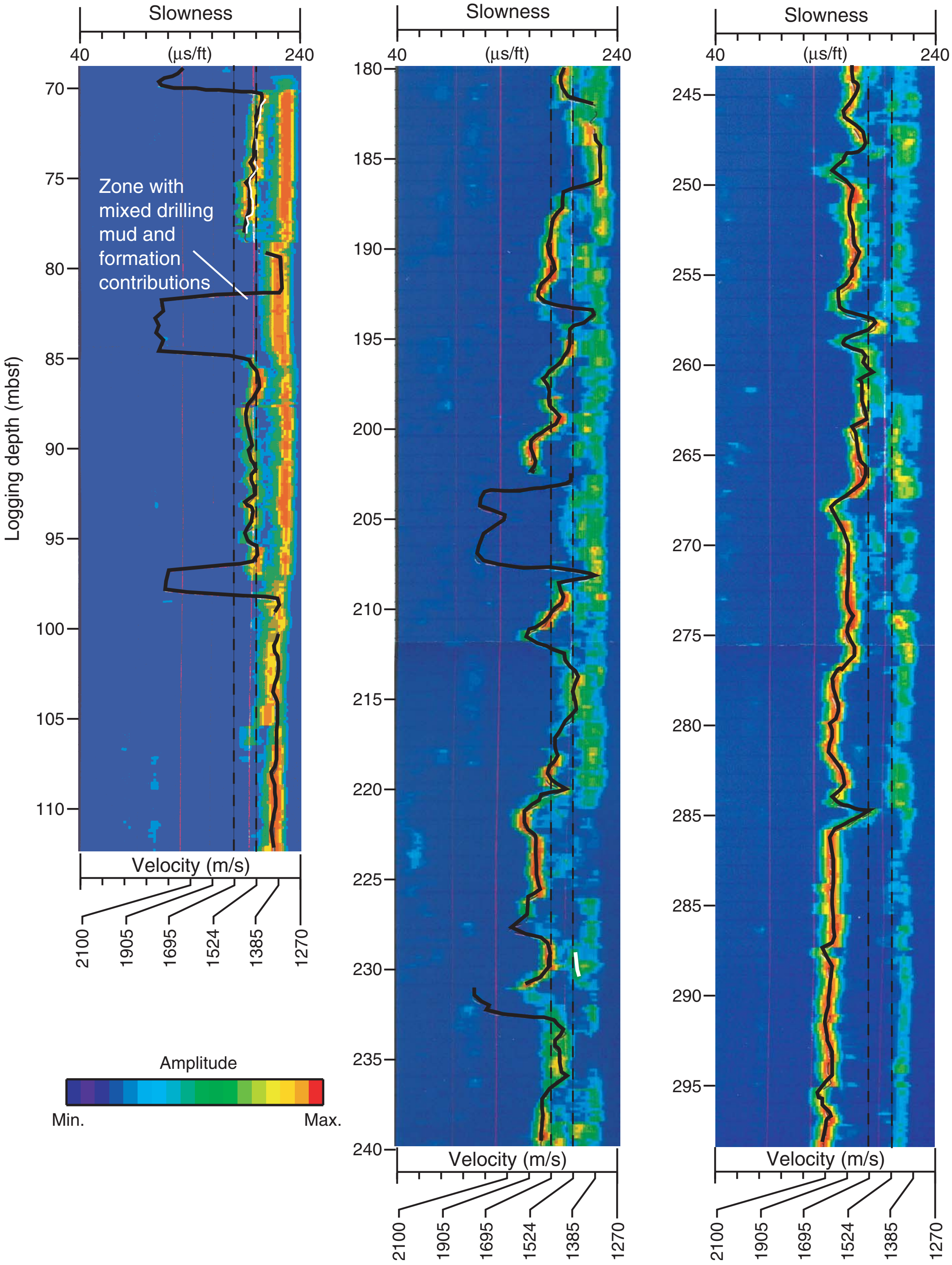

Figure F48. A. Core recovery plot. **B.** Shipboard biostratigraphic and magnetostratigraphic datums and the interpreted age-depth model. **C.** Corrected linear sedimentation rate (LSR), total, carbonate, and noncarbonate mass accumulation rates (MAR), calculated from the age model sampled at 1-m.y. intervals, and dry density and calcium carbonate concentrations averaged over the same 1-m.y. intervals. T = top, B = bottom.

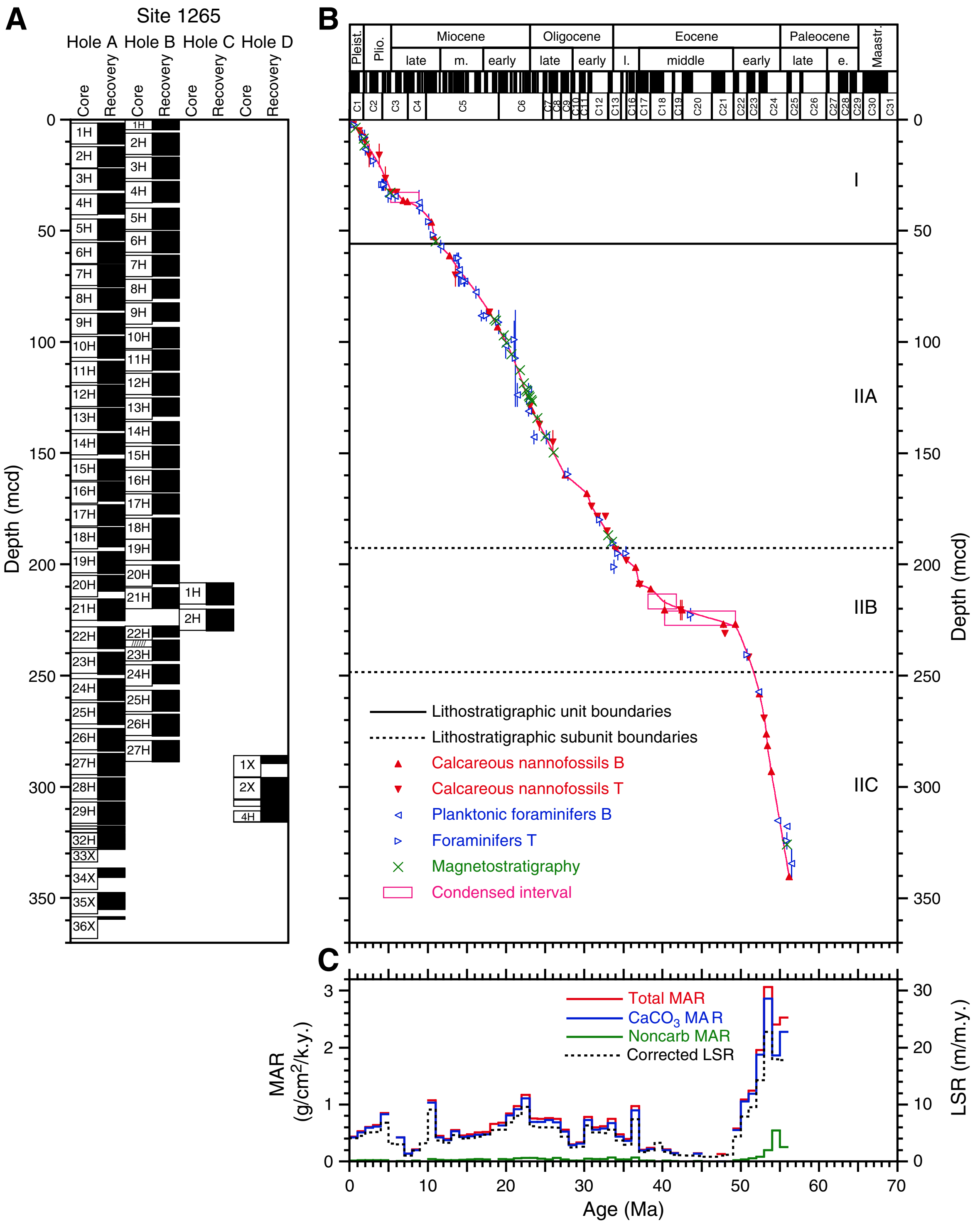

Table T1. Coring summary, Site 1265. (**See table notes.** Continued on next page.)

Core	Date (Apr 2003)	Local time (hr)	Depth (mbsf)		Length (m)		Recovery (%)	Tool deployment
			Top	Bottom	Cored	Recovered		
208-1265A-								
1H	9	20	0.0	9.5	9.5	9.56	100.6	
2H	9	115	9.5	19.0	9.5	9.08	95.6	NMCB
3H	9	210	19.0	28.5	9.5	9.63	101.4	Tensor
4H	9	310	28.5	38.0	9.5	9.16	96.4	APCT, Tensor
5H	9	405	38.0	47.5	9.5	9.67	101.8	Tensor
6H	9	450	47.5	57.0	9.5	9.44	99.4	Tensor, NMCB
7H	9	605	57.0	66.5	9.5	10.05	105.8	APCT, Tensor
8H	9	650	66.5	76.0	9.5	9.67	101.8	Tensor, NMCB
9H	9	740	76.0	85.5	9.5	9.34	98.3	Tensor
10H	9	850	85.5	95.0	9.5	9.80	103.2	APCT, Tensor
11H	9	940	95.0	104.5	9.5	9.91	104.3	Tensor
12H	9	1030	104.5	114.0	9.5	9.65	101.6	Tensor, NMCB
13H	9	1140	114.0	123.5	9.5	9.95	104.7	APCT, Tensor
14H	9	1235	123.5	133.0	9.5	9.13	96.1	Tensor, NMCB
15H	9	1315	133.0	142.5	9.5	9.64	101.5	Tensor
16H	9	1405	142.5	152.0	9.5	8.66	91.2	Tensor, NMCB
17H	9	1500	152.0	161.5	9.5	9.51	100.1	Tensor
18H	9	1550	161.5	171.0	9.5	8.62	90.7	Tensor, NMCB
19H	9	1640	171.0	180.5	9.5	9.82	103.4	Tensor
20H	9	1740	180.5	190.0	9.5	7.03	74.0	Tensor, NMCB
21H	9	1830	190.0	199.5	9.5	9.83	103.5	Tensor
22H	9	1915	199.5	209.0	9.5	9.89	104.1	Tensor, NMCB
23H	9	2010	209.0	218.5	9.5	9.96	104.8	Tensor
24H	9	2110	218.5	228.0	9.5	9.73	102.4	DO, Tensor, NMCB
25H	9	2210	228.0	237.5	9.5	9.83	103.5	Tensor
26H	9	2315	237.5	247.0	9.5	10.16	107.0	DO, Tensor
27H	10	55	247.0	256.5	9.5	10.02	105.5	DO, Tensor
28H	10	150	256.5	266.0	9.5	10.01	105.4	Tensor
29H	10	255	266.0	275.5	9.5	10.21	107.5	DO, Tensor
30H	10	350	275.5	276.7	1.2	1.23	102.5	Tensor
31H	10	505	276.7	278.2	1.5	1.56	104.0	Tensor
32H	10	640	278.2	285.6	7.4	7.41	100.1	Tensor
33X	10	810	285.6	292.1	6.5	0.00	0.0	
34X	10	935	292.1	301.7	9.6	4.16	43.3	
35X	10	1055	301.7	311.3	9.6	7.61	79.3	
36X	10	1210	311.3	321.0	9.7	1.11	11.4	
				Cored totals:	321.0	300.04	93.5	
208-1265B-								
1H	11	1310	0	4.7	4.7	4.78	101.7	APCT
2H	11	1410	4.7	14.2	9.5	9.98	105.1	
3H	11	1455	14.2	23.7	9.5	9.78	103.0	NMCB
4H	11	1545	23.7	33.2	9.5	9.33	98.2	Tensor
5H	11	1640	33.2	42.7	9.5	9.70	102.1	Tensor, NMCB
6H	11	1740	42.7	52.2	9.5	9.72	102.3	Tensor
7H	11	1835	52.2	61.7	9.5	9.36	98.5	Tensor, NMCB
8H	11	1925	61.7	71.2	9.5	8.48	89.3	Tensor
9H	11	2020	71.2	80.7	9.5	8.31	87.5	Tensor, NMCB
10H	11	2115	80.7	90.2	9.5	9.24	97.3	Tensor
11H	11	2200	90.2	99.7	9.5	9.14	96.2	Tensor, NMCB
12H	11	2250	99.7	109.2	9.5	9.98	105.1	Tensor
13H	11	2350	109.2	118.7	9.5	8.15	85.8	Tensor, NMCB
14H	12	40	118.7	128.2	9.5	9.96	104.8	Tensor
15H	12	135	128.2	137.7	9.5	9.77	102.8	Tensor, NMCB
16H	12	230	137.7	147.2	9.5	9.74	102.5	Tensor
17H	12	325	147.2	156.7	9.5	9.05	95.3	Tensor, NMCB
18H	12	415	156.7	166.2	9.5	9.71	102.2	Tensor
19H	12	500	166.2	175.7	9.5	9.55	100.5	Tensor, NMCB
20H	12	550	175.7	185.2	9.5	8.40	88.4	Tensor
21H	12	640	185.2	194.7	9.5	9.40	99.0	Tensor, NMCB
22H	12	730	194.7	204.2	9.5	5.04	53.1	Tensor
23H	12	840	204.2	213.7	9.5	9.36	98.5	Tensor, NMCB
24H	12	930	213.7	223.2	9.5	8.60	90.5	Tensor
25H	12	1025	223.2	232.7	9.5	9.47	99.7	Tensor
26H	12	1110	232.7	242.2	9.5	9.76	102.7	Tensor
27H	13	430	242.2	251.7	9.5	9.67	101.8	Tensor
				Cored totals:	251.7	243.43	96.7	

Table T1 (continued).

Core	Date (Apr 2003)	Local time (hr)	Depth (mbsf)		Length (m)		Recovery (%)	Tool deployment
			Top	Bottom	Cored	Recovered		
208-1265C-								
			*****Drilled from 0.0 to 185.0 mbsf*****					
1H	13	1840	185.0	194.5	9.5	9.89	104.1	Tensor
2H	14	915	194.5	204.0	9.5	9.78	103.0	DO, Tensor
			Cored totals:		19	19.67	103.5	
208-1265D-								
			*****Drilled from 0.0 to 248.0 mbsf*****					
1X	14	2255	248.0	257.6	9.6	3.59	37.4	
2X	14	2355	257.6	267.2	9.6	9.78	101.9	
3X	15	50	267.2	270.0	2.8	5.42	193.6	
4H	15	220	270.0	274.8	4.8	4.89	101.9	DO
5H	15	320	274.8	274.9	0.1	0.10	100.0	
			Cored totals:		26.9	23.78	88.4	
			Totals:		618.6	586.92	94.9	

Notes: NMCB = nonmagnetic core barrel, including cutting shoe (made from Monel). Tensor = brand name for core barrel orientation tool. APCT = Advanced Piston Corer Temperature tool (stainless steel housing is cutting shoe). DO = drillover. See Table **T1**, p. 106, in the “Leg 208 Summary” chapter.

Table T2. Composite depth scale, Site 1265.

Core	Offset (m)	Depth	
		(mbsf)	(mcd)
208-1265A-			
1H	1.62	0.00	1.62
2H	2.73	9.50	12.23
3H	3.30	19.00	22.30
4H	4.90	28.50	33.40
5H	6.70	38.00	44.70
6H	7.85	47.50	55.35
7H	8.18	57.00	65.18
8H	9.62	66.50	76.12
9H	11.12	76.00	87.12
10H	12.07	85.50	97.57
11H	13.77	95.00	108.77
12H	14.96	104.50	119.46
13H	15.90	114.00	129.90
14H	17.80	123.50	141.30
15H	19.75	133.00	152.75
16H	20.43	142.50	162.93
17H	21.23	152.00	173.23
18H	22.00	161.50	183.50
19H	23.31	171.00	194.31
20H	24.52	180.50	205.02
21H	25.65	190.00	215.65
22H	28.58	199.50	228.08
23H	30.48	209.00	239.48
24H	32.96	218.50	251.46
25H	34.19	228.00	262.19
26H	36.35	237.50	273.85
27H	38.03	247.00	285.03
28H	39.45	256.50	295.95
29H	40.78	266.00	306.78
30H	42.11	275.50	317.61
31H	42.28	276.70	318.98
32H	42.49	278.20	320.69
33X	43.52	285.60	329.12
34X	44.43	292.10	336.53
35X	45.78	301.70	347.48
36X	47.12	311.30	358.42
208-1265B-			
1H	0.00	0.00	0.00
2H	1.45	4.70	6.15
3H	2.88	14.20	17.08
4H	4.27	23.70	27.97
5H	6.70	33.20	39.90
6H	7.57	42.70	50.27
7H	8.90	52.20	61.10
8H	10.20	61.70	71.90
9H	11.27	71.20	82.47
10H	12.87	80.70	93.57
11H	13.42	90.20	103.62
12H	14.45	99.70	114.15
13H	16.06	109.20	125.26
14H	17.17	118.70	135.87
15H	18.67	128.20	146.87
16H	20.11	137.70	157.81
17H	21.12	147.20	168.32
18H	22.53	156.70	179.23
19H	22.48	166.20	188.68
20H	24.59	175.70	200.29
21H	25.32	185.20	210.52
22H	32.98	194.70	227.68
23H	29.75	204.20	233.95
24H	31.44	213.70	245.14
25H	33.45	223.20	256.65
26H	34.69	232.70	267.39
27H	36.96	242.20	279.16
208-1265C-			
1H	23.36	185.00	208.36
2H	25.65	194.50	220.15
208-1265D-			
1X	37.90	248.00	285.90
2X	38.27	257.60	295.87
3X	38.69	267.20	305.89
4H	40.83	270.00	310.83
5H	40.98	274.80	315.78

Table T3. Splice tie points, Site 1265.

Hole, core, section, interval (cm)	Depth			Hole, core, section, interval (cm)	Depth	
	(mbsf)	(mcd)			(mbsf)	(mcd)
208-				208-		
1265B-1H-4, 5.0	3.88	3.88	Tie to	1265A-1H-2, 76.0	2.26	3.88
1265A-1H-6, 87.5	8.38	10.00	Tie to	1265B-2H-3, 85.0	8.55	10.00
1265B-2H-5, 130.0	12.00	13.45	Tie to	1265A-2H-1, 121.0	10.72	13.45
1265A-2H-6, 55.0	17.55	20.28	Tie to	1265B-3H-3, 20.0	17.40	20.28
1265B-3H-6, 127.5	22.98	25.86	Tie to	1265A-3H-3, 54.5	22.56	25.86
1265A-3H-6, 30.0	26.80	30.10	Tie to	1265B-4H-2, 62.5	25.83	30.10
1265B-4H-6, 45.0	31.65	35.92	Tie to	1265A-4H-2, 102.5	31.02	35.92
1265A-4H-6, 35.0	36.20	41.10	Tie to	1265B-5H-1, 120.0	34.40	41.10
1265B-5H-5, 35.0	39.55	46.25	Tie to	1265A-5H-2, 5.0	39.55	46.25
1265A-5H-6, 142.5	46.92	53.62	Tie to	1265B-6H-3, 35.0	46.05	53.62
1265B-6H-6, 62.5	50.83	58.40	Tie to	1265A-6H-3, 5.0	50.55	58.40
1265A-6H-6, 17.5	55.17	63.02	Tie to	1265B-7H-2, 42.5	54.12	63.02
1265B-7H-5, 117.5	59.38	68.28	Tie to	1265A-7H-3, 10.0	60.10	68.28
1265A-7H-7, 2.5	66.03	74.21	Tie to	1265B-8H-2, 79.5	64.01	74.21
1265B-8H-4, 35.0	66.55	76.75	Tie to	1265A-8H-1, 62.0	67.13	76.75
1265A-8H-7, 5.0	75.25	84.87	Tie to	1265B-9H-2, 90.0	73.60	84.87
1265B-9H-5, 65.0	77.85	89.12	Tie to	1265A-9H-2, 50.0	78.00	89.12
1265A-9H-6, 5.0	83.55	94.67	Tie to	1265B-10H-1, 110.0	81.80	94.67
1265B-10H-4, 80.0	86.00	98.87	Tie to	1265A-10H-1, 130.0	86.80	98.87
1265A-10H-6, 145.0	94.45	106.52	Tie to	1265B-11H-2, 140.0	93.10	106.52
1265B-11H-4, 110.0	95.80	109.22	Tie to	1265A-11H-1, 45.0	95.45	109.22
1265A-11H-6, 135.0	103.85	117.62	Tie to	1265B-12H-3, 46.0	103.17	117.62
1265B-12H-6, 42.5	107.60	122.05	Tie to	1265A-12H-2, 108.5	107.09	122.05
1265A-12H-5, 97.5	111.48	126.44	Tie to	1265B-13H-1, 117.5	110.38	126.44
1265B-13H-5, 112.5	116.32	132.38	Tie to	1265A-13H-2, 97.5	116.48	132.38
1265A-13H-5, 67.5	120.68	136.58	Tie to	1265B-14H-1, 71.0	119.41	136.58
1265B-14H-5, 125.0	125.95	143.12	Tie to	1265A-14H-2, 32.5	125.32	143.12
1265A-14H-6, 7.5	131.08	148.88	Tie to	1265B-15H-2, 51.0	130.21	148.88
1265B-15H-5, 112.5	135.32	153.99	Tie to	1265A-15H-1, 123.5	134.24	153.99
1265A-15H-4, 130.0	138.80	158.55	Tie to	1265B-16H-1, 73.5	138.44	158.55
1265B-16H-4, 102.5	143.22	163.33	Tie to	1265A-16H-1, 40.0	142.90	163.33
1265A-16H-4, 132.5	148.32	168.75	Tie to	1265B-17H-1, 42.0	147.63	168.75
1265B-17H-6, 120.0	155.90	177.02	Tie to	1265A-17H-3, 78.5	155.79	177.02
1265A-17H-5, 115.0	159.15	180.38	Tie to	1265B-18H-1, 115.0	157.85	180.38
1265B-18H-6, 55.0	164.75	187.28	Tie to	1265A-18H-3, 77.5	165.28	187.28
1265A-18H-5, 65.0	168.15	190.15	Tie to	1265B-19H-1, 147.0	167.67	190.15
1265B-19H-6, 75.0	174.45	196.93	Tie to	1265A-19H-2, 112.5	173.62	196.93
1265A-19H-7, 20.0	180.20	203.51	Tie to	1265B-20H-3, 22.5	178.92	203.51
1265B-20H-4, 65.0	180.85	205.44	Tie to	1265A-20H-1, 42.5	180.92	205.44
1265A-20H-5, 5.0	186.55	211.07	Tie to	1265B-21H-1, 55.0	185.75	211.07
1265B-21H-5, 77.5	191.98	217.30	Tie to	1265A-21H-2, 13.0	191.65	217.30
1265A-21H-4, 95.0	195.45	221.10	Tie to	1265C-2H-1, 95.0	195.45	221.10
1265C-2H-7, 37.5	203.38	229.03	Tie to	1265A-22H-1, 95.0	200.45	229.03
1265A-22H-5, 35.0	205.85	234.43	Tie to	1265B-23H-1, 47.0	204.68	234.43
1265B-23H-5, 87.5	211.08	240.83	Tie to	1265A-23H-1, 135.0	210.35	240.83
1265A-23H-5, 77.5	215.78	246.26	Tie to	1265B-24H-1, 112.5	214.82	246.26
1265B-24H-6, 60.0	221.80	253.24	Tie to	1265A-24H-2, 27.0	220.28	253.24
1265A-24H-5, 47.5	224.98	257.94	Tie to	1265B-25H-1, 145.0	224.49	257.94
1265B-25H-7, 62.5	232.16	265.61	Tie to	1265A-25H-3, 42.5	231.42	265.61
1265A-25H-5, 125.0	235.25	269.44	Tie to	1265B-26H-2, 55.0	234.75	269.44
1265B-26H-6, 122.5	241.42	276.11	Tie to	1265A-26H-2, 74.5	239.76	276.11
1265A-26H-6, 7.5	245.08	281.43	Tie to	1265B-27H-2, 76.0	244.47	281.43
1265B-27H-6, 105.0	250.75	287.71	Tie to	1265A-27H-2, 117.5	249.68	287.71
1265A-27H-C, 10.0	256.95	294.98	Append to	1265A-28H-1, 0.0	256.50	295.95
1265A-28H-C, 15.0	266.44	305.89	Append to	1265A-29H-1, 0.0	266.00	306.78
1265A-29H-C, 22.5	276.11	316.89	Append to	1265A-30H-1, 0.0	275.50	317.61
1265A-30H-C, 12.5	276.65	318.76	Append to	1265A-31H-1, 0.0	276.70	318.98
1265A-31H-C, 27.5	278.17	320.45	Append to	1265A-32H-1, 0.0	278.20	320.69
1265A-32H-C, 15.0	285.55	328.04	Append to	1265A-34X-1, 0.0	292.10	336.53
1265A-34X-3, 70.0	295.80	340.23	Append to	1265A-35X-1, 0.0	301.70	347.48
1265A-35X-C, 25.0	309.21	354.99	Append to	1265A-36X-1, 0.0	311.30	358.42
1265A-36X-C, 30.0	312.31	359.43				

Note: This table is also available in ASCII.

Table T4. Lithostratigraphic subdivisions, Site 1265.

Subunit	Unit boundary depth (mcd)	Hole 1265A						Hole 1265B						Hole 1265C					
		Core, section, interval (cm)		Depth (mbsf)		Depth (mcd)		Core, section, interval (cm)		Depth (mbsf)		Depth (mcd)		Core, section, interval (cm)		Depth (mbsf)		Depth (mcd)	
		Top	Base	Top	Base	Top	Base	Top	Base	Top	Base	Top	Base	Top	Base	Top	Base	Top	Base
I		1H-1, 0	6H-1, 50	0.0	48.0	1.6	55.9	**1H-1, 0**	**6H-4, 108**	**0.0**	**48.3**	**0.0**	**55.9**	—	—	—	—	—	—
	55.85																		
IIA		**6H-1, 50**	**18H-7, 0**	**48.0**	**169.0**	**55.9**	**191.0**	**6H-4, 108**	**19H-3, 105**	**48.3**	**170.3**	**55.9**	**192.7**	—	—	—	—	—	—
	192.73																		
IIB		**18H-7, 0**	**23H-7, 23**	**169.0**	**218.2**	**191.0**	**248.7**	**19H-3, 105**	**24H-3, 36**	**170.3**	**217.1**	**192.7**	**248.5**	1H-1, 0	2H-CC, 32	185.0	204.3	208.4	229.9
	248.50																		
IIC		**23H-7, 23**	**36X-CC**	**218.2**	**312.4**	**248.7**	**359.5**	24H-3, 36	27H-CC, 10	217.1	251.9	248.5	288.8	—	—	—	—	—	—
	359.13																		

Notes: Bold data define unit boundaries; other values indicate recovered interval closest to unit boundary. — = lithostratigraphic unit not recovered.

Subunit	Unit boundary depth (mcd)	Hole 1265D						Description
		Core, section, interval (cm)		Depth (mbsf)		Depth (mcd)		
		Top	Base	Top	Base	Top	Base	
I		—	—	—	—	—	—	Foraminifer-bearing nannofossil ooze and nannofossil ooze
	55.85							
IIA		—	—	—	—	—	—	Nannofossil ooze and foraminifer-bearing nannofossil ooze
	192.73							
IIB		—	—	—	—	—	—	Nannofossil ooze and foraminifer-bearing nannofossil ooze
	248.50							
IIC		1X-1, 0	5X-CC, 10	248.0	274.9	285.9	315.9	Nannofossil ooze and foraminifer-bearing nannofossil ooze
	359.13							

Table T5. Stratigraphic positions of selected calcareous nannofossil datums, Site 1265. (**See table note.** Continued on next page.)

				Top of sample interval			Base of sample interval		
		Age (Ma)		Core, section, interval (cm)	Depth		Core, section, interval (cm)	Depth	
	Datum	Youngest	Oldest		(mbsf)	(mcd)		(mbsf)	(mcd)
				208-1265A-			208-1265A-		
T	*Pseudoemiliania lacunosa*	0.46	0.46	1H-1, 20	0.20	1.82	1H-1, 120	1.20	2.82
T	Large *Gephyrocapsa* spp.	1.22	1.22	1H-2, 120	2.70	4.32	1H-3, 120	4.20	5.82
B	Large *Gephyrocapsa* spp.	1.58	1.58	1H-3, 120	4.20	5.82	1H-4, 120	5.70	7.32
T	*Calcidiscus macintyrei*	1.67	1.67	1H-4, 120	5.70	7.32	1H-5, 120	7.20	8.82
B	Medium *Gephyrocapsa* spp.	1.69	1.69	1H-4, 120	5.70	7.32	1H-5, 120	7.20	8.82
T	*Discoaster brouweri* and *D. triradiatus*	1.95	1.97	1H-5, 120	7.20	8.82	1H-6, 120	8.70	10.32
T	*Discoaster pentaradiatus*	2.52	2.52	1H-CC	9.46	11.08	2H-CC	18.53	21.26
T	*Reticulofenestra pseudoumbilicus*	3.82	3.82	1H-CC	9.46	11.08	2H-CC	18.53	21.26
T	*Amaurolithus* spp.	4.56	4.56	2H-CC	18.53	21.26	3H-CC	28.58	31.88
T	*Nicklithus amplificus*	6.00	6.00	3H-CC	28.58	31.88	4H-1, 15	28.65	33.55
B	*Nicklithus amplificus*	6.84	6.84	4H-3, 2	31.37	36.27	4H-3, 50	31.85	36.75
B	*Amaurolithus primus*	7.39	7.39	4H-3, 50	31.85	36.75	4H-3, 100	32.35	37.25
B	*Discoaster bellus* gr. (*D. hamatus*)	10.48	10.48	5H-1, 110	39.10	45.80	5H-2, 40	39.90	46.60
B	*Catinaster coalitus*	10.79	10.79	5H-5, 40	44.40	51.10	5H-7, 50	47.50	54.20
B	*Triquetrorhabdulus rugosus*	12.81	12.81	6H-4, 110	53.10	60.95	6H-5, 15	53.65	61.50
T	*Sphenolithus heteromorphus*	13.55	13.55	6H-CC	56.89	64.74	7H-CC	66.83	75.01
B	*Sphenolithus heteromorphus*	17.76	17.76	8H-CC	76.12	85.74	9H-1, 40	76.40	87.52
T	*Sphenolithus belemnos*	17.89	17.89	8H-CC	76.12	85.74	9H-1, 40	76.40	87.52
B	*Sphenolithus belemnos*	18.92	18.92	9H-4, 120	81.70	92.82	9H-5, 40	82.40	93.52
T	*Sphenolithus delphix*	23.07	23.07	12H-7, 70	113.90	128.86	12H-CC	114.10	129.06
B	*Sphenolithus delphix*	23.33	23.33	13H-1, 70	114.70	130.60	13H-1, 100	115.00	130.90
T	*Sphenolithus ciperoensis*	24.23	24.23	13H-3, 130	118.30	134.20	13H-CC	123.90	139.80
T	*Sphenolithus distentus*	25.98	25.98	13H-CC	123.90	139.80	14H-CC	132.58	150.38
B	*Sphenolithus ciperoensis*	27.55	27.55	15H-5, 70	139.70	159.45	15H-5, 137	140.37	160.12
B	*Sphenolithus distentus*	30.32	30.32	16H-4, 30	147.30	167.73	16H-4, 100	148.00	168.43
T	*Sphenolithus pseudoradians*			17H-1, 30	152.30	173.53	17H-1, 110	153.10	174.33
T	*Reticulofenestra umbilicus* >14 µm	31.7	31.7	17H-4, 30	156.80	178.03	17H-4, 110	157.60	178.83
T	*Isthmolithus recurvus*	32.7	32.7	17H-4, 30	156.80	178.03	17H-4, 110	157.60	178.83
T	*Ericsonia formosa*	32.9	32.9	18H-1, 110	162.60	184.60	18H-2, 30	163.30	185.30
T	*Discoaster saipanensis*	34.0	34.0	18H-CC	170.02	192.02	19H-1, 30	171.30	194.61
T	*Calcidiscus protoannulus*	35.4	35.4	19H-3, 30	174.30	197.61	19H-3, 145	175.45	198.76
B	*Isthmolithus recurvus*	36.6	36.6	19H-5, 39	177.39	200.70	19H-5, 145	178.45	201.76
B	*Chiasmolithus oamaruensis*	37.0	37.0	20H-3, 20	183.70	208.22	20H-3, 60	184.10	208.62
T	*Chiasmolithus grandis*	37.1	37.1	20H-3, 60	184.10	208.62	20H-3, 140	184.90	209.42
B	*Dictyococcites bisectus*	38.5	38.5	20H-4, 140	186.40	210.92	20H-5, 20	186.70	211.22
B	*Dictyococcites scrippsae*	40.3	40.3	20H-CC	187.43	211.95	21H-1, 40	190.40	216.05
T	*Nannotetrina* spp.	42.3	42.3	20H-CC	187.43	211.95	21H-1, 40	190.40	216.05
B	*Reticulofenestra umbilicus* >14 µm	42.5	42.5	21H-1, 40	190.40	216.05	21H-7, 30	199.30	224.95
B	*Nannotetrina* spp.	47.8	47.8	21H-CC	199.78	225.43	22H-1, 40	199.90	228.48
B	*Discoaster sublodoensis*	49.3	49.3	21H-CC	199.78	225.43	22H-1, 40	199.90	228.48
T	*Discoaster lodoensis*	48.0	48.0	22H-2, 110	202.10	230.68	22H-3, 40	202.90	231.48
T	*Tribrachiatus orthostylus*	51.0	51.0	23H-2, 40	210.90	241.38	23H-2, 110	211.60	242.08
B	*Discoaster lodoensis*	52.4	52.4	24H-5, 40	224.90	257.86	24H-5, 110	225.60	258.56
T	*Discoaster multiradiatus*	53.0	53.0	25H-5, 45	234.45	268.64	25H-5, 140	235.40	269.59
B	*Sphenolithus radians*	53.3	53.3	26H-2, 60	239.60	275.95	26H-2, 100	240.00	276.35
B	*Tribrachiatus orthostylus*	53.4	53.4	26H-5, 90	244.40	280.75	26H-6, 90	245.90	282.25
B	*Discoaster diastypus*	53.9	53.9	27H-5, 25	253.25	291.28	27H-CC	256.97	295.00
T	*Fasciculithus* spp.			29H-3, 140	269.78	310.56	29H-4, 20	270.08	310.86
	Increase *Zygrhablithus bijugatus*			29H-6, 100	273.88	314.66	29H-7, 15	274.53	315.31
B	*Rhomboaster* spp.			29H-7, 50	274.88	315.66	29H-7, 68	275.06	315.84
B	*Discoaster multiradiatus*	56.2	56.2	34X-3, 70	295.80	340.23	34X-CC	296.21	340.64
				208-1265B-			208-1265B-		
T	*Pseudoemiliania lacunosa*	0.46	0.46	1H-1, 1	0.01	0.01	1H-CC	4.73	4.73
T	*Discoaster brouweri* and *D. triradiatus*	1.95	1.95	1H-CC	4.73	4.73	2H-CC	14.63	16.08
T	*Reticulofenestra pseudoumbilicus*	3.82	3.82	2H-CC	14.63	16.08	3H-CC	23.93	26.81
T	*Amaurolithus* spp.	4.56	4.56	2H-CC	14.63	16.08	3H-CC	23.93	26.81
T	*Nicklithus amplificus*	6.00	6.00	3H-CC	23.93	26.81	4H-CC	32.98	37.25
B	*Amaurolithus primus*	7.39	7.39	3H-CC	23.93	26.81	4H-CC	32.98	37.25
B	*Discoaster bellus* gr. (*D.hamatus*)	10.48	10.48	4H-CC	32.98	37.25	5H-CC	42.85	49.55
B	*Catinaster coalitus*	10.79	10.79	5H-CC	42.85	49.55	6H-CC	52.37	59.94
B	*Triquetrorhabdulus rugosus*	12.81	12.81	5H-CC	42.85	49.55	6H-CC	52.37	59.94
T	*Sphenolithus heteromorphus*	13.55	13.55	6H-CC	52.37	59.94	7H-2, 44	54.14	63.04
B	*Sphenolithus heteromorphus*	17.76	17.76	8H-CC	70.13	80.33	9H-CC	79.46	90.73
T	*Sphenolithus belemnos*	17.89	17.89	8H-CC	70.13	80.33	9H-CC	79.46	90.73
B	*Sphenolithus belemnos*	18.92	18.92	9H-CC	79.46	90.73	10H-CC	89.89	102.76

Table T5 (continued).

		Age (Ma)		Top of sample interval			Base of sample interval		
				Core, section, interval (cm)	Depth		Core, section, interval (cm)	Depth	
	Datum	Youngest	Oldest		(mbsf)	(mcd)		(mbsf)	(mcd)
B	*Sphenolithus disbelemnos*	22.67	22.67	11H-CC	99.29	112.71	12H-7, 84	109.51	123.96
T	*Sphenolithus delphix*	23.07	23.07	13H-3, 80	113.00	129.06	13H-3, 120	113.40	129.46
B	*Sphenolithus delphix*	23.33	23.33	13H-4, 30	114.00	130.06	13H-4, 90	114.60	130.66
T	*Sphenolithus ciperoensis*	24.23	24.23	13H-CC	117.30	133.36	14H-CC	128.61	145.78
T	*Sphenolithus distentus*	25.98	25.98	13H-CC	117.30	133.36	14H-CC	128.61	145.78
B	*Sphenolithus ciperoensis*	27.55	27.55	14H-CC	128.61	145.78	15H-CC	137.92	156.59
B	*Sphenolithus distentus*	30.32	30.32	16H-CC	147.39	167.50	17H-CC	156.20	177.32
T	*Sphenolithus pseudoradians*			16H-CC	147.39	167.50	17H-CC	156.20	177.32
T	*Reticulofenestra umbilicus* >14 µm	31.7	31.7	17H-CC	156.20	177.32	18H-CC	166.27	188.80
T	*Ericsonia formosa*	32.9	32.9	17H-CC	156.20	177.32	18H-CC	166.27	188.80
T	*Isthmolithus recurvus*	32.7	32.7	19H-1, 60	166.80	189.28	19H-3, 100	170.20	192.68
T	*Discoaster saipanensis*	34.0	34.0	19H-3, 110	170.30	192.78	19H-5, 130	173.50	195.98
T	*Chiasmolithus grandis*	37.1	37.1	20H-CC	184.00	208.59	21H-CC	194.50	219.82
B	*Dictyococcites bisectus*	38.5	38.5	20H-CC	184.00	208.59	21H-CC	194.50	219.82
B	*Dictyococcites scrippsae*	40.3	40.3	20H-CC	184.00	208.59	21H-CC	194.50	219.82
T	*Nannotetrina* spp.	42.3	42.3	20H-CC	184.00	208.59	21H-CC	194.50	219.82
B	*Reticulofenestra umbilicus* >14 µm	42.5	42.5	20H-CC	184.00	208.59	21H-CC	194.50	219.82
B	*Nannotetrina* spp.	47.8	47.8	20H-CC	184.00	208.59	21H-CC	194.50	219.82
T	*Discoaster lodoensis*	48.0	48.0	21H-CC	194.50	219.82	22H-CC	199.64	232.62
B	*Discoaster sublodoensis*	49.3	49.3	22H-CC	199.64	232.62	23H-CC	213.46	243.21
T	*Tribrachiatus orthostylus*	51.0	51.0	22H-CC	199.64	232.62	23H-CC	213.46	243.21
B	*Discoaster lodoensis*	52.4	52.4	24H-CC	222.20	253.64	25H-1, 66	223.86	257.31
T	*Discoaster multiradiatus*	53.0	53.0	25H-CC	232.47	265.92	26H-CC	242.41	277.10
B	*Tribrachiatus orthostylus*	53.4	53.4	25H-CC	232.47	265.92	26H-CC	242.41	277.10
B	*Sphenolithus radians*	53.3	53.3	26H-CC	242.41	277.10	27H-CC	251.77	288.73
				208-1265D-			208-1265D-		
B	*Discoaster diastypus*	53.9	53.9	1X-CC	251.54	289.44	2X-CC	267.33	305.60
T	*Fasciculithus* spp.			2X-CC	267.33	305.60	3X-CC	272.57	311.26
	Increase *Zygrhablithus bijugatus*			3X-CC	272.57	311.26	4X-CC	274.88	315.71
B	*Rhomboaster* spp.			4X-CC	274.88	315.71	5X-CC	274.89	315.87

Note: T = top, B = bottom.

Table T6. Stratigraphic ranges and relative abundances of selected calcareous nannofossil taxa, Site 1265. (This table is available in an **oversized format.**)

Table T7. Stratigraphic positions of selected planktonic foraminiferal datums, Site 1265.

	Datum	Age (Ma)		Hole, core, section, interval (cm)	Depth		Hole, core, section, interval (cm)	Depth	
		Youngest	Oldest		(mbsf)	(mcd)		(mbsf)	(mcd)
				208-			208-		
T	*Globorotalia tosaensis*	0.61	0.61	1265B-1H-1, 0–2	0.00	0.00	1265B-1H-CC	4.73	4.73
T	*Globigerina apertura*	1.68	1.68	1265B-1H-CC	4.73	4.73	1265A-1H-CC	9.46	11.08
T	*Globigerinoides extremus*	1.91	1.91	1265B-1H-CC	4.73	4.73	1265A-1H-CC	9.46	11.08
B	*Globorotalia truncatulinoides*	2.03	2.03	1265A-1H-CC	9.46	11.08	1265B-2H-CC	14.63	16.08
T	*Dentoglobigerina altispira*	3.02	3.02	1265B-2H-CC	14.63	16.08	1265A-2H-CC	18.53	21.26
T	*Globorotalia plesiotumida*	4.15	4.15	1265B-3H-CC	23.93	26.81	1265A-3H-CC	28.58	31.88
T	*Hirsutella cibaoensis*	4.16	4.16	1265B-3H-CC	23.93	26.81	1265A-3H-CC	28.58	31.88
B	*Globorotalia crassaformis* s.l.	4.31	4.31	1265B-3H-CC	23.93	26.81	1265A-3H-CC	28.58	31.88
T	*Globoturborotalita nepenthes*	4.37	4.37	1265B-3H-CC	23.93	26.81	1265A-3H-CC	28.58	31.88
B	*Sphaeroidinella dehiscens* (s.l.)	4.94	4.94	1265A-3H-CC	28.58	31.88	1265B-4H-CC	32.98	37.25
B	*Globigerinoides conglobatus*	5.84	5.84	1265B-4H-CC	32.98	37.25	1265A-3H-CC	28.58	31.88
B	*Globorotalia plesiotumida*	8.91	8.91	1265A-3H-CC	28.58	31.88	1265A-4H-CC	37.61	42.51
B	*Globigerinoides extremus*	8.94	8.94	1265B-4H-CC	32.98	37.25	1265A-4H-CC	37.61	42.51
T	*Menardella praemenardii*	10.09	10.09	1265A-4H-CC	37.61	42.51	1265B-5H-CC	42.85	49.55
T	*Paragloborotalia mayeri*	10.70	10.70	1265B-5H-CC	42.85	49.55	1265A-5H-CC	47.62	54.32
B	*Globoturborotalita nepenthes*	11.64	11.64	1265A-5H-CC	47.62	54.32	1265B-6H-CC	52.37	59.94
T	*Hirsutella praescitula*	13.73	13.73	1265B-6H-CC	52.37	59.94	1265A-6H-CC	56.89	64.74
T	*Menardella archeomenardii*	13.92	13.92	1265B-6H-CC	52.37	59.94	1265A-6H-CC	56.89	64.74
T	*Fohsella peripheroronda*	13.92	13.92	1265B-6H-CC	52.37	59.94	1265A-6H-CC	56.89	64.74
B	*Menardella praemenardii*	13.95	13.95	1265A-6H-CC	56.89	64.74	1265A-7H-CC	66.83	75.01
B	*Fohsella peripheroacuta*	14.02	14.02	1265A-6H-CC	56.89	64.74	1265A-7H-CC	66.83	75.01
T	*Praeorbulina sicana*	14.63	14.63	1265B-7H-CC	61.51	70.41	1265A-7H-CC	66.83	75.01
B	*Orbulina suturalis*	14.70	14.70	1265B-7H-CC	61.51	70.41	1265A-7H-CC	66.83	75.01
B	*Orbulina* spp.	14.71	14.71	1265B-7H-CC	61.51	70.41	1265A-7H-CC	66.83	75.01
B	*Menardella archeomenardii*	16.16	16.16	1265A-7H-CC	66.83	75.01	1265B-8H-CC	70.13	80.33
B	*Praeorbulina sicanus*	16.86	16.86	1265A-8H-CC	76.12	85.74	1265B-9H-CC	79.46	90.73
T	*Catapsydrax dissimilis*	17.51	17.51	1265A-8H-CC	76.12	85.74	1265B-9H-CC	79.46	90.73
T	*Globoquadrina binaiensis*	19.08	19.08	1265A-8H-CC	76.12	85.74	1265A-9H-CC	85.29	96.41
B	*Globoquadrina binaiensis*	19.98	19.98	1265A-9H-CC	85.29	96.41	1265A-10H-CC	95.20	107.27
T	*Paragloborotalia kugleri*	21.03	21.03	1265A-10H-CC	95.20	107.27	1265B-11H-CC	99.29	112.71
T	*Paragloborotalia pseudokugleri*	21.22	21.22	1265A-8H-CC	76.12	85.74	1265A-9H-CC	79.46	90.73
B	*Globoquadrina dehiscens*	21.44	21.44	1265A-11H-CC	104.86	118.63	1265A-12H-CC	114.10	129.06
B	*Paragloborotalia kugleri*	22.87	22.87	1265A-12H-CC	114.10	129.06	1265B-13H-CC	117.30	133.36
B	*Globigerinoides trilobus* s.l.	22.87	22.87	1265A-11H-CC	104.86	118.63	1265B-12H-CC	109.63	124.08
T	*Globigerina euapertura*	23.03	23.03	1265B-12H-CC	109.63	124.08	1265A-12H-CC	114.10	129.06
B	*Globigerinoides primordius* (common)	23.54	23.54	1265A-13H-CC	123.90	139.80	1265B-14H-CC	128.61	145.78
B	*Paragloborotalia pseudokugleri*	25.15	25.15	1265A-13H-CC	123.90	139.80	1265B-14H-CC	128.61	145.78
T	*Chiloguembelina cubensis* (common)	27.92	27.92	1265B-15H-CC	137.92	156.59	1265A-15H-CC	142.59	162.34
T	*Pseudohastigerina* spp.	32.00	32.00	1265B-17H-CC	156.20	177.32	1265A-17H-CC	161.46	182.69
T	*Hantkenina* spp.	33.70	33.70	1265B-18H-CC	166.27	188.80	1265A-18H-CC	170.02	192.02
T	*Turborotalia cerroazulensis*	33.80	33.80	1265B-19H-CC	175.65	198.13	1265A-19H-CC	180.77	204.08
T	*Globigerinatheka index*	34.30	34.30	1265A-18H-CC	170.02	192.02	1265B-19H-CC	175.65	198.13
T	*Globigerinatheka semiinvoluta*	35.30	35.30	1265A-18H-CC	170.02	192.02	1265B-19H-CC	175.65	198.13
T	*Morozovella aragonensis*	43.60	43.60	1265B-21H-CC	194.50	219.82	1265A-21H-CC	199.78	225.43
T	*Morozovella formosa*	50.80	50.80	1265A-22H-CC	209.34	237.92	1265B-23H-CC	213.46	243.21
B	*Morozovella aragonensis*	52.30	52.30	1265B-25H-1, 66–67	223.86	257.31	1265B-25H-1, 78–79	223.98	257.43
B	*Igorina broedermanni*	54.70	54.70	1265A-29H-6, 148–149	274.36	315.14	1265A-29H-7, 8–9	274.46	315.24
T	*Stensioeina beccariiformis**	55.00	55.00	1265A-29H-7, 65–66	275.03	315.81	1265A-29H-7, 70–71	275.08	315.86
B	*Morozovella subbotinae*	55.90	55.90	1265A-29H-CC	276.16	316.94	1265A-30H-CC	276.68	318.79
T	*Globanomalina pseudomenardii*	55.90	55.90	1265A-31H-CC	278.21	320.49	1265A-32H-CC	285.56	328.05
B	*Morozovella aequa*	56.50	56.50	1265A-32H-CC	285.56	328.05	1265A-34X-CC	296.21	340.74
B	*Acarinina soldadoensis*	56.50	56.50	1265A-32H-CC	285.56	328.05	1265A-34X-CC	296.21	340.74

Notes: T = top, B = bottom. * = benthic foraminiferal datum level.

Table T8. Stratigraphic ranges and relative abundances for selected planktonic foraminifer taxa, Site 1265. (This table is available in an **oversized format.**)

Table T9. Occurrence of selected benthic foraminifer taxa, Site 1265. (This table is available in an **oversized format.**)

Table T10. Magnetostratigraphic age-depth tie points, Site 1265.

			Top			Bottom		
	Age (Ma)		Hole, core, section,	Depth		Hole, core, section,	Depth	
Chron	1	2	interval (cm)	(mbsf)	(mcd)	interval (cm)	(mbsf)	(mcd)
			208-			208-		
C1n (o)	0.781	0.780	1265B-1H-3, 85	3.68	3.68	1265B-1H-4, 20	4.03	4.03
C2n (y)	1.785	1.770	1265A-1H-5, 30	6.30	7.92	1265A-1H-6, 25	7.75	9.37
C2n (o)	1.942	1.950	1265A-1H-7, 15	9.15	10.77	1265A-2H-1, 60	10.10	12.83
C3n (o)	5.236	5.230	1265A-3H-7, 10	28.10	31.40	1265A-4H-1, 90	29.40	34.30
C5En (o)	18.524	18.781	1265A-9H-2, 90	78.40	89.52	1265A-9H-2, 135	78.85	89.97
C6n (y)	18.748	19.048	1265A-9H-2, 140	78.90	90.02	1265A-9H-3, 65	79.65	90.77
C6n (o)	19.722	20.131	1265A-9H-7, 40	84.90	96.02	1265A-10H-1, 60	86.10	98.17
C6An (y)	20.040	20.518	1265A-10H-2, 90	87.90	99.97	1265A-10H-3, 30	88.80	100.87
C6An (o)	20.709	21.320	1265A-10H-6, 25	93.25	105.32	1265A-10H-6, 80	93.80	105.87
C6Bn (y)	21.767	22.588	1265A-11H-3, 45	98.45	112.22	1265A-11H-3, 145	99.45	113.22
C6Bn (o)	22.268	23.069	1265A-11H-7, 45	104.45	118.22	1265B-12H-4, 35	104.52	118.97
C6Cn.1n (y)	22.564	23.353	1265A-12H-2, 45	106.45	121.41	1265A-12H-2, 60	106.60	121.56
C6Cn.1n (o)	22.754	23.535	1265A-12H-2, 115	107.15	122.11	1265A-12H-3, 5	107.55	122.51
C6Cn.2n (y)	22.902	23.677	1265A-12H-3, 140	108.90	123.86	1265A-12H-4, 40	109.40	124.36
C6Cn.2n (o)	23.030	23.800	1265A-12H-4, 70	109.70	124.66	1265A-12H-4, 100	110.00	124.96
C6Cn.3n (y)	23.230	23.999	1265A-12H-5, 55	111.05	126.01	1265A-12H-5, 75	111.25	126.21
C6Cn.3n (o)	23.340	24.118	1265A-12H-5, 125	111.75	126.71	1265A-12H-5, 145	111.95	126.91
C7n (y)	24.011	24.730	1265A-13H-3, 5	117.05	132.95	1265A-13H-4, 105	119.55	135.45
C8n (y)	25.053	25.823	1265A-14H-1, 70	124.20	142.00	1265A-14H-1, 145	124.95	142.75
C8n (o)	26.061	26.554	1265A-14H-6, 60	131.60	149.40	1265A-14H-6, 115	132.15	149.95
C13n (y)		33.058	1265A-18H-3, 20	164.70	186.70	1265A-18H-3, 55	165.05	187.05
C13n (o)		33.545	1265B-18H-7, 25	165.95	188.48	1265A-18H-7, 5	169.03	191.03
C25n (y)		55.904	1265A-32H-4, 140	284.10	326.59	1265A-32H-5, 10	284.30	326.79

Notes: o = old end of chron, y = young end of chron. 1 = ages as in Lourens et al. (in press) and H. Pälike (pers. comm., 2003), 2 = ages as in Cande and Kent (1995).

Table T11. Composition of headspace gases, Hole 1265A.

Core, section, interval (cm)	Depth (mcd)	C_1 (ppm)
208-1265A-		
1H-6, 0–5	9.1	1.8
2H-6, 0–5	19.7	1.8
3H-6, 0–5	29.8	1.9
4H-6, 0–5	40.8	1.7
5H-6, 0–5	52.2	1.8
6H-6, 0–5	62.9	1.9
7H-6, 0–5	72.7	1.9
8H-6, 0–5	83.6	1.7
9H-6, 0–5	94.6	1.9
10H-6, 0–5	105.1	1.9
11H-6, 0–5	116.3	1.7
12H-6, 0–5	127.0	1.7
13H-6, 0–5	137.4	1.7
14H-6, 0–5	148.8	1.9
15H-6, 0–5	160.3	2.0
16H-5, 0–5	168.9	1.7
17H-6, 0–5	180.7	1.9
18H-5, 0–5	189.5	1.8
19H-6, 0–5	201.8	1.8
20H-4, 0–5	209.5	1.8
21H-6, 0–5	223.2	1.8
22H-6, 0–5	235.6	1.9
23H-5, 0–5	245.5	1.9
24H-6, 0–5	259.0	1.8
25H-6, 0–5	270.0	2.0
26H-6, 0–5	281.4	1.9
27H-6, 0–5	292.5	2.1
28H-6, 0–5	303.5	2.2
29H-6, 0–5	313.7	2.2
32H-5, 0–5	326.7	2.3

Table T12. Interstitial water analyses, Site 1265.

Hole, core, section, interval (cm)	Depth (mcd)	pH	Alkalinity (mM)	Salinity	Cl (mM)	SO_4 (mM)	Na (mM)	Mg (mM)	Ca (mM)	K (mM)	B (µM)	Fe (µM)	Mn (µM)	Li (µM)	Ba (µM)	Sr (µM)	Si (µM)	Zn (µM)
208-																		
1265A-1H-5, 145–150	9.1	7.42	2.17	35.0	556	26.8	469	50.0	11.0	10.7	457	0.00	0.22	ND	0.34	136	369	0.54
1265A-2H-5, 140–150	19.6	7.40	ND	35.0	567	26.2	478	52.6	11.5	10.4	462	0.00	0.38	ND	0.21	176	313	0.04
1265A-3H-5, 140–150	29.7	7.34	3.48	35.0	571	25.5	ND	50.3	13.9	ND	465	0.10	2.11	28.3	2.48	155	248	1.09
1265A-4H-5, 140–150	40.7	7.30	2.66	35.0	568	25.9	476	51.9	12.5	10.1	461	0.41	2.25	ND	0.19	211	243	0.18
1265A-5H-5, 140–150	52.1	7.37	2.68	35.0	567	25.1	462	49.6	12.5	9.59	452	0.00	2.49	ND	0.22	226	255	0.44
1265A-6H-5, 140–150	62.8	7.29	2.72	35.0	567	25.4	474	50.1	13.2	9.90	487	0.00	2.88	ND	0.23	198	253	0.39
1265A-7H-5, 140–150	72.6	7.18	2.60	35.5	568	25.1	469	50.3	13.8	9.86	501	0.94	3.38	ND	1.85	233	244	1.20
1265A-8H-5, 140–150	83.5	7.31	2.61	35.5	569	25.3	477	49.2	14.0	9.75	499	0.00	2.52	ND	0.33	251	248	0.36
1265A-9H-5, 140–150	94.5	7.25	2.60	35.5	564	25.4	477	49.2	13.7	9.54	481	0.03	1.67	ND	0.25	255	275	0.29
1265A-10H-5, 140–150	105.0	7.29	2.61	35.5	566	24.7	475	49.1	14.7	9.27	469	0.03	1.15	32.4	0.22	252	237	0.16
1265A-11H-5, 140–150	116.2	7.21	2.60	35.5	560	24.7	476	47.4	15.8	9.68	501	0.66	1.53	35.9	0.24	258	337	0.00
1265A-14H-5, 140–150	148.7	7.39	2.59	35.0	565	24.5	476	47.5	16.1	8.97	493	0.00	1.61	34.0	0.26	289	336	0.29
1265A-15H-5, 140–150	160.2	7.27	2.60	35.5	567	24.4	462	45.7	16.7	8.65	457	0.10	2.82	ND	0.46	277	334	0.99
1265B-16H-5, 140–150	165.2	7.34	3.48	35.0	572	24.2	470	47.5	16.3	8.51	470	0.00	1.82	35.9	0.26	289	323	0.15
1265A-16H-4, 140–150	168.8	7.31	2.60	35.5	568	24.2	479	48.4	17.2	8.61	484	0.00	2.02	ND	0.27	289	389	0.28
1265B-17H-5, 140–150	175.7	7.38	2.57	35.0	572	24.5	476	46.0	17.3	8.50	488	0.00	2.57	ND	2.58	297	365	0.10
1265B-18H-4, 140–150	185.1	7.27	2.59	35.0	568	23.8	475	45.5	17.1	8.23	470	0.07	2.81	ND	0.28	299	398	0.48
1265B-19H-5, 140–150	196.1	7.29	2.59	35.0	567	24.2	479	46.7	18.0	8.34	485	0.21	4.66	ND	0.32	307	425	0.47
1265B-20H-4, 140–150	206.2	7.34	2.55	34.0	565	26.6	478	45.4	18.2	8.42	455	0.58	4.13	37.7	2.97	299	481	0.16
1265A-21H-5, 140–150	223.1	7.31	2.57	34.5	569	24.0	477	44.7	18.2	8.16	457	0.00	4.23	ND	2.00	315	597	0.43
1265A-22H-5, 140–150	235.5	7.30	2.54	35.5	570	23.7	475	43.9	18.2	7.88	446	0.00	4.28	38.3	0.28	313	645	0.49
1265A-23H-4, 140–150	245.4	7.30	2.55	34.5	570	23.3	478	44.6	19.1	8.11	459	0.00	3.95	ND	0.30	317	760	0.60
1265B-25H-5, 140–150	263.9	7.32	2.54	35.0	571	25.9	479	42.1	19.1	8.01	443	0.00	3.60	36.8	0.34	305	762	0.11
1265B-26H-4, 140–150	273.3	7.19	2.72	34.5	571	23.6	471	44.7	19.8	8.08	442	0.00	3.86	38.6	0.66	287	882	0.35
1265A-32H-4, 140–150	326.6	7.34	2.22	35.0	571	23.2	475	43.6	21.4	7.67	424	0.06	1.58	40.7	2.80	319	1428	0.21
1265A-35X-3, 140–150	351.9	7.20	2.25	35.0	574	22.8	475	42.3	21.5	7.03	416	0.63	1.35	40.0	0.41	306	1181	0.53

Note: ND = not determined.

Table T13. Sedimentary inorganic carbon and calcium carbonate concentrations, Site 1265.

Core, section, interval (cm)	Depth (mcd)	Inorganic carbon (wt%)	$CaCO_3$ (wt%)
208-1265A-			
1H-1, 72–73	2.34	11.6	97.0
1H-3, 72–73	5.34	11.5	96.0
1H-5, 72–73	8.34	11.5	96.0
1H-5, 145–150	9.07	11.6	96.4
2H-1, 72–73	12.95	11.6	96.6
2H-3, 72–73	15.95	11.5	95.9
2H-5, 72–73	18.95	11.6	96.2
2H-5, 140–150	19.63	11.7	97.0
3H-1, 72–73	23.02	11.6	96.7
3H-3, 72–73	26.02	11.7	97.7
3H-5, 72–73	29.02	11.8	98.4
3H-5, 140–150	29.70	11.6	96.7
4H-1, 72–73	34.12	11.8	98.4
4H-3, 72–73	36.97	11.7	97.8
4H-5, 72–73	39.97	11.3	94.5
4H-5, 140–150	40.65	11.2	93.5
5H-1, 72–73	45.42	11.4	94.7
5H-3, 72–73	48.42	11.7	97.2
5H-5, 72–73	51.42	11.5	95.4
5H-5, 140–150	52.10	11.6	96.2
6H-1, 72–73	56.07	11.3	93.9
6H-3, 72–73	59.07	11.3	93.8
6H-5, 72–73	62.07	11.5	95.6
6H-5, 140–150	62.75	11.3	94.5
7H-1, 72–73	65.90	11.7	97.4
7H-3, 72–73	68.90	11.3	93.8
7H-5, 72–73	71.90	11.2	93.5
7H-5, 140–150	72.58	11.0	91.3
8H-1, 72–73	76.84	11.3	93.7
8H-3, 72–73	79.84	11.1	92.2
8H-5, 72–73	82.84	11.6	96.3
8H-5, 140–150	83.52	10.6	89.7
9H-1, 72–73	87.84	11.1	92.6
9H-3, 72–73	90.84	13.8	92.7
9H-5, 72–73	93.84	11.4	95.2
9H-5, 140–150	94.52	11.4	95.1
10H-1, 72–73	98.29	10.9	94.8
10H-3, 72–73	101.29	11.5	95.6
10H-5, 72–73	104.29	11.5	95.4
10H-5, 140–150	104.97	11.6	96.9
11H-1, 72–73	109.49	11.3	94.1
11H-3, 72–73	112.49	11.2	93.5
11H-5, 72–73	115.49	11.5	95.4
11H-5, 140–150	116.17	11.3	93.8
12H-1, 72–73	120.18	11.4	94.9
12H-3, 72–73	123.18	11.5	95.7
12H-5, 72–73	126.18	11.2	93.4
13H-1, 72–73	130.62	11.0	91.8
13H-3, 72–73	133.62	11.1	92.1
13H-5, 72–73	136.62	11.4	94.6
14H-1, 72–73	142.02	11.1	92.1
14H-3, 72–73	145.02	11.5	95.7
14H-5, 72–73	148.02	11.8	92.5
14H-5, 140–150	148.70	11.2	93.1
15H-1, 72–73	153.47	11.0	91.6
15H-3, 72–73	156.47	11.0	91.6
15H-5, 72–73	159.47	11.3	94.1
15H-5, 140–150	160.15	11.4	95.0
16H-1, 72–73	163.65	11.3	94.2
16H-3, 72–73	166.65	11.5	95.5
16H-4, 140–150	168.83	11.4	95.1
16H-5, 72–73	169.65	11.3	93.9
17H-1, 72–73	173.95	11.0	91.9
17H-3, 72–73	176.95	11.2	93.3
17H-5, 72–73	179.95	11.1	92.8
18H-1, 72–73	184.22	11.3	94.4
18H-3, 72–73	187.22	10.7	94.6
18H-5, 67–68	190.17	11.1	92.3
19H-1, 72–73	195.03	11.2	93.1
19H-3, 72–73	198.03	10.9	91.0
19H-5, 72–73	201.03	11.2	93.1
20H-1, 72–73	205.74	11.0	91.4
20H-3, 72–73	208.74	11.1	92.1
20H-5, 72–73	211.74	11.1	92.3
21H-1, 72–73	216.37	11.3	94.4
21H-3, 72–73	219.37	11.4	94.9
21H-5, 72–73	222.37	11.6	96.3
21H-5, 140–150	223.05	11.1	92.7
22H-1, 72–73	228.80	11.5	95.5
22H-3, 72–73	231.80	11.6	96.5
22H-5, 72–73	234.80	11.6	96.7
22H-5, 140–150	235.48	11.5	96.1
23H-1, 72–73	240.20	11.7	97.5
23H-3, 72–73	243.20	11.6	96.4
23H-4, 140–150	245.38	11.3	93.7
23H-5, 72–73	246.20	11.5	96.1
24H-1, 72–73	252.18	11.6	96.8
24H-3, 72–73	255.18	11.7	97.2
24H-5, 72–73	258.18	11.7	97.4
25H-1, 72–73	262.91	11.4	95.1
25H-3, 72–73	265.91	11.4	94.8
25H-5, 72–73	268.91	11.4	95.1
26H-1, 72–73	274.57	11.4	95.0
26H-3, 72–73	277.57	10.8	90.0
26H-5, 72–73	280.57	11.3	94.4
27H-1, 72–73	285.75	11.3	93.9
27H-3, 72–73	288.75	11.2	93.6
27H-5, 72–73	291.75	11.2	93.2
28H-1, 72–73	296.67	11.1	92.6
28H-3, 72–73	299.67	11.4	95.0
28H-5, 72–73	302.67	10.8	90.5
29H-1, 72–73	307.50	11.2	93.6
29H-3, 68–69	309.84	11.0	91.9
29H-6, 70–70	314.36	10.8	90.1
29H-6, 75–75	314.41	11.1	92.4
29H-6, 80–80	314.46	10.5	87.6
29H-6, 85–85	314.51	10.3	85.7
29H-6, 90–90	314.56	10.5	87.7
29H-6, 95–95	314.61	10.8	89.9
29H-6, 100–100	314.66	11.1	92.4
29H-6, 105–105	314.71	11.0	91.3
29H-6, 110–110	314.76	10.8	90.0
29H-6, 115–115	314.81	11.3	94.0
29H-6, 120–120	314.86	10.5	87.1
29H-6, 125–125	314.91	10.6	88.6
29H-6, 130–130	314.96	10.6	88.1
29H-6, 135–135	315.01	10.7	88.8
29H-6, 140–140	315.06	10.6	88.6
29H-6, 145–145	315.11	10.7	88.8
29H-6, 150–150	315.16	10.6	88.4
29H-7, 5–5	315.21	10.8	90.0
29H-7, 10–10	315.26	10.7	89.4
29H-7, 15–15	315.31	10.8	90.3
29H-7, 20–20	315.36	10.5	87.5
29H-7, 25–25	315.41	10.1	84.1
29H-7, 30–30	315.46	9.7	81.0
29H-7, 32–32	315.48	9.7	81.1
29H-7, 34–34	315.50	8.9	74.5
29H-7, 36–36	315.52	8.4	70.3
29H-7, 38–38	315.54	8.6	71.3
29H-7, 40–40	315.56	8.9	74.4
29H-7, 42–42	315.58	8.7	72.2
29H-7, 44–44	315.60	9.2	76.6
29H-7, 46–46	315.62	7.2	59.7
29H-7, 48–48	315.64	7.7	64.5
29H-7, 50–50	315.66	7.5	62.1
29H-7, 52–52	315.68	7.0	58.3
29H-7, 54–54	315.70	6.7	56.0
29H-7, 56–56	315.72	6.4	53.3
29H-7, 58–58	315.74	5.8	48.1
29H-7, 60–60	315.76	5.8	48.7
29H-7, 62–62	315.78	5.6	47.0
29H-7, 64–64	315.80	5.0	42.0
29H-7, 66–66	315.82	3.6	30.0
29H-7, 68–68	315.84	4.2	34.6
29H-7, 70–70	315.86	9.2	76.7
29H-7, 75–75	315.91	10.5	87.2
29H-7, 80–80	315.96	10.7	89.1
29H-7, 85–85	316.01	10.8	90.1
29H-7, 90–90	316.06	11.7	91.9
29H-7, 95–95	316.11	10.8	89.6
29H-7, 100–100	316.16	10.7	89.2
29H-7, 105–105	316.21	10.8	89.6
29H-7, 110–110	316.26	10.4	86.9
29H-7, 115–115	316.31	10.1	84.2
29H-7, 120–120	316.36	9.7	80.7
29H-7, 125–125	316.41	10.4	86.7
29H-7, 130–130	316.46	10.8	90.1
29H-7, 135–135	316.51	11.1	92.4
29H-7, 140–140	316.56	11.0	91.5
29H-7, 145–145	316.61	10.8	90.3
29H-7, 150–150	316.66	11.0	91.9
30H-1, 72–73	318.33	11.0	91.5
31H-1, 72–73	319.70	11.1	92.5
32H-1, 72–73	321.41	11.3	94.1
32H-3, 82–83	324.51	11.0	91.7
32H-4, 140–150	326.59	12.1	95.4
32H-5, 72–73	327.41	11.3	94.3
34X-1, 93–94	337.46	10.6	90.6
34X-3, 56–57	340.09	10.9	90.6
35X-1, 82–83	348.30	10.8	90.1
35X-3, 72–73	351.20	11.2	93.4
35X-3, 140–150	351.88	11.2	93.2
35X-5, 72–73	354.20	10.8	89.6
36X-1, 60–61	359.02	10.9	90.6
208-1265B-			
16H-5, 140–150	165.21	11.2	93.0
17H-5, 140–150	175.72	11.1	92.7
18H-4, 140–150	185.13	11.1	92.5
19H-5, 140–150	196.08	11.0	91.3
20H-4, 140–150	206.19	11.2	93.1
25H-5, 140–150	263.89	11.4	94.8
26H-4, 140–150	273.29	11.3	94.2

Table T14. Breakdown of logging operations, Hole 1265A.

Date (Apr 2003)	Local time (hr)	Operations
10	1200	Hole preparation complete, rig up triple combo (MGT-HNGS-APS-HLDS-DIT-TAP)
	1700	Run into hole with triple combo
	1800	Uplog with triple combo (HNGS-APS-HLDS-DIT) at 900 ft/hr from total depth
	1915	Going down for a second pass
	1935	Repeat with triple combo (HNGS-HLDS-DIT, no APS)
	1955	Going down for an MGT pass
	2010	Uplog with MGT at 600 ft/hr from total depth
	2230	Pull tools out of hole and rigdown
11	0000	Rig up FMS-sonic (SGT-DSI-GPIT-FMS)
	0030	Run into hole with FMS-sonic
	0200	Short pass with FMS-sonic at 900 ft/hr from total depth
	0215	Going down for a main pass
	0220	Uplog with FMS-sonic at 900 ft/hr from total depth
	0315	Pull tools out of hole and rig down
	0500	Rig up WST-3
	0530	Run into hole with WST-3
	0700	Checkshots (7)
	0820	Pull tool out of hole and rig down
	0930	Clear rig floor of logging tools, sheaves, and wireline
	1100	End of logging operation

Notes: Drillers total depth = 3392.0 mbrf, water depth = 3060 m, end of pipe = 69.0 mbsf, total depth = 321 mbsf. MGT = Multi-Sensor Gamma Ray Tool, HNGS = Hostile Environment Natural Gamma Ray Sonde, APS = Accelerator Porosity Sonde, HLDS = Hostile Environment Litho-Density Sonde, DIT = Dual Induction Tool, TAP = Temperature/Acceleration/Pressure tool, FMS = Formation MicroScanner, SGT = Scintillation Gamma Ray Tool, DSI = Dipole Sonic Imager tool, GPIT = General Purpose Inclinometry Tool, WST-3 = three-component Well Seismic Tool.

Table T15. Meters composite depth and equivalent logging depth, Site 1265.

Depth (mcd)	Equivalent logging depth (mbsf)
77.97	71.45
82.87	76.17
90.07	81.20
95.67	86.40
99.72	88.97
110.07	93.54
117.71	99.18
122.05	103.30
130.48	110.31
134.47	113.05
139.54	116.71
154.42	128.29
159.07	137.28
163.90	142.46
168.65	149.93
173.29	154.20
188.44	168.52
195.10	175.23
200.80	180.26
210.31	186.97
218.88	192.76
221.51	197.18
223.26	200.22
235.39	210.28
241.22	220.49
255.29	227.05
262.89	230.70
269.18	233.90
277.52	242.74
281.90	247.16
299.32	260.88
305.61	268.20
310.01	269.72
311.95	271.24
315.72	274.29
316.71	275.29
318.17	277.03
322.05	282.22
323.68	283.28
325.73	286.63
337.30	292.73

Table T16. Checkshot survey, Site 1265.

Stack number	Measured depth (m)	Depth (mbsf)	One-way TT (ms)		Interval velocity (m/s)
			Measured	Corrected	
6	3,250	175	2,145.49	2,146.49	1,984.55
5	3,315	240	2,178.23	2,179.24	2,210.64
4	3,340	265	2,189.54	2,190.55	2,197.94
3	3,360	285	2,198.63	2,199.65	2,308.14
2	3,380	305	2,207.30	2,208.31	2,142.52
1	3,395	320	2,214.30	22,153.32	

Note: TT = traveltime.

Table T17. Age-depth control points, Site 1265. (See table notes. Continued on next page.)

	Datum	Type	Upper depth (mcd)	Lower depth (mcd)	Minimum age (Ma)	Maximum age (Ma)
T	*Globorotalia tosaensis*	PF	0.00	4.72	0.61	0.61
T	*Pseudoemiliania lacunosa*	CN	1.82	2.82	0.46	0.46
	C1n (o)	PMAG	3.67	4.02	0.781	0.781
T	Large *Gephyrocapsa* spp.	CN	4.32	5.82	1.22	1.22
T	*Globigerina apertura*	PF	4.72	11.08	1.68	1.68
T	*Globigerinoides extremus*	PF	4.72	11.08	1.91	1.91
B	Large *Gephyrocapsa* spp.	CN	5.82	7.32	1.58	1.58
T	*Calcidiscus macintyrei*	CN	7.32	8.82	1.67	1.67
B	Medium *Gephyrocapsa* spp.	CN	7.32	8.82	1.69	1.69
	C2n (y)	PMAG	7.92	9.37	1.785	1.785
T	*Discoaster brouweri* and *D. triradiatus*	CN	8.82	10.32	1.95	1.95
	C2n (o)	PMAG	10.77	12.83	1.942	1.942
T	*Discoaster pentaradiatus*	CN	11.08	21.26	2.52	2.52
T	*Reticulofenestra pseudoumbilicus*	CN	11.08	21.26	3.82	3.82
B	*Globorotalia truncatulinoides*	PF	11.08	16.08	2.03	2.03
T	*Dentoglobigerina altispira*	PF	16.08	21.26	3.02	3.02
T	*Amaurolithus* spp.	CN	21.26	31.88	4.56	4.56
T	*Globorotalia plesiotumida*	PF	26.81	31.88	4.15	4.15
T	*Hirsutella cibaoensis*	PF	26.81	31.88	4.16	4.16
B	*Globorotalia crassaformis* s.l.	PF	26.81	31.88	4.31	4.31
T	*Globoturborotalita nepenthes*	PF	26.81	31.88	4.37	4.37
	C3n (o)	PMAG	31.40	34.30	5.236	5.236
T	*Nicklithus amplificus*	CN	31.88	33.55	6.00	6.00
B	*Sphaeroidinella dehiscens* (s.l.)	PF	31.88	37.25	4.94	4.94
B	*Globorotalia plesiotumida*	PF	31.88	42.51	8.91	8.91
B	*Nicklithus amplificus*	CN	36.27	36.75	6.84	6.84
B	*Amaurolithus primus*	CN	36.75	37.25	7.39	7.39
B	*Globigerinoides conglobatus*	PF	37.25	31.88	5.84	5.84
B	*Globigerinoides extremus*	PF	37.25	42.51	8.94	8.94
T	*Menardella praemenardii*	PF	42.51	49.55	10.09	10.09
B	*Discoaster bellus* gr. (*D. hamatus*)	CN	45.80	46.60	10.48	10.48
T	*Paragloborotalia mayeri*	PF	49.55	54.32	10.70	10.70
B	*Catinaster coalitus*	CN	51.10	54.20	10.79	10.79
	C5n (o)	PMAG	53.90	55.95	11.043	11.043
B	*Globoturborotalita nepenthes*	PF	54.32	59.94	11.64	11.64
T	*Hirsutella praescitula*	PF	59.94	64.74	13.73	13.73
T	*Menardella archeomenardii*	PF	59.94	64.74	13.92	13.92
T	*Fohsella peripheroronda*	PF	59.94	64.74	13.92	13.92
B	*Triquetrorhabdulus rugosus*	CN	60.95	61.50	12.81	12.81
T	*Sphenolithus heteromorphus*	CN	64.74	75.01	13.55	13.55
B	*Menardella praemenardii*	PF	64.74	75.01	13.95	13.95
B	*Fohsella peripheroacuta*	PF	64.74	75.01	14.02	14.02
T	*Praeorbulina sicana*	PF	70.41	75.01	14.63	14.63
B	*Orbulina suturalis*	PF	70.41	75.01	14.70	14.70
B	*Orbulina* spp.	PF	70.41	75.01	14.71	14.71
B	*Menardella archeomenardii*	PF	75.01	80.33	16.16	16.16
B	*Sphenolithus heteromorphus*	CN	85.74	87.52	17.76	17.76
T	*Sphenolithus belemnos*	CN	85.74	87.52	17.89	17.89
B	*Praeorbulina sicanus*	PF	85.74	90.73	16.86	16.86
T	*Catapsydrax dissimilis*	PF	85.74	90.73	17.51	17.51
T	*Globoquadrina binaiensis*	PF	85.74	96.41	19.08	19.08
	C5En (o)	PMAG	89.52	89.97	18.524	18.524
	C6n (y)	PMAG	90.02	90.77	18.748	18.748
B	*Sphenolithus belemnos*	CN	92.82	93.52	18.92	18.92
	C6n (o)	PMAG	96.02	98.17	19.722	19.722
B	*Globoquadrina binaiensis*	PF	96.41	107.27	19.98	19.98
	C6An (y)	PMAG	99.97	100.87	20.040	20.040
	C6An (o)	PMAG	105.32	105.87	20.709	20.709
T	*Paragloborotalia kugleri*	PF	107.27	118.63	21.03	21.03
	C6Bn (y)	PMAG	112.22	113.22	21.767	21.767
	C6Bn (o)	PMAG	118.22	118.97	22.268	22.268
B	*Globoquadrina dehiscens*	PF	118.63	129.06	21.44	21.44
B	*Globigerinoides trilobus* s.l.	PF	118.63	124.08	22.87	22.87
	C6Cn.1n (y)	PMAG	121.41	121.56	22.564	22.564
	C6Cn.1n (o)	PMAG	122.11	122.51	22.754	22.754
	C6Cn.2n (y)	PMAG	123.86	124.36	22.902	22.902
T	*Globigerina euapertura*	PF	124.08	129.06	23.03	23.03
	C6Cn.2n (o)	PMAG	124.66	124.96	23.030	23.030

Table T17 (continued).

	Datum	Type	Upper depth (mcd)	Lower depth (mcd)	Minimum age (Ma)	Maximum age (Ma)
	C6Cn.3n (y)	PMAG	126.01	126.21	23.230	23.230
	C6Cn.3n (o)	PMAG	126.71	126.91	23.340	23.340
T	*Sphenolithus delphix*	CN	128.86	129.06	23.07	23.07
B	*Paragloborotalia kugleri*	PF	129.06	133.36	22.87	22.87
B	*Sphenolithus delphix*	CN	130.60	130.90	23.33	23.33
	C7n (y)	PMAG	132.95	135.45	24.011	24.011
T	*Sphenolithus ciperoensis*	CN	134.20	139.80	24.23	24.23
T	*Sphenolithus distentus*	CN	139.80	150.38	25.98	25.98
B	*Globigerinoides primordius* (common)	PF	139.80	145.78	23.54	23.54
B	*Paragloborotalia pseudokugleri*	PF	139.80	145.78	25.15	25.15
	C8n (y)	PMAG	142.00	142.75	25.053	25.053
	C8n (o)	PMAG	149.40	149.95	26.061	26.061
T	*Chiloguembelina cubensis* (common)	PF	156.59	162.34	27.92	27.92
B	*Sphenolithus ciperoensis*	CN	159.45	160.12	27.55	27.55
B	*Sphenolithus distentus*	CN	167.73	168.43	30.32	30.32
T	*Pseudohastigerina spp.*	PF	177.32	182.69	32.00	32.00
T	*Reticulofenestra umbilicus* >14 µm	CN	178.03	178.83	31.7	31.7
T	*Isthmolithus recurvus*	CN	178.03	178.83	32.7	32.7
T	*Ericsonia formosa*	CN	184.60	185.30	32.9	32.9
	C13n (y)	PMAG	186.70	187.05	33.058	33.058
	C13n (o)	PMAG	188.48	191.13	33.545	33.545
T	*Hantkenina* spp.	PF	188.80	192.02	33.70	33.70
T	*Discoaster saipanensis*	CN	192.02	194.61	34.0	34.0
T	*Globigerinatheka index*	PF	192.02	198.13	34.30	34.30
T	*Globigerinatheka semiinvoluta*	PF	192.02	198.13	35.30	35.30
T	*Calcidiscus protoannulus*	CN	197.61	198.76	35.4	35.4
T	*Turborotalia cerroazulensis*	PF	198.13	204.08	33.80	33.80
B	*Isthmolithus recurvus*	CN	200.70	201.76	36.6	36.6
B	*Chiasmolithus oamaruensis*	CN	208.22	208.62	37.0	37.0
T	*Chiasmolithus grandis*	CN	208.62	209.42	37.1	37.1
B	*Dictyococcites bisectus*	CN	210.92	211.22	38.5	38.5
B	*Dictyococcites scrippsae*	CN	211.95	216.05	40.3	40.3
T	*Nannotetrina* spp.	CN	211.95	216.05	42.3	42.3
B	*Reticulofenestra umbilicus* >14 µm	CN	216.05	224.95	42.5	42.5
T	*Morozovella aragonensis*	PF	219.82	225.43	43.60	43.60
B	*Nannotetrina* spp.	CN	225.43	228.48	47.8	47.8
B	*Discoaster sublodoensis*	CN	225.43	228.48	49.3	49.3
T	*Discoaster lodoensis*	CN	230.68	231.48	48.0	48.0
T	*Morozovella formosa*	PF	237.92	243.21	50.80	50.80
T	*Tribrachiatus orthostylus*	CN	241.38	242.08	51.0	51.0
B	*Morozovella aragonensis*	PF	257.30	257.40	52.30	52.30
B	*Discoaster lodoensis*	CN	257.86	258.56	52.4	52.4
T	*Discoaster multiradiatus*	CN	268.64	269.59	53.0	53.0
B	*Sphenolithus radians*	CN	275.95	276.35	53.3	53.3
B	*Tribrachiatus orthostylus*	CN	280.75	282.25	53.4	53.4
B	*Discoaster diastypus*	CN	291.28	295.00	53.9	53.9
B	*Igorina broedermanni*	PF	315.14	315.24	54.70	54.70
T	*Stensioeina beccariiformis*	BF	315.81	315.86	55.0	55.0
B	*Morozovella subbotinae*	PF	316.91	318.79	55.90	55.90
T	*Globanomalina pseudomenardii*	PF	320.49	328.05	55.90	55.90
	C25n (y)	PMAG	325.83	326.03	55.904	55.904
B	*Morozovella aequa*	PF	328.05	340.74	56.50	56.50
B	*Acarinina soldadoensis*	PF	328.05	340.74	56.50	56.50
B	*Discoaster multiradiatus*	CN	340.23	340.64	56.2	56.2

Notes: T = top, B = bottom. o = oldest, y = youngest. PF = planktonic foraminifers, CN = calcareous nannoplankton, PMAG = paleomagnetic reversals. This table is also available in **ASCII.**

Table T18. Age model, linear sedimentation rates, and mass accumulation rates, Site 1265.

Age (Ma)	Depth (mcd)	LSR	Growth Factor	Corrected LSR	Dry density (g/cm^3)	CaCO$_3$ (wt%)	Total MAR (g/cm^2/k.y.)	CaCO$_3$ MAR (g/cm^2/k.y.)	Noncarbonate MAR (g/cm^2/k.y.)
1	4.72	4.72	1.15	4.10	1.06	97.0	0.44	0.422	0.013
2	9.89	5.17	1.15	4.49	1.18	96.1	0.53	0.509	0.021
3	15.79	5.90	1.15	5.13	1.19	96.6	0.61	0.589	0.021
4	21.76	5.97	1.15	5.20	1.23	96.4	0.64	0.614	0.023
5	29.56	7.80	1.15	6.78	1.25	97.6	0.85	0.828	0.020
6	33.20	3.64	1.15	3.16	0.00	96.7	0.00	0.000	0.000
7	36.66	3.46	1.15	3.01	1.42	98.4	0.43	0.420	0.007
8	37.85	1.19	1.15	1.03	1.36	97.8	0.14	0.137	0.003
9	40.04	2.19	1.15	1.90	1.11	94.5	0.21	0.200	0.012
10	43.72	3.68	1.15	3.20	0.00	93.5	0.00	0.000	0.000
11	54.19	10.47	1.15	9.10	1.18	95.9	1.08	1.034	0.044
12	58.45	4.25	1.15	3.70	1.22	93.9	0.45	0.423	0.028
13	62.23	3.79	1.15	3.29	1.20	94.7	0.40	0.374	0.021
14	67.54	5.31	1.15	4.62	1.19	95.9	0.55	0.528	0.022
15	72.15	4.60	1.15	4.00	1.15	93.6	0.46	0.429	0.029
16	76.88	4.73	1.15	4.11	1.16	92.5	0.48	0.442	0.036
17	81.90	5.02	1.15	4.36	1.17	92.2	0.51	0.471	0.040
18	87.30	5.41	1.15	4.70	1.09	92.4	0.51	0.475	0.039
19	93.68	6.38	1.15	5.55	1.19		0.66		
20	100.14	6.46	1.15	5.62	1.21	93.7	0.68	0.635	0.043
21	108.02	7.88	1.15	6.85	1.23	95.9	0.84	0.809	0.034
22	117.28	9.25	1.15	8.05	1.21	94.2	0.97	0.918	0.057
23	128.30	11.02	1.15	9.58	1.22	94.7	1.17	1.105	0.062
24	135.41	7.11	1.15	6.18	1.22	91.9	0.76	0.696	0.061
25	142.33	6.93	1.15	6.02	1.24	93.3	0.75	0.696	0.050
26	149.26	6.92	1.15	6.02	1.26	95.6	0.76	0.727	0.033
27	156.10	6.85	1.15	5.95	1.26	91.6	0.75	0.686	0.063
28	161.12	5.02	1.15	4.36	1.28	93.5	0.56	0.522	0.036
29	164.00	2.88	1.15	2.50	1.21	94.2	0.30	0.285	0.017
30	167.02	3.02	1.15	2.62	1.28	94.3	0.33	0.315	0.019
31	174.26	7.25	1.15	6.30	1.24	93.6	0.78	0.731	0.050
32	180.16	5.90	1.15	5.13	1.18	92.9	0.60	0.560	0.043
33	185.90	5.74	1.15	4.99	1.25	93.5	0.62	0.580	0.041
34	192.30	6.40	1.15	5.57	1.34	90.6	0.75	0.675	0.070
35	196.57	4.27	1.15	3.71	1.28	92.2	0.48	0.439	0.037
36	199.90	3.33	1.15	2.90	1.37	91.0	0.40	0.362	0.036
37	208.42	8.52	1.15	7.41	1.31	92.5	0.97	0.900	0.072
38	210.29	1.87	1.15	1.63	1.26	92.1	0.21	0.189	0.016
39	212.48	2.18	1.15	1.90	1.24	92.3	0.24	0.218	0.018
40	216.24	3.76	1.15	3.27					
41	218.18	1.95	1.15	1.69	1.26	94.4	0.21	0.201	0.012
42	219.56	1.37	1.15	1.19	1.28	94.9	0.15	0.144	0.008
43	220.80	1.25	1.15	1.08					
44	222.00	1.20	1.15	1.04					
45	223.10	1.10	1.15	0.96	1.54	94.5	0.15	0.139	0.008
46	224.10	1.00	1.15	0.87					
47	225.10	1.00	1.15	0.87					
48	226.25	1.15	1.15	1.00	1.33		0.13		
49	227.56	1.31	1.15	1.14					
50	232.61	5.06	1.15	4.40	1.31	96.0	0.58	0.553	0.023
51	241.73	9.12	1.15	7.93	1.37	96.8	1.09	1.051	0.035
52	252.68	10.95	1.15	9.52	1.31	95.8	1.24	1.191	0.053
53	269.12	16.44	1.15	14.29	1.37	95.7	1.96	1.874	0.083
54	295.26	26.14	1.15	22.73	1.35	93.4	3.06	2.862	0.202
55	315.85	20.59	1.15	17.91	1.34	77.2	2.41	1.858	0.548
56	329.43	18.65	1.15	16.21	1.42	89.9	2.53	2.275	0.255

Note: LSR = linear sedimentation rate, MAR = mass accumulation rate. This table is also available in ASCII.